

Search and analysis of giant radio galaxies with associated nuclei (SAGAN). I. New sample and multi-wavelength studies

Dabhade, P.; Mahato, M.; Bagchi, J.; Saikia, D.J.; Combes, F.; Sankhyayan, S.; \dots ; Guiderdoni, B.

Citation

Dabhade, P., Mahato, M., Bagchi, J., Saikia, D. J., Combes, F., Sankhyayan, S., ... Guiderdoni, B. (2020). Search and analysis of giant radio galaxies with associated nuclei (SAGAN). I. New sample and multi-wavelength studies. *Astronomy & Astrophysics*, 642, A153. doi:10.1051/0004-6361/202038344

Version: Accepted Manuscript

License: Leiden University Non-exclusive license

Downloaded from: https://hdl.handle.net/1887/3133656

Note: To cite this publication please use the final published version (if applicable).

Search and Analysis of Giant radio galaxies with Associated Nuclei (SAGAN) - I

New sample & multi-wavelength studies

P. Dabhade^{1,2*}, M. Mahato², J. Bagchi², D. J. Saikia², F. Combes^{3,4}, S. Sankhyayan^{2,5,6}, H. J. A. Röttgering¹, L. C. Ho^{7,8}, M. Gaikwad⁹, S. Raychaudhury^{2,10}, B. Vaidya¹¹, and B. Guiderdoni¹²

May 11, 2020

ABSTRACT

We present the first results of a project called SAGAN, dedicated solely to the studies of relatively rare megaparsec-scale radio galaxies in the Universe, called the Giant Radio Galaxies (GRGs). We have identified 162 new GRGs primarily from the NRAO VLA SKY SURVEY (NVSS) with sizes ranging from ~ 0.71 Mpc to ~ 2.82 Mpc in the redshift range of ~ 0.03 - 0.95, of which 23 are hosted by quasars (Giant Radio Quasars, GRQs). As part of the project SAGAN, we have created a database of all known GRGs - 'GRG-catalogue' from literature (including our new sample) of 820 sources. For the first time, we present the multi-wavelength properties of the largest sample of GRGs, providing new insights about their nature.

Our results firmly establish that the distributions of radio spectral index and the black hole mass of GRGs do not differ from the corresponding distributions of normal sized radio galaxies (RGs). However, GRGs have lower Eddington ratio than RGs. Using the mid-infrared data, we have classified GRGs in terms of their accretion mode: either high-power radiatively-efficient, high-excitation state or a radiatively-inefficient low-excitation state. This enables us to compare key physical properties of their AGN like the black hole mass, spin, Eddington ratio, jet kinetic power, total radio power, magnetic field and size. We find that GRGs in high excitation state statistically have larger sizes, radio power, jet kinetic power and Eddington ratio than those in low excitation state. Our analysis reveals a strong correlation between black hole's accretion efficiency and jet kinetic power, thus suggesting a disk-jet coupling.

Our environmental study reveals that $\sim 10\%$ of all GRGs may reside at the centres of galaxy clusters, in a denser galactic environment while majority seem to reside in sparse environment. The probability of finding the brightest cluster galaxy (BCG) as GRG is quite low and even lower for high mass clusters. Therefore, we present new results on GRGs ranging from black hole mass to large scale environment properties, and discuss their formation and growth scenarios, highlighting the key physical factors responsible for attaining their gigantic size.

Key words. galaxies: jets - galaxies: active - radio continuum: galaxies - quasars: general

1. Introduction

In the 1950s, it was revealed that some galaxies emit dominantly at radio wavelengths (Jennison & Das Gupta 1953; Baade & Minkowski 1954) via the process of synchrotron radiation (Shklovskii 1955; Burbidge 1956). Such galaxies later came to be known as radio galaxies (RGs), whose radio emission often extends well beyond the physical extent of the galaxies as seen at optical wavelengths. Thereafter, it was realised by theoretical efforts (Salpeter 1964; Lynden-

Bell 1969; Bardeen 1970) that a supermassive black hole $(10^6 - 10^{10} \rm \, M_\odot)$ residing at the center of host galaxy must be responsible for powering (Rees 1971) the radio galaxy via twin, collimated and relativistic jets (Blandford & Rees 1974; Scheuer 1974). The creation of the relativistic radio jets is not completely understood and is currently under investigations, but astrophysical models show that these are created by mass accreting, rotating black holes supported by strong magnetic fields (Blandford & Znajek 1977; Blandford & Payne 1982; Meier 1999; Meier et al. 2001). The model given by Blandford & Znajek (1977) (hereafter B-

¹Leiden Observatory, Leiden University, P.O. Box 9513, NL-2300 RA, Leiden, The Netherlands

²Inter-University Centre for Astronomy and Astrophysics (IUCAA), Pune 411007, India

³Sorbonne Université, Observatoire de Paris, Université PSL, CNRS, LERMA, 75014 Paris, France

⁴Collège de France, 11 Place Marcelin Berthelot, 75231 Paris, France

⁵Indian Institute of Science Education and Research (IISER), Dr. Homi Bhabha Road, Pashan, Pune 411008, India

⁶National Centre for Radio Astrophysics, TIFR, Post Bag 3, Ganeshkhind, Pune - 411007, India

⁷Kavli Institute for Astronomy and Astrophysics, Peking University, Beijing 100871, People's Republic of China

⁸Department of Astronomy, School of Physics, Peking University, Beijing 100871, People's Republic of China

⁹ Max-Planck-Institut für Radioastronomie, Auf dem Hugel 69, 53121 Bonn, Germany

 $^{^{10}\}mbox{Department}$ of Physics, Presidency University, 86/1 College Street, Kolkata 700073, India

¹¹ Discipline of Astronomy, Astrophysics and Space Engineering, Indian Institute of Technology Indore, 453552, India

¹² Univ. Lyon, ENS de Lyon, CNRS, Centre de Recherche Astrophysique de Lyon, 69230 Saint-Genis-Laval, France

 $^{^\}star$ E-mail: pratik@strw.leidenuniv.nl

Z) describes the process that is thought to be responsible for powering jets in galactic microquasars and gamma-ray bursts apart from radio galaxies and quasars. Studies over the years have established that supermassive black holes (SMBHs) reside at the centres of almost all massive galaxies (Soltan 1982; Rees 1984; Begelman et al. 1984; Magorrian et al. 1998; Kormendy & Ho 2013) and their active phase is triggered only under certain circumstances. These active forms of SMBHs are known as the active galactic nuclei (AGNs), whose signatures can be observed at almost all wavelengths, ranging from radio to gamma-rays.

AGNs emitting predominantly at radio wavelengths are called radio-loud AGNs (RLAGNs). A smaller fraction and more powerful class of AGNs are the quasars, which are among the most energetic and brightest objects known in the Universe. When the quasar AGNs emit radiation at radio wavelengths, they are labelled as radio-loud quasars (RQs). In high luminosity RGs/RQs, the jets tend to terminate into high brightness regions, called hotspots, at the outer edges of the radio lobes, which are filled with relativistic non-thermal plasma. Such class of RGs are called the Fanaroff-Riley-II (FR-II) class (Fanaroff & Riley 1974). FR-IIs are edge brightened RGs, whereas the Fanaroff-Riley-I (FR-I) class RGs are less powerful compared to FR-II. The FR-I structure is mainly edge-darkened and lobe brightness peaks within the inner half of their extent with the absence of hotspot. The largest angular size has usually been measured between the peaks in the hotspots for FR-II sources and the outermost contours at the 3σ level for FR-I sources. The projected linear size of RGs/RQs extends from less than a few tens of parsecs (pc) to several megaparsecs (Mpc).

In the past six decades, thousands of RGs have been found and catalogued, but only a few hundred of RGs have been discovered so far exhibiting megaparsec scale sizes. Since their discovery in the 1970s by Willis et al. (1974), this relatively rare gigantic sub-class of RGs have been referred to by several names, such as the 'giant radio sources' (GRSs), 'large radio galaxies' (LRGs) and 'giant radio galaxies' (GRGs). In order to avoid confusion and to maintain uniformity, we will refer to this giant sub-class of RGs as 'giant radio galaxies' (GRGs) as previously adopted in several works (Schoenmakers et al. 2001; Dabhade et al. 2017; Ursini et al. 2018; Dabhade et al. 2020).

Since the discovery of GRGs in the 1970s to early 2000s, the Hubble constant (H_0) used to derive the physical properties of the GRGs had a range of values between 50 to 100 km s⁻¹ Mpc⁻¹ based on available measurements at that time. This led to over or under-estimating the sizes of these sources and eventually, leading to inaccurate statistics of their population. With the advent of precision cosmology derived from the cosmic microwave background radiation observed with the Wilkinson Microwave Anisotropy Probe (WMAP; Hinshaw et al. 2013) and Planck mission (Planck Collaboration et al. 2016), the value of H_0 was set to ~ 68 ${\rm km~s^{-1}~Mpc^{-1}}$. The first GRGs discovered by Willis et al. (1974) were 3C236 and DA240, both of which are more than 2 Mpc in size and hence originally there was not a lower limit of size set for RGs to be classified as GRGs. Recent studies (Dabhade et al. 2017; Kuźmicz et al. 2018; Ursini et al. 2018; Dabhade et al. 2020) have adopted 700 kpc as the lower size limit of GRGs with the updated H₀ value.

In the last six decades, owing to radio surveys like the third Cambridge radio survey (3CR; Bennett 1962; Laing et al. 1983), Bologna Survey (B2; Colla et al. 1970), Faint Images of the Radio Sky at Twenty-Centimeters survey (FIRST; Becker et al. 1995), NRAO VLA Sky Survey (NVSS; Condon et al. 1998), Westerbork Northern Sky Survey (WENSS; Rengelink et al. 1997), Sydney University Molonglo Sky Survey (SUMSS; Bock et al. 1999), TIFR GMRT Sky Survey (TGSS; Intema et al. 2017) and LOFAR Two-metre Sky Survey (LoTSS; Shimwell et al. 2019), millions of RGs have been found and a considerable fraction has been studied in detail. However, only a few hundred of these RGs have turned out to be giants or GRGs, highlighting the rarity of this type of AGNs.

Over a course of nearly 45 years, about 40 research papers (Willis et al. 1974; Bridle et al. 1976; Laing et al. 1983; Kronberg et al. 1986; de Bruyn 1989; Jones 1989; Ekers et al. 1989; Lacy et al. 1993; Law-Green et al. 1995; Cotter et al. 1996; McCarthy et al. 1996; Subrahmanyan et al. 1996; Ishwara-Chandra & Saikia 1999; Lara et al. 2001; Machalski et al. 2001; Schoenmakers et al. 2001; Sadler et al. 2002; Letawe et al. 2004; Saripalli et al. 2005; Saikia et al. 2006; Machalski et al. 2007; Huynh et al. 2007; Machalski et al. 2008; Kozieł-Wierzbowska & Stasińska 2011; Hota et al. 2011; Solovyov & Verkhodanov 2014; Molina et al. 2014; Bagchi et al. 2014; Amirkhanyan et al. 2015; Tamhane et al. 2015; Amirkhanyan 2016; Dabhade et al. 2017; Clarke et al. 2017; Kapińska et al. 2017; Prescott et al. 2018; Sebastian et al. 2018; Kuźmicz et al. 2018; Kozieł-Wierzbowska et al. 2019; Dabhade et al. 2020) have reported about 662 GRGs spread all over the sky. This estimation is based on a database of GRGs compiled by us adopting 700 kpc as the lower limit of GRG size and using concordant cosmological parameters from Planck (H₀ = 67.8 km s⁻¹ Mpc⁻¹, $\Omega_{\rm m}$ = 0.308, Ω_{Λ} = 0.692; Planck Collaboration et al. 2016). Apart from the above which illustrates the rarity of GRGs, if we take a complete radio sample like the Third Cambridge Radio Survey (the 3CRR sample; Laing et al. 1983), the median size of the RGs/RQs is ~ 350 kpc, and only $\sim 7\%$ of the sample are GRGs.

Some of the open questions related to GRGs are:

- How do some GRGs grow to megaparsec scale sizes?
- How rare are GRGs?
- Do GRGs grow only in sparser environments?
- Do GRGs have the most powerful SMBHs?
- What is the accretion state, mass and spin of the central SMBH?
- Do GRGs contribute to any other large scale processes?

These cosmic behemoths bring forth some of the most puzzling and interesting aspects of relativistic jets, and SMBHs residing in active galaxies. The most favoured explanation for GRGs' exceptional size is these growing in sparser or low-density environments (Mack et al. 1998; Pirya et al. 2012; Malarecki et al. 2015; Saripalli & Malarecki 2015). However, contrary to this proposition, a few studies like Komberg & Pashchenko (2009) and Dabhade et al. (2017, 2020) have shown dozens of GRGs residing in dense cluster environments. Few other studies (Subrahmanyan et al. 1996; Saripalli et al. 2005; Bruni et al. 2019, 2020) have also shown that GRGs may attain their gigantic size due to the restarted AGN activity. However,

both the above mentioned explanations remain to be robustly tested for a statistically large sample.

It has also been suggested that GRGs contain exceptionally powerful "central engines" powered by massive black holes, which are responsible for their gigantic sizes (Gopal-Krishna et al. 1989). Therefore, based on the current understanding, we believe that environment alone cannot be the only determining factor for the giant size of GRGs, but possibly a combination of AGN power (including jet power and accretion states), environmental factors and the longevity of AGN activity (duty cycle) might be playing an equally important role.

Despite various studies of GRGs over the last five decades, the colossal physical scale and other extreme properties of GRGs remains to be explained by a complete physical model. It is unknown whether the large sizes of GRGs indicate the high efficiency of radio jets ejected from the central AGN or the effect of their location in sparser environments or a combination of both. Moreover, till now, multi-wavelength studies of only a small fraction of GRGs have been carried out, to specifically address the important questions related to their unusual nature. This has restricted a comprehensive statistical analysis of the properties of GRGs to understand their true nature.

In order to address the above questions via a systematic study of a large number of GRGs, we have initiated a project completely dedicated to the study of GRGs which we describe in the following parts of this paper along with our first results. In this work, for the first time, we have been able to obtain a good understanding of the GRG astrophysics, spanning an enormous range ($\sim 10^{11}$) of physical scales from $\sim 10^{-5}$ parsecs in the jet launch zone present in the vicinity of black hole to ~ 1 Mpc where the jet termination point is located.

The paper is organised as follows: In Sec. 2, an overview and goals of project SAGAN are presented. In Sec. 2.1, the search criteria and methodology for identifying the new GRG sample from the NVSS survey are described, followed by a discussion on the creation of a new database of GRGs in Sec. 2.2. In Sec. 3, we describe the analysis methods employed on multi-wavelength data of GRGs to estimate their various properties. Next, we present the results of the analysis along with their discussion and implications in Sec. 4, which is further sub-divided into several subsections, each dedicated to a property of GRGs. We end the main paper with the conclusion of our study on GRGs under project SAGAN and its future prospects in Sec. 7. Lastly, in Appendix Sec. A, we present three main tables consisting of the properties of our new GRG sample and in Appendix Sec. B, we show the multi-frequency radio maps of GRGs of our new sample.

Throughout this paper, the flat $\Lambda \mathrm{CDM}$ cosmological model is adopted based on the Planck results ($\mathrm{H_0}=67.8~\mathrm{km}~\mathrm{s^{-1}~Mpc^{-1}}$, $\Omega_\mathrm{m}=0.308$ and $\Omega_\Lambda=0.692$ Planck Collaboration et al. 2016), which gives a physical scale of 4.6 kpc/" for the redshift of 0.3. All the images are presented in a J2000 coordinate system. We use the convention $S_\nu \propto \nu^{-\alpha}$, where S_ν is the flux density at frequency ν and α is the spectral index.

2. Project SAGAN

To understand the physics of these extreme cosmic radio sources much better, and specifically address the key questions about them, we have initiated a project called SAGAN¹ (Search and Analysis of GRGs with Associated Nuclei), whose pilot study results were presented in the previous paper (Dabhade et al. 2017). Some of the main goals for this project are:

- 1. Create a complete and uniform database of GRGs from the literature spanning five decades using a single cosmological model with $H_0=67.8~{\rm km~s^{-1}~Mpc^{-1}},~\Omega_{\rm m}=0.308~{\rm and}~\Omega_{\Lambda}=0.692$ (flat $\Lambda{\rm CDM}$).
- 2. Search for more GRGs from existing radio and optical/infrared survey data.
- 3. Using the newly created large database of GRGs, carry out multi-wavelength studies of the host AGNs of the GRGs. We intend to focus on some key physical properties such as the accretion rate (\dot{m}) of the black hole, excitation type, black hole mass (M_{BH}), Eddington ratio, spin, host galaxy star formation rate (SFR), and high energy gamma-ray emission from jets.
- 4. Exploring effects of the environment on the morphology and growth of the GRGs.
- 5. Using Magneto-hydrodynamical (MHD) simulations to investigate the jet physics and the necessary conditions required for the collimation and stability of relativistic jets, propagating to megaparsec or larger physical distances from the host AGN.

Broadly the goal is to understand birth, growth and evolution of GRGs and their possible contribution to other processes in the Universe.

In this first paper, we present the results of our search for GRGs from the NVSS along with GRGs from other published works and investigate their multi-wavelength properties (in radio, optical and mid-infrared bands).

Here, we not only report a larger sample of 162 hitherto unidentified GRGs, but also shed light for the first time on their AGN and host galaxy physical properties.

2.1. New sample of GRGs from NVSS

The NVSS provides radio maps ($\delta > -40^{\circ}$, 82% of the sky) at 1400 MHz with a modest resolution of 45" and has rms (root mean square) brightness fluctuations of ~ 0.45 mJy beam⁻¹. The NVSS was released more than 20 years ago, yet it continues to be a source of many interesting discoveries (e.g. for GRGs- Solovyov & Verkhodanov 2011; Amirkhanyan 2016; Proctor 2016; Dabhade et al. 2017).

Proctor (2016) produced a catalogue of 1616 possible giant radio sources (GRSs) from automated pattern recognition techniques using NVSS data. This catalogue of 1616 sources represents the radio objects which are possible candidates for GRGs having their projected angular size $\geq 4'$. Therefore, this catalogue serves as a useful database to find new GRGs.

Following up our pilot study published in Dabhade et al. (2017), we further carried out our independent manual visual search for GRGs from the NVSS and the results of the search were combined with the fraction of GRGs we confirmed from the Proctor (2016) sample.

In order to confirm potential GRGs from Proctor's sample, we used the following radio surveys to decipher the true radio morphology of the sources:

¹ https://sites.google.com/site/anantasakyatta/sagan

- NVSS: It has a high sensitivity for large scale diffuse emission and is one of the best all-sky radio surveys till date.
- FIRST: This survey is at 1400 MHz with a resolution of $\sim 5''$ and 0.15 mJy beam⁻¹ rms. Its high resolution maps provide vital information of the radio cores and hotspots of the sources.
- TGSS: It is a low frequency radio survey at 150 MHz with a resolution of $\sim 25''$ and rms of ~ 3.5 mJy beam⁻¹, covering the entire NVSS footprint. It is sensitive to diffuse low radio frequency emission and particularly, good at detecting very steep spectrum sources.
- VLASS²: Very Large Array Sky Survey (Lacy et al. 2019): It is the most recent all sky radio survey at 3000 MHz with a resolution of $\sim 2.5''$ and rms of $\sim 100~\mu Jy$ covering the footprint same as that of the NVSS. This survey is deeper, has better resolution and covers more sky area when compared to the FIRST, and is very useful for deciphering sources in the southern sky up to declination of -40° .

Once the overall morphology of the sources was determined using the available above mentioned radio surveys, optical and mid-infrared (mid-IR) data from the Sloan Digital Sky Survey (SDSS; York et al. 2000; Abolfathi et al. 2018), the Panoramic Survey Telescope and Rapid Response System (Pan-STARRS; Kaiser et al. 2002, 2010; Chambers et al. 2016) and the Wide-field Infrared Survey Explorer (WISE; Wright et al. 2010) respectively, were used for identifying the host galaxies of the candidate GRGs.

The following steps and criteria were used to create the final sample of confirmed GRGs from Proctor (2016) GRS catalogue:

- 1. Optical/mid-IR and radio maps were overlaid to identify the host galaxy/AGN coinciding with the radio core. Sources which did not have radio core-host galaxy association were rejected.
- 2. We selected only those sources via thorough manual inspection whose various components (core/jets/lobes) were sufficiently resolved, with no ambiguity in their radio morphology.
- 3. All the sources selected by the above steps were checked for redshift (z) information of the host galaxy (photometric or spectroscopic) from publicly available optical surveys and databases.
- 4. The angular sizes of the sources were computed using NVSS radio maps for uniformity, and to ensure that there is no flux or structure loss which the other higher resolution radio surveys (FIRST, TGSS and VLASS) are prone to. We measured the largest angular separation of the two components (lobes/hotspots/tails/jets) of the sources after considering only the parts of the sources seen above 3σ . Hence, the angular sizes of all the sources were revised, and the angular extent of some sources came out to be < 4', which is the lower limit of Proctor (2016) sample.
- 5. Lastly, we made use of redshift and angular size information to compute the projected linear size of the sources, and only the ones greater than 700 kpc were considered for our GRG sample (SAGAN GRG Sample or SGS henceforth).

Table 1: Short summary of classification of sources from Proctor (2016).

Classification	No. of objects
Ambiguous morphology	156
Independent Sources	266
New GRGs	151
Known GRGs	165
Narrow Angle Tailed RGs	24
No core	143
No Host	20
No Redshift	311
RGs	311
Supernova Remnant	6
Spiral/disk Galaxies	32
Wide Angle Tailed RGs	31
Total	1616

The above steps resulted in identifying 151 new GRGs from Proctor (2016) sample. We also classified the rest of the sources into different categories, which can be useful to the scientific community for future work. The classification was done based on the availability of radio and optical data, which are given in Table 1. Many sources from our independent manual search were common in Proctor (2016) sample and a total of 11 GRGs were found to be unique (not in Proctor 2016 sample). Therefore after combining the two, we report our final sample (SGS) of 162 GRGs as seen in Table A.1. The sample is discussed in more details in Sec. 4.

The basic information of the SGS, namely right ascension (RA) and declination (Dec) of host galaxies in optical, AGN type (galaxy or quasar), redshift, angular size (arcminute), physical size or projected linear size (Mpc), flux density (mJy) and radio powers (W $\rm Hz^{-1}$) at 1400 MHz and 150 MHz, and spectral index with error estimates are presented in the Table A.1.

2.2. The GRG-catalogue

In order to explore and study the trends of GRG properties using a statistically significant sample, we have combined our SGS with all other known GRGs from literature (as of April 2020) given in Sec. 1, and we henceforth refer it as the 'GRG-catalogue' throughout this paper. The total number of GRGs in the GRG-catalogue, i.e. the total number of GRGs known till date is 820, and it is a unique complete compendium of known GRGs till date. In Fig. 1, we can see the distribution of all the known GRGs (including GRG sample of this paper) in the sky. The high concentration of GRGs seen in the northern region of the plot (right ascension 10h45m to 15h30m and declination $45^{\circ}00'$ to $57^{\circ}00'$) is primarily due to the recent discovery of a large sample of new GRGs (225) from the LoTSS by us (Dabhade et al. 2020), which has contributed about 30% to the known GRG population as seen in Fig. 2. Our reporting sample from this paper called the SGS has contributed an additional $\sim 20\%$ to the overall known population of GRGs. Thus we are contributing around 50% of all known GRGs till date.

We point out that in the present study, analysis has been restricted to 762/820 GRGs ($\sim 93\%$ of GRG-catalogue)

² https://archive-new.nrao.edu/vlass/HiPS/VLASS_ Epoch1/Quicklook/

Distribution of known 820 Giant Radio Galaxies on sky plane

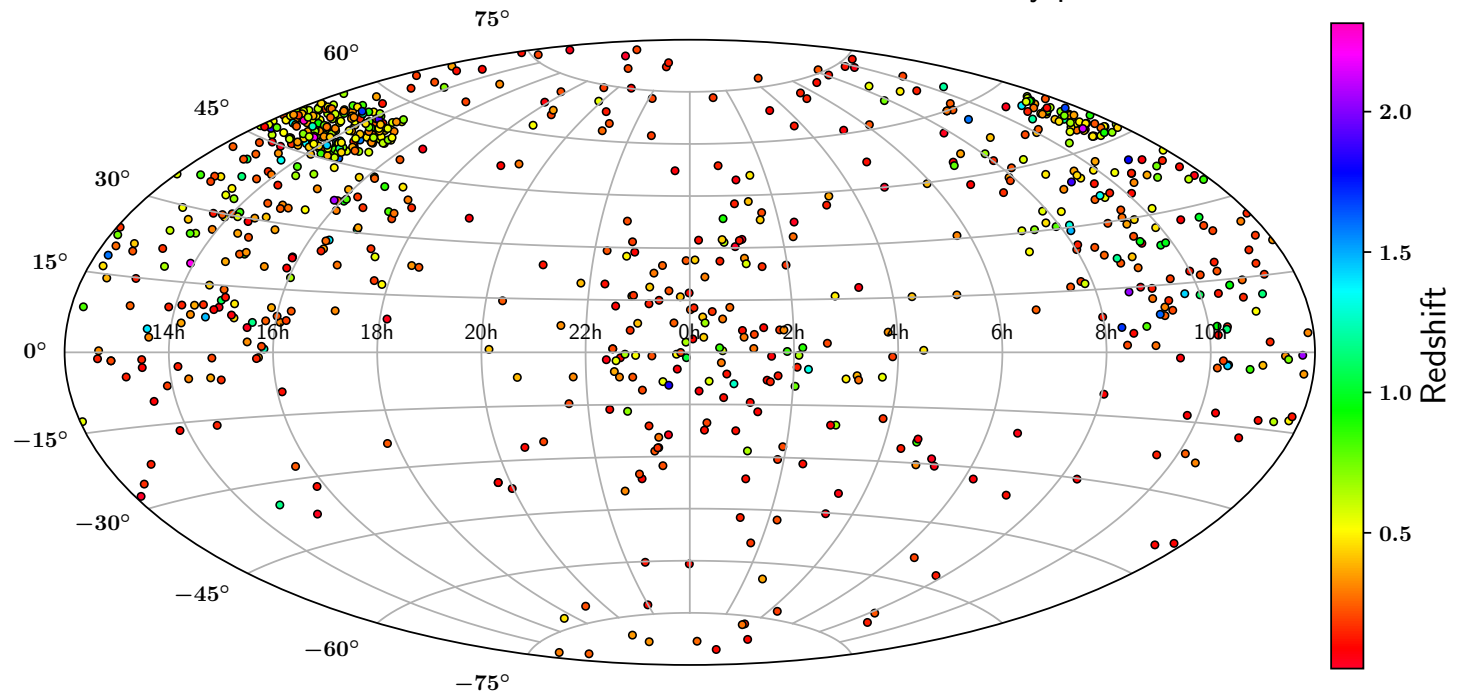


Fig. 1: The plot shows the sky distribution of all the known GRGs from the year 1974 to 2020 along with our SAGAN GRG sample in Aitoff projection. The total number of GRGs plotted here is 820 (LoTSS:225 + SAGAN:162 + all others from literature: 433). The large clustering of GRGs seen in the northern region of the plot (right ascension 10h45m to 15h30m and declination 45°00′ to 57°00′) is the result of the finding of large sample of GRGs (225) from the LoTSS by us (Dabhade et al. 2020). The colour of the points on the plot corresponds to their redshift indicated in the vertical colour bar on the right side of the plot. We do not make use of all the 820 GRGs for our analysis in this paper, but only the ones with (762 GRGs) redshift less than 1.

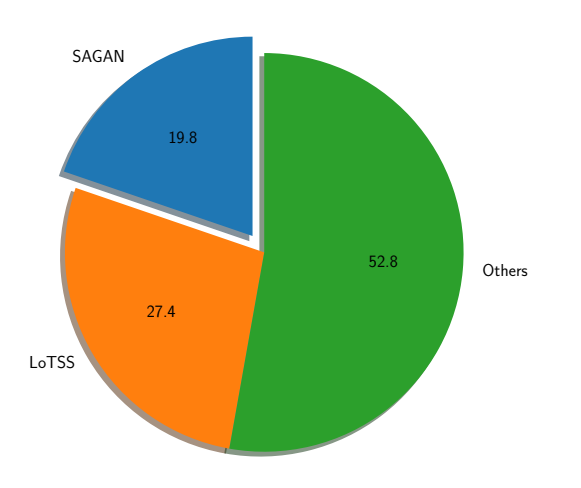


Fig. 2: Pie diagram representing the contribution of SGS (blue colour: $\sim 20\%$) and LoTSS-GRGs (orange colour: $\sim 27\%$) to the total GRG population. The green colour indicates the GRGs reported in the literature until March 2020. Here, we show all the known (820) sources without any filters.

and 61 GRGs with z>1 have not been considered to avoid any kind of bias. Beyond redshift of 1 we are limited by the unavailability of optical data as well as due to a strong evolution of radio source properties (luminosity and size) in the early cosmic epoch of z > 1. SGS, which is now part of the GRG-catalogue has all sources with z < 1.

3. Analysis

3.1. Size

The projected linear size of the sources is taken as the end to end distance between the two hotspots (peak fluxes) in case of FR-II sources, and for FR-Is, it is the distance between the maximum extents defined by the outer lobes. For the measurement of angular sizes, only the NVSS maps are considered for uniformity. The projected linear sizes of sources are estimated using the following formula, and are tabulated in Table. A.1 (column 8):

$$D = \frac{\theta \times D_c}{(1+z)} \times \frac{\pi}{10800} \tag{1}$$

where θ is the angular extent of the GRG in the sky in units of arcminutes, D_c is the comoving distance in Mpc, z is the GRG host galaxy's redshift, and D is projected linear size of the GRG in Mpc.

3.2. Flux density & Radio Power

The integrated flux density of GRGs was estimated using Common Astronomy Software Applications (CASA) (McMullin et al. 2007) with the task CASA-VIEWER by manually selecting the regions of emission associated with each

GRG in NVSS³ and TGSS⁴ maps. The TGSS maps were convolved to the resolution of NVSS. We use the scheme of Klein et al. (2003) for measuring flux density errors for each source, where we have adopted the values of 3% and 20% flux calibration errors, mentioned in the literature for the NVSS and the TGSS respectively.

Radio powers of GRGs were calculated using the formula and are given in Table. A.1 (column 10 and 12):

$$P_{\nu} = 4\pi D_{L}^{2} S_{\nu} (1+z)^{\alpha-1}$$
 (2)

where D_L is the luminosity distance, S_{ν} is the measured radio flux density at frequency ν , $(1+z)^{\alpha-1}$ is the standard k-correction term, and α is the radio spectral index.

3.3. Jet Kinetic Power

AGN jets, made of relativistic charged particles and magnetic fields emanate out of the central engine and pierce through the interstellar medium. Observations allow us to estimate the jet kinetic power, which is a key messenger of characteristics of the radio-loud SMBH system, i.e. mass, spin, accretion rate and the magnetic field (further discussed in detail below). High radio frequencies ($\sim 1~\rm GHz)$ are ideal for observing nuclear jet components owing to their flatter spectral nature. Since these components have large velocities, relativistic effects like the Doppler enhancement effects are prominent. Therefore, lower radio frequencies are more suitable for probing the jet kinetic power due to negligible contribution from Doppler enhancement. We have used the following relation from simulation based analytical model of Hardcastle (2018b) to estimate jet kinetic power:

$$L_{150} = 3 \times 10^{27} \frac{Q_{\rm Jet}}{10^{38} \ W} \rm Hz^{-1} \eqno(3)$$

where L_{150} is the radio luminosity at 150 MHz at which Doppler boosting is negligible, and Q_{Jet} is the jet kinetic power. Hardcastle (2018b) has also considered the environmental and age factors in their model, via which the Q_{Jet} was obtained. They have shown that by doing so the accuracy of the result increases, and the results are consistent with the findings of Willott et al. (1999). Sources in the GRG-catalogue coming from Dabhade et al. (2020) GRG sample have flux density measurements at 144 MHz from LoTSS, which is used to derive the 150 MHz radio luminosity. The TGSS was used for the rest of the sources in the GRG-catalogue for obtaining the 150 MHz radio luminosity. This was mainly done for our newly found SGS, and only sources with full structure detection in TGSS were considered for the same. The results obtained are presented in column 8 of Table A.2.

3.4. Spectral Index (α)

For a radio source, its spectral index (α) represents the energy distribution of the relativistic electrons (Scheuer & Williams 1968) and therefore its measurement ideally should involve covering wide frequency range. Studies have shown that α correlates with radio power and redshift. For synchrotron radiation, unless being affected by radiative

losses and optical depth effects, it is well known that radio flux density varies with frequency as $S_{\nu} \propto \nu^{-\alpha}$ resulting into two-point spectral index measurement, given as follows:

$$\alpha = \frac{\ln S_{\nu_1} - \ln S_{\nu_2}}{\ln \nu_2 - \ln \nu_1} \tag{4}$$

The integrated spectral index between 150 and 1400 MHz (α_{150}^{1400}) for the GRGs was computed using the TGSS and the NVSS radio maps (Table. A.1: column 13). We do not include GRGs with incomplete structure detection in the TGSS for the α_{150}^{1400} studies. For these sources, the α_{150}^{1400} is assumed to be 0.75 for the determination of the radio power at 1400 MHz (P₁₄₀₀). See Sec. 4.2 and Sec. 5.1.4 for more discussion.

For sources SAGANJ090111.78+294338.00 and SAGANJ091942.21+260923.97, TGSS data is absent as they fall in sky area which is not covered in TGSS-ADR-1. Therefore, no spectral index measurements were possible for them.

3.5. Absolute r-band magnitude

Using SDSS, we obtained the apparent r-band magnitudes (m_r) of hosts of GRGs for the SGS as well as for all the other objects in the GRG-catalogue. The absolute r-band magnitudes (M_r) of galaxies were computed after applying the k-correction on extinction corrected r-band apparent magnitudes (m_r) of SDSS. The k-correction is computed using K-CORRECT v4.3 software (Blanton & Roweis 2007) for rest frame at z=0. Column 5 of Table A.1 shows m_r of sources from SGS.

3.6. Black Hole mass

We have estimated the black hole masses associated with the AGNS in the host galaxies of GRGs using M_{BH} - σ relation. The M_{BH} - σ relation is based on a strong correlation between the central galactic black hole mass (M_{BH}) and the effective stellar velocity dispersion (σ) in the galactic bulge (Ferrarese & Merritt 2000; Gebhardt et al. 2000) given by,

$$\log\left(\frac{M_{BH}}{M_{\odot}}\right) = \alpha + \beta \log\left(\frac{\sigma}{200 \text{ km s}^{-1}}\right)$$
 (5)

where $\alpha=-0.510\pm0.049$ and $\beta=4.377\pm0.290$ (Kormendy & Ho 2013). Estimates for σ (column 4 of Table A.2) were available for only 46 host galaxies of GRGs from SGS in SDSS, and hence the $M_{\rm BH}$ of GRGs (Table. A.2: column 5) could be computed via this method.

3.7. Eddington Ratio

Dimensionless Eddington ratio ($\lambda_{\rm Edd}$) is the ratio of bolometric luminosity of the AGN to the maximal Eddington luminosity, which in turn is the estimation of the accretion rate of the SMBH in terms of Eddington accretion rate and the radiative efficiency of the accretion state (Note: It is also denoted as $l_{\rm rad}$ in other literature). In case of accreting black holes, not all the energy brought in by the accretion flow has to appear as radiative luminosity or jet power, since significant energy can be lost through the event horizon, consumed by the black hole. Eddington ratio is expressed

³ https://www.cv.nrao.edu/nvss/postage.shtml

⁴ https://vo.astron.nl/tgssadr/q_fits/cutout/form

by the following relation:

$$\lambda \equiv \frac{L_{\rm bol}}{L_{\rm Edd}} \tag{6}$$

where $L_{\rm bol}$ represents the bolometric luminosity, and the Eddington luminosity is $L_{\rm Edd}.$ The $L_{\rm bol}$ is calculated from the luminosity of [OIII] emission line, using the relation: $L_{\rm bol}=3500\times L_{\rm [OIII]}$ (Heckman et al. 2004). The values of $\lambda_{\rm Edd}$ are tabulated in column 7 of Table. A.2. The Eddington luminosity (also known as the Eddington limit) is derived from black hole mass, and it is the maximum luminosity, an object could have, when there is a balance between the force of radiation acting outward and the gravitational force acting inward. The equation of Eddington luminosity for pure ionised hydrogen plasma is $L_{\rm Edd}=1.3\times10^{38}\times(\frac{M_{\rm BH}}{M_{\odot}})~{\rm erg~s^{-1}}.$

3.8. Black Hole Spin

Spin and angular momentum (a and J) are fundamental properties of black holes along with mass, which can help us reconstruct the history of mergers and accretion activity (Hughes & Blandford 2003; Volonteri et al. 2007; King et al. 2008; Daly 2011), occurring in the central engine in the past billions of years and thus, paving a way to understanding the energetic astrophysical jets. In the B-Z model, the relativistic jet is the outcome of the combined effect of rotation (frame dragging) and accumulated magnetic field near the black hole (Blandford & Znajek 1977), which is fed matter by a rotating accretion disk surrounding it. In the alternate model of Blandford & Payne (1982) (B-P mechanism), the jet power can be sourced from the rotation of the accretion disk with the help magnetic threading, without invoking a spinning black hole. However, in both the processes the intensity and geometry of the poloidal component of the magnetic field near the black hole horizon strongly influence the Poynting flux of the emergent jet (Beckwith et al. 2008).

According to B-Z model (Blandford & Znajek 1977; Blandford 1990), a relationship between the jet power (Q_{Jet}), the black hole mass (M_{BH}), the black hole dimensionless spin ($a=Jc/(GM^2)$), and the poloidal magnetic field (B) threading the accretion disk and ergosphere take the following form:

$$Q_{\rm Jet} \propto B^2 M_{\rm BH}^2 a^2 \tag{7}$$

where $Q_{\rm Jet}$ is in units of 10^{44} erg s⁻¹, B is in units of 10^4 G, $M_{\rm BH}$ is in units of 10^8 M_{\odot} and 'a' is the dimensionless spin parameter ($a{=}0$ refers to a non-rotating black hole and $a{=}1$ is a maximally spinning black hole). The spin (a) can be quantified using the above relation once the other contributing parameters are known or fixed. The constant of proportionality is taken to be $\sim \sqrt{0.5}$ as in the B-Z model. Owing to the challenges of estimating the magnetic field of the vicinity of the black hole to compute spin, we consider the Eddington magnetic field strength ($B_{\rm Edd}$) (Beskin 2010; Daly 2011), which is as follows:

$$B \sim B_{\rm Edd} \approx 6 \times 10^4 \left(\frac{M_{\rm BH}}{10^8 M_{\odot}}\right)^{-1/2} {\rm Gauss}$$
 (8)

This is the upper limit of magnetic field strength close to the central engine, and it is based on the assumption that the magnetic field energy density balances the total energy density of the accreting plasma having a radiation field of Eddington luminosity.

The X-ray reflection is the most robust and effective technique employed till date to estimate the spin of black holes (Reynolds 2019). However, owing to the weakness of the signal and need of richness of the data for the objects it has been done convincingly only for $\sim\!20$ sources till now. For radio galaxies which are jetted sources and mostly show weak X-ray reflection signatures, it is possible to estimate the spin assuming the B-Z mechanism (Daly 2011; Mikhailov & Gnedin 2018). In this radio driven method, the spin (a) of the black hole can be estimated if we have estimates of $\rm M_{BH}$ and $\rm Q_{Jet}$ along with adopting $\rm B_{Edd}$ as B. This method provides an indirect estimate of the spin of the black hole.

3.9. WISE Mid Infrared properties

We use the WISE survey to study the hosts of GRGs at mid-infrared (mid-IR) wavelengths. WISE, which is a space-based telescope, carried out an all-sky survey in four mid-IR bands [W1 $(3.4\mu\text{m})$, W2 $(4.6\mu\text{m})$, W3 $(12\mu\text{m})$, W4 $(22\mu\text{m})$] with an angular resolution of 6.1'', 6.4'', 6.5'' and 12'' respectively.

Using the mid-IR colours, we obtained the properties of possible dust obscured AGN, and estimated its radiative efficiency. The mid-IR information of hosts of GRGs is very useful in gauging the radiative efficiency because the optical-UV radiation from the accretion disk of the AGN is absorbed by the surrounding dusty torus (if present) and is re-radiated in mid-IR wavelengths. Moreover, it has been shown in literature that WISE mid-IR colours can effectively distinguish AGNs from star-forming and passive galaxies, and within the AGN subset itself high-excitation radio galaxies (HERGs) and low-excitation radio galaxies (LERG) stand out on the mid-IR colour-colour and mid-IRradio plots (Stern et al. 2012; Gürkan et al. 2014). Therefore, in the absence of any dedicated multi-wavelength survey of hosts of GRGs, WISE data is ideal for exploring GRGs properties.

The WISE All–Sky Source Catalogue was used to obtain magnitudes of the hosts of GRGs in the four mid-IR bands. After applying photometric quality cuts of 3σ , reliable mid-IR magnitudes were obtained for sources in the GRG–catalogue. Upper limits of the magnitudes in relevant bands were estimated for sources which did not have 3σ detection via a method prescribed in WISE documentation.

We employ the scheme from Mingo et al. (2016), which is based on the earlier work of Wright et al. (2010), Lake et al. (2012) and Gürkan et al. (2014), to classify the host-AGN and host-galaxies of GRGs into Low Excitation Radio Galaxies (LERGs), High Excitation Radio Galaxies (HERGs), quasars (QSOs), star-forming galaxies (SFGs), and Ultra-Luminous Infrared Radio Galaxies (ULIRGs).

Fig. 3 is a colour-colour plot using four mid-IR bands [W1 (3.4 μ m), W2 (4.6 μ m), W3 (12 μ m), W4 (22 μ m)] which not only shows the distinction between LERGs and HERGs but also effectively distinguish AGNs from star-forming and passive galaxies. The Fig. 3 includes 733 sources from GRG-catalogue based on the availability of data and detection in WISE database. It has been marked into 4 regions, which signify the following:

- 1. Region I: HERGs and quasars (W1 W2 $\geqslant 0.5$, W2 W3 < 5.1)- this region consists of 250 GRGs of which 103 are hosted by quasars.
- 2. Region II: LERGs (W1 W2 < 0.5 , 0 < W2 W3 < 1.6)- there are 153 sources in this region.
- 3. Region III: LERGs and star-forming galaxies (W1 W2 <0.5 , $1.6 \le$ W2 W3 < 3.4)- 297 giants lie in this region.
- 4. Region IV: ULIRGs (W1 W2 < 0.5 , W2 W3 \geq 3.4)- only 33 sources are there in this region.

Fig. 3 shows that hosts of GRGs reveal a variety of AGN excitation types similar to that of RGs. This also indicates that the host galaxy or the AGN of GRGs do not preferentially show any specific AGN excitation type. Quasars in this plot are not identified via this method but have been previously classified from SDSS and other available literature data. Similar results were presented in Dabhade et al. (2017) but with a much smaller sample. Now, in this paper, we have placed almost the entire GRG-catalogue on the WISE colour-colour plot for AGN diagnostic and classified the known GRG population into their excitation types. We have focused on low and high excitation part of the classification and efforts were put to ensure a clean classification. For a sub-sample (based on the availability of data), we have also compared our LERG and HERG classification of GRGs from WISE with the classification method based on emission line ratios and found them to be consistent with each other.

Here on throughout the paper, the GRGs with low and high excitation types will be referred to as LEGRG and HEGRG, respectively. Since region-III and region-IV of Fig. 3 have both mixed population of LERGs as well as star-forming galaxies and ULIRGs respectively (thereby confusing the classification), we do not consider objects in these regions for our analysis, and consider only sources in region-II to be LEGRGs to make a clean sample. Similarly, from the region-I we exclude known quasars and create HEGRG sample for our analysis. Both the above criteria reduce the number of objects available for our further analysis.

4. SAGAN GRG Sample (SGS): Results

The classification of the sources in SAGAN GRG Sample (SGS) is shown in Table. 2 below. Out of 162 GRGs, 23 sources are found to be hosted by galaxies with quasars as their AGN (henceforth they will be referred to as GRQs). The quasar nature of these 23 GRQs is identified using the spectroscopic data from SDSS, Pâris et al. (2018) and other available literature data. All the GRGs have been detected in the redshift range of ~ 0.03 - 0.95, with projected linear sizes varying from $\sim\!0.71$ - 2.82 Mpc. Three GRGs in our sample have projected linear sizes ≥ 2 Mpc.

Table 2: Summary of classified sources.

-	
Types	No.
GRQ	23
BCG	18
FRI	8
FRII	149
HyMoRS	4
m DDRG	1

4.1. Notes on individual sources from SGS

Here we present our findings and important notes related to some interesting GRGs from our sample.

- SAGANJ000450.25+124840.10 & SAGANJ011341.11+010608.52- Both these sources show two symmetric winged back-flows emanating out from the two hotspots and therefore, they can be referred to as X-shaped radio galaxies. For X-shaped radio galaxies there are three models, namely i) Twin AGN model, ii) Rapid Jet Reorientation Models, and iii) Back-flow diversion model, proposed to explain this phenomenon in RGs. After inspecting high resolution maps of FIRST and VLASS, we found no evidence of the presence of twin AGN at the core. However, our observations support the model that the pair of wings arise from the diversion of synchrotron plasma from the hotspots due to ambient pressure gradient.
- **SAGANJ075931.84+082534.59** The radio core of the source is only detected at 3000 MHz high resolution survey VLASS (2''). It coincides with a galaxy at a redshift of 0.124 with an r-band magnitude of 17.31. The diffuse plasma, spread along the jet axis on either side of the core is seen properly in the NVSS but partially well in the TGSS as seen in Fig. B.3. Thus, the overall intricacies of this object make it a good candidate for a remnant radio-loud AGN (Parma et al. 2007; Mahatma et al. 2018) with a projected linear size of ~ 0.72 Mpc. This is likely to be a young active source with a fading plasma from the earlier activity of the source. The integrated two-point spectral index of ~ 0.68 also supports the above argument. This source is important in order to understand the last phase of the duty cycle of AGN activity after the jets have switched off.
- **SAGANJ105309.33+260142.13** Contamination is observed near the western side of the core, which is quite clear in the contours of FIRST in the montage Fig. B.4. The measured flux density at 1400 MHz (NVSS) is 336.2 mJy which includes the flux density of the contaminating source (henceforth source A). For source A, using FIRST, where it is sufficiently resolved, we estimate a flux density of 21.6 mJy, and subtracting this value from the total measured flux density, we obtain the corrected flux density value of 314.6 mJy. A similar method is followed for flux density correction at 150 MHz (TGSS). Since source A is not sufficiently resolved in TGSS map, the 3σ contours of the source from the FIRST map is overlaid on the TGSS map, and the flux density of the corresponding region (3σ) is considered to be the flux density of source A in TGSS. The respective value (77.9) mJy) is then subtracted from the measured flux density (1688.3 mJy) of the source, and therefore, the corrected flux density is 1610.4 mJy as given in Table A.1. Both the corrected flux densities at the respective frequencies are used for further calculations of radio power.
- SAGANJ112422.77+150957.90- It is the only Double-Double Radio Galaxy (DDRG) identified in our sample of 162 GRGs based on the available radio maps. The DDRG clearly displays aligned radio components, consisting of radio core, two inner and two outer lobes. The double-double morphology is prominently seen in the montage Fig. B.4 where images from the NVSS (45"), TGSS (25") and FIRST (5") are overlaid. The outer lobes are well detected in the NVSS (1400 MHz),

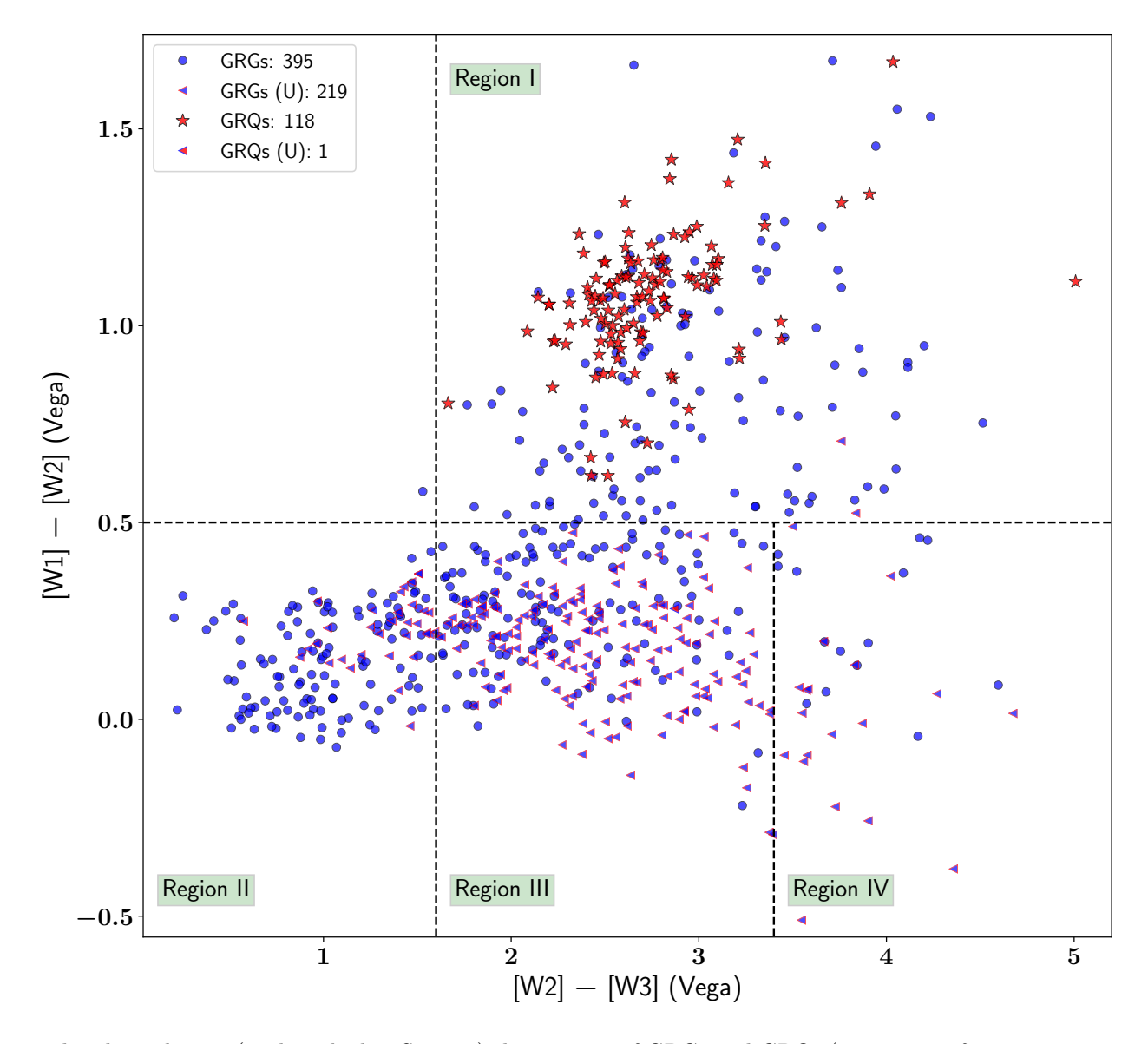


Fig. 3: The plot indicates (as described in Sec. 3.9) the position of GRGs and GRQs (733 sources from GRG-catalogue) on the mid-IR colour-colour plot using WISE mid-IR magnitudes (W1, W2, W3 and W4 have 3.4, 4.6, 12 and 22 μ m Vega magnitudes, respectively). It includes the objects from GRG-catalogue. Region-I: [W1]-[W2] \geq 0.5, [W2]-[W3] < 5.1 is mostly occupied by HERGs and quasars. Region-II: objects which have [W1]-[W2] < 0.5 and 0 < [W2]-[W3] < 1.6 are basically LERGs. Region-III: Star-forming galaxies and LERGs lie mostly in this region ([W1]-[W2] < 0.5, 1.6 \leq [W2]-[W3] < 3.4). Region-IV: ULIRGs lie in the region of [W1]-[W2] < 0.5 , [W2]-[W3] \geqslant 3.4. All the sources have z < 1. The 'triangle' symbol in the plot and 'U' in the legend indicates the upper limits of the W3 magnitudes.

but the inner structure is unresolved there. In the TGSS (150 MHz), there is a hint of detection of both outer and inner components of the source, but they are not bright enough for the confirmation of DDRG nature. However, the high resolution FIRST map confirms the inner structure showing the two inner lobes having edge brightened FR-II morphology, and VLASS (3000 MHz) with its higher resolution of 2" clearly reveals the radio core. Due to relatively low surface brightness sensitivity, the FIRST (1400 MHz) and VLASS (3000 MHz) surveys have resolved out the outer components of the source. The inner doubles are very compact as compared to the outer ones. The two outer hotspots are quite prominent in the NVSS map, and a winged flow is observed coming out from the northern hotspot. The angular size of the

inner double is 0.82' projecting a linear size of ~ 0.15 Mpc whereas the outer double spans up to ~ 0.92 Mpc. The radio core of the DDRG coincides with an optical galaxy with r-band magnitude of 16.36. This source has been classified as DDRG by Kozieł-Wierzbowska et al. (2019).

- SAGANJ114427.19+370831.87- A winged backflow is observed to emanate from the northern hotspot, but no such feature is seen near the southern hotspot. However, this source has been classified as X-shaped radio galaxy by Kozieł-Wierzbowska et al. (2019).
- SAGANJ225321.28+162016.77- The source has been mentioned in Solovyov & Verkhodanov (2014) as a candidate GRG.

4.2. Spectral Index Distribution of SGS

We were able to estimate the α_{150}^{1400} for a total of 123 from SGS, of which 18 are GRQs (See column 13 of Table A.1). For the remaining 39 sources in SGS, there was only partial or no detection in TGSS, and hence we have assumed the spectral index to be 0.75 for the calculation of P₁₄₀₀. Therefore, the α_{150}^{1400} data for the remaining 39 sources is not included for further studies in this paper. The median value of the α_{150}^{1400} for our sample's GRGs (0.69 \pm 0.02) is similar to that of GRQs (0.69 \pm 0.04). Dabhade et al. (2020) also find the α_{150}^{1400} of GRGs and GRQs to be similar with almost similar sample size. However, since their sample is chosen from a low frequency survey like the LoTSS, they find it to be slighter steeper than our SGS.

4.3. The PD $z\alpha$ parameters of GRGs

We investigate here the correlation between various properties of sources in our sample, such as radio power (P), projected linear size (D), redshift (z), and spectral index (α) (Fig. 4). The inferences are presented below:

- 1. Radio Power (P) vs Redshift (z): Fig. 4 (a) represents the distribution of GRGs on the P-z plane with radio power spanning over three orders of magnitude upto a redshift range of ~ 0.95 . Most of the sources are within the redshift range of 0.1 to 0.5, and the number of radio sources decreases with increase in redshift beyond z=0.5.
 - The non-availability of sources in the lower right quadrant is most likely due to the non-detection of low powered sources at high redshift due to the sensitivity limit of the survey, known as Malmquist bias. The GRQs have occupied the high radio luminosity and high redshift regime due to availability of optical data as compared to GRGs. The weakest source in our sample is SAGANJ090640.80+142522.97 with a flux density of ~ 24 mJy at 1400 MHz. The dashed line represents the minimum luminosity at different redshifts, corresponding to a minimum flux density of $\sim 24 \text{mJy}$ assuming a spectral index of 0.75. This is the NVSS's limit for detecting objects with low surface brightness and hence the absence of any source below this line. Recently, Dabhade et al. (2020) discovered a large sample of new GRGs, and significant fractions of those were of low luminosity. If we place them on Fig. 4 (a) then they tend to lie below the drawn line due to LoTSS's higher sensitivity.
- 2. Radio Power (P) vs Linear Size (D): The linear sizes of the radio sources have been plotted against their radio power, measured at 1400 MHz as shown in Fig. 4 (b). This plot is the radio astronomers equivalent of the traditional Hertzsprung-Russell diagram and is commonly known as the P-D diagram. We can draw the following conclusions from this diagram:
 - Despite the systematic search for giants, very few sources are found to be of extremely large size and very low radio power ($\leq 10^{24} \mathrm{~W~Hz^{-1}}$ at 1400 MHz).
 - The upper right region of PD diagram i.e the region of sources having high radio power and large linear size is devoid of any source which is indicative of an increase of radiative losses as the sources grow, lowering surface brightness, making them inaccessi-

- ble to the surveying telescope due to its sensitivity limit.
- There is a sudden drop in the number of giants with a linear size beyond 2 Mpc. Only three sources, i.e. SAGANJ064408.04+104341.40, SAGANJ225934.13+082040.78 SAGANJ231622.32+224650.28 inour sample, have their projected linear sizes exceeding 2 Mpc. All of them have low redshifts with the highest being 0.405 of the source SAGANJ225934.13+082040.78. Only 66 among ~ 762 known GRGs from the GRG-catalogue (z < 1) have projected linear size greater than 2 Mpc. Among them, four sources have extraordinary large linear sizes between 3 to 4 Mpc, while another four sources have linear sizes > 4 Mpc and the largest GRG known till date spans up to 5.2 Mpc at the redshift of 0.3067 (Machalski et al. 2008). Around 50% of the sources are at low redshifts ($z \le 0.4$), and the high redshift objects are mostly dominated by quasars. This could be attributed to the sensitivity limit of radio surveys. Another possibility might be the limited lifetime of radio sources (Schoenmakers et al. 2001). A large fraction of sources possibly are switched off before they reach 2 Mpc and beyond.
- 3. Linear Size (D) vs Redshift (z): The plot in Fig. 4 (c) shows the positive correlation between sizes of our sources with redshift, which is as expected since luminosity strongly correlates with both the parameters. At high redshift, as the sources grow, the increased radiative losses make them undetectable at radio wavelengths at their early stage of life. However, a negative correlation between linear size and redshift is observed by Miley & De Breuck (2008) due to the systematic increase of density of environment at earlier epochs (Athreya & Kapahi 1998; Klamer et al. 2006).
- 4. Radio Power (P) vs Spectral Index (α): The hotspots being the major contributors in the total flux density of powerful sources, play a crucial role in determining the nature of the relationship between the spectral index and radio power. We can see from Fig. 4 (d) that the spectral index increases with radio power. The correlation is significant for our sources, which are selected at high frequency (1400 MHz), similar to the results of Laing & Peacock (1980) for extended sources. It is also consistent with results of Blundell et al. (1999), who mentioned that the spectra of hotspots in powerful radio sources are steeper than those in less powerful radio sources. Sources with high Q_{Jet} form powerful hotspots with enhanced magnetic fields (Klamer et al. 2006), which in turn leads to the rapid synchrotron cooling of relativistic electrons (cooling time $\tau \propto 1/B^2$). This eventually results in an increase of synchrotron losses, and thus, electrons with steeper energy distribution are injected into the lobes.
- 5. Redshift (z) vs Spectral index (α) : We observe from Fig. 4 (e) that at higher z we get relatively steeper α . although there is a large scatter and sources with steep spectra are also seen at low redshifts. The possible explanations for our results could be the following:
 - At higher redshifts, the circum-galactic medium is denser. While traversing through this dense medium, most powerful jets undergo multiple shocks as a result of which the speed of the hotspots as well as the

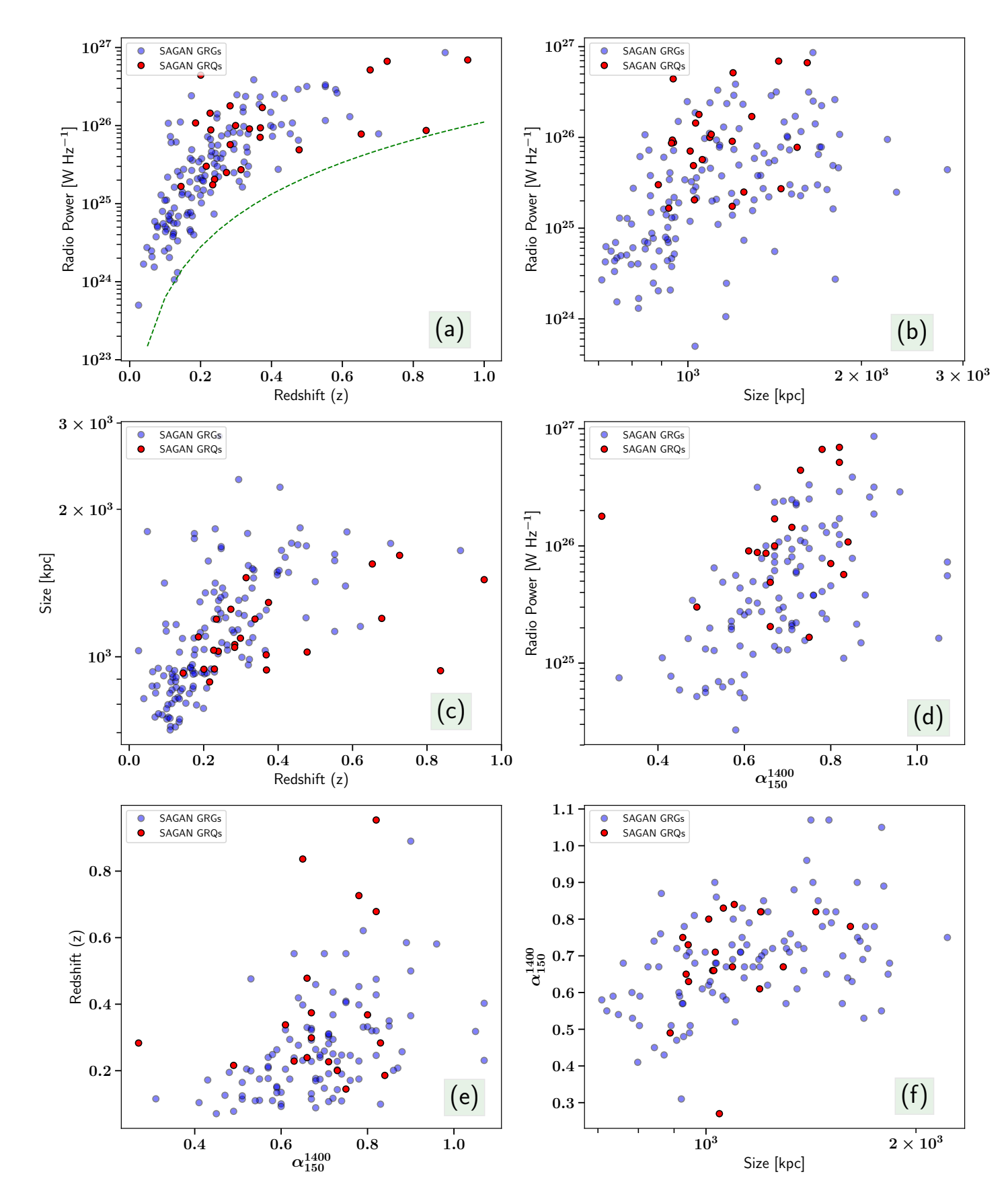


Fig. 4: Correlations amongst radio power [W Hz^{-1}] at 1400 MHz , size [kpc], redshift and spectral index for GRGs and GRQs. Red circles indicate GRQs while blue circles indicate GRGs. The green dashed line in the sub-figure (a) represents the minimum radio luminosity corresponding to flux density $\sim 24 \text{mJy}$ of source SAGANJ090640.80+142522.97 at different redshifts, assuming a spectral index of 0.75.

jet material slows down. A reduction in the velocity would result in the production of electrons with steeper energy distribution (Kirk & Schneider 1987; Athreya & Kapahi 1998).

- As the redshift increases, there is a rapid increment in the energy density of the cosmic microwave background radiation (CMBR energy density $\propto (1+z)^4$). When the high energy electrons of plasma interact with the CMBR photons, energy loss due to inverse Compton radiation increases and thus, the spectra steepens (Krolik & Chen 1991; Athreya & Kapahi 1998).
- 6. Spectral Index (α) vs Linear Size (D): The sampling of the sources in the D α plane in Fig. 4 (f), shows a weak correlation between the two parameters. The larger the sources grow, the steeper is their spectral index. As the sources grow, they are subjected to adiabatic expansion losses and decrease of magnetic fields in the lobes, and thereby, steepening the energy distribution. However, it is also reflected in the plot that sources with large linear size need not have steep spectra. This result is consistent with the findings of Blundell et al. (1999).

4.4. Morphology of GRGs

Using combined information from the VLASS, FIRST, NVSS and TGSS, we have classified GRGs in our sample into FR-I, FR-II, HyMoRS and DDRG.

HyMoRS are RGs with hybrid morphology (Saikia et al. 1996; Gopal-Krishna & Wiita 2000) which exhibits FR-I morphology on one side and FR-II on another side of the radio core. This classification can be seen in the $15^{\rm th}$ column of Table A.1, where HM refers to GRGs which are candidates for HyMoRS. Higher resolution radio maps are needed to confirm the morphology of the 4 HyMoRS candidate GRGs. For HyMoRS candidates, the range of radio powers is $P_{1400}\sim2.74\times10^{24}~W~Hz^{-1}$ - $7.78\times10^{25}~W$ $\mathrm{Hz^{-1}}$. The most significant result is that about $\sim 92\%$ of GRGs in SGS show FR-II type (edge brightened hotspots within radio lobes) of radio morphology, whereas only 8/162 GRGs show FR-I type radio morphology. The radio powers (P_{1400}) for FR-I type GRG range from $\sim 1.31 \times 10^{24}$ W ${\rm Hz^{-1}}$ - 11.1 \times 10²⁵ W Hz⁻¹, and for FR-II type GRGs the range is from \sim 0.5 \times 10²⁴ to 8.6 \times 10²⁶. Recently, Dabhade et al. (2020) using LoTSS also found the similar result of most of the GRGs having FR-II type morphology. Also, Mingo et al. (2019) using the LoTSS showed that there is a significant overlap in radio powers of FR-I and FR-II type RGs and also presented a new sample of low luminosity FR-II type RGs.

4.5. Environmental analysis of SGS

We cross-matched SGS with one of the largest catalogues of galaxy clusters - the WHL catalogue (Wen et al. 2012). This resulted in the finding of 18 GRGs from SGS to be Brightest Cluster Galaxies (BCGs), listed in Table A.4. The mass (M_{200}) and virial radius (r_{200}) were obtained from Wen et al. (2012) of the clusters, and are listed in the Table A.4 for all the corresponding 18 GRGs. The size is expressed as r_{200} , which is the radius within which the galaxy cluster's mean density is about 200 times of the critical density of the universe, and the mass of the cluster within r_{200} is denoted by M_{200} . We consider the sizes of these 18 GRGs along with

111 non BCG-GRGs from our sample in the same redshift range (0.063 - 0.369) with median redshifts of 0.174 and 0.205 respectively. We find that the median values for sizes of BCG-GRGs and non BCG-GRGs are 0.92 Mpc and 1.03 Mpc, respectively. Even though the median values do not vary largely, it is indicating that BCG-GRGs have smaller sizes compared to non-BCGs or in other words, the immediate environment plays an active role in curtailing their growth.

5. GRG-catalogue: Properties and Correlations

Here, we describe the derived properties of GRGs consisting of 762 sources with z < 1 using the multi-wavelength data.

Our multi-wavelength analysis is divided into the following three parts to understand the nature of GRGs, and we investigate the key astrophysical factors governing their growth to megaparsec scales:

- Studying differences in AGN types of GRGs: Quasars powering giant radio structures (jets and/or lobes) are called GRQs, which constitute less than 20% of the total known GRG population. The aim is to understand the key differences between giants hosted by quasars and non-quasar AGN. Their properties like size, $P_{1400},\,Q_{\rm Jet},$ and α_{150}^{1400} are compared and discussed in Sec. 5.1.
- Studying accretion states (LEGRG/HEGRG) of central nuclei of GRGs: These two sub-classes are investigated and discussed in Sec. 5.2 in context of their properties like size, P₁₄₀₀, Q_{Jet}, M_r, M_{BH} and λ_{Edd}.
 Studying similarities and dissimilarities between RGs
- Studying similarities and dissimilarities between RGs and GRGs: This is done by comparing their α_{150}^{1400} , M_{BH} and λ_{Edd} properties, and the findings are discussed in Sec. 5.3.

To test whether two samples in comparison come from the same distribution or not we use the two-sample Kolmogorov-Smirnov (K-S) test (Kolmogorov 1933; Smirnov 1948; Peacock 1983). In this we test the null hypothesis H_0 : the two populations have the same distribution, against the alternative hypothesis H_1 : the distributions of the two populations are different. A lower p-value indicates H_1 to be true or in other words that the two samples have different distributions.

Apart from the above comparative studies, we explore the SMBH properties to understand how several aspects like mass ($M_{\rm BH}$), spin, Eddington ratio $\lambda_{\rm Edd}$, and jet kinetic power $Q_{\rm Jet}$ are related. Lastly, we discuss the environmental properties of GRGs which are found in clusters of galaxies (BCGs), and explore their relationship with the M_{200} and other BCG-RGs.

5.1. Comparison of Properties of GRGs and GRQs

As mentioned earlier, in this paper, only GRGs with z<1 are considered for analysis. But the redshift distribution of GRGs and GRQs is not similar as GRQs extend to higher redshifts as compared to GRGs. The mean and median redshifts of GRGs are 0.331 and 0.284 respectively for the range of 0.016 to 0.910, and for GRQs, the values are 0.515 and 0.475 respectively for the range of 0.085 to 0.999. Owing to the smaller number statistics of GRGs and especially GRQs, we have considered all the objects below redshift of 1 and not divided them further into sub-redshift bins. The distribution of redshift is shown in Fig. 5.

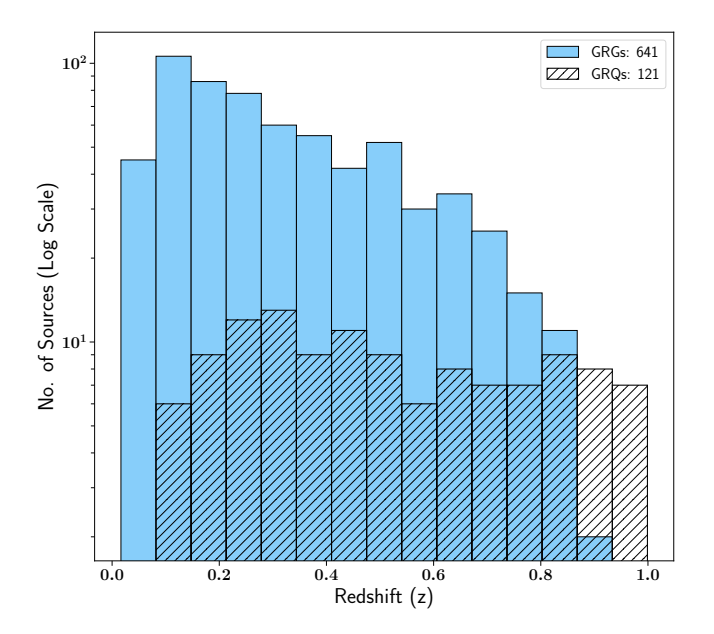


Fig. 5: Distribution of redshift (z) of GRGs and GRQs represented in unhatched and hatched bins respectively.

5.1.1. Distribution of Linear Size

The frequency of occurrence of sources in several bins of size is shown in Fig. 6 (a). The K-S test results in the p-value of 7.01×10^{-3} , which implies that the distributions of the samples are not the same. The sizes of GRGs is smaller than GRQs as shown in Table. 3, though the difference is not significant.

It is possible that the GRG-catalogue is subjected to some selection biases, as these have been taken from multiple and heterogeneous sources. However, if we consider the homogeneous sample of LoTSS and SGS, the median values of sizes for GRGs is 0.89 and 1.06 Mpc, and for GRQs 0.88 and 1.07 Mpc respectively. The mean values of sizes for GRGs and GRQs too are more or less similar in each sample. Therefore, our data suggest that sizes of GRQs are not significantly smaller than that of GRGs and are, in fact, quite similar.

5.1.2. Distribution of Radio Power (P_{1400})

Based on the availability of data from the NVSS, we were able to estimate P_{1400} for 722 GRGs from the GRG-catalogue. The distribution of P_{1400} of GRGs and GRQs is shown in Fig. 6 (b), where we observe that GRQs have higher radio power than GRGs at 1400 MHz. This is well supported by the K-S test with its p-value of 1.23 \times 10⁻¹⁶ strongly indicating that the two distributions are significantly different. Clearly, prevailing conditions in the central-engine of GRQs are able to produce more powerful jets resulting in more radio luminous sources as compared to GRGs. Knowing what these conditions require detailed study of their AGNs, but indeed GRQs are found to have higher jet kinetic power compared to GRGs (as shown below) and possibly they may host more massive black holes accreting at higher Eddington rate. Since our sample is restricted to sources with redshift less than 1, we do not observe more powerful GRQs, which are mostly at higher redshifts.

5.1.3. Distribution of jet kinetic power (Q_{Jet})

The Q_{Jet} of the GRGs and GRQs was estimated using TGSS and the LoTSS as explained in Sec. 3.3. Fig. 6 (c) shows the histogram of Q_{Jet} of GRGs and GRQs, where it is evident that the GRQs have the higher values of Q_{Jet} . The K-S test gives in p-value of 2.98×10^{-5} , which rejects the null hypothesis that they belong to the populations with identical distribution. From the inverse correlation between jet power and dynamical age, i.e. $Q_{\rm Jet} \propto 1/t_{\rm age}^{-2}$ (Ito et al. 2008), it can be inferred that if their linear sizes are similar, more powerful radio jets of the GRQs would take less time in scaling Mpc distance as compared to the GRGs (if placed in similar ambient density environment, which is not clear at this stage). Using a sample of 14 GRGs, Ursini et al. (2018) also, finds Q_{Jet} of GRGs to be in the range of $\sim 10^{42}$ erg s⁻¹ to 10^{44} erg s⁻¹. It has been observed (Mingo et al. 2014) that some RGs have much higher Q_{Jet} as compared to GRGs, which could be attributed to the severity of the radiative losses suffered by the GRGs over a period of their growth.

Ursini et al. (2018), based on their figure 3, hypothesised that GRGs like RGs at the start of their life have high nuclear luminosities as well as high $Q_{\rm Jet},$ which eventually fades over a period of time. Also, since their sample of GRGs is hard X-ray selected, it shows high nuclear luminosities, and other GRG samples (like our GRG-catalogue sample) which are radio selected will occupy the lower luminosity part of Ursini et al. (2018) figure 3. Our findings based on the GRG-catalogue support their hypothesis, as we mostly have radio-selected GRGs with $L_{\rm bol}$ in the range of $\sim 10^{42}$ erg s $^{-1}$ to 10^{46} erg s $^{-1}$, which is below the $L_{\rm bol}$ range of Ursini et al. (2018) hard X-ray selected sample of 14 GRGs.

5.1.4. Distribution of Spectral Index (α_{150}^{1400})

Fig. 6 (d) shows the histogram of the spectral indices of 252 GRGs and 37 GRQs. Similar criterion (as mentioned in Sec. 3.4 and Sec. 4.2) of considering only those sources which have full detection in TGSS (or LoTSS) and NVSS was followed for the sources in the GRG-catalogue. For this study only sources from LoTSS and SGS were used. The median and mean values of the spectral index of GRGs are 0.73 and 0.75, and GRQs have median and mean spectral index as 0.72 and 0.72 respectively. This result is also consistent with the recent findings of Dabhade et al. (2020). The K-S test with p-value of 0.12, further confirms that both the GRGs and GRQs have the same distribution of spectral index with 95% level of significance.

5.2. Comparison of Properties of HEGRGs and LEGRGs

Based on the stringent criteria mentioned in Sec. 3.9, here we classify GRGs into high and low excitation or HEGRGs and LEGRGs types. If we consider their respective RG counterparts called the LERGs and HERGs, the LERGs are the dominant population as compared to HERGs. About 12% of the sample of Kozieł-Wierzbowska & Stasińska (2011) comprises of HERGs, and almost similar is the case for Best & Heckman (2012). As mentioned previously in Sec. 3.9, in order to have a clean sample, we do not consider LERGs or LEGRGs from region-III as they are contaminated with possible star formation. Therefore, our LEGRG

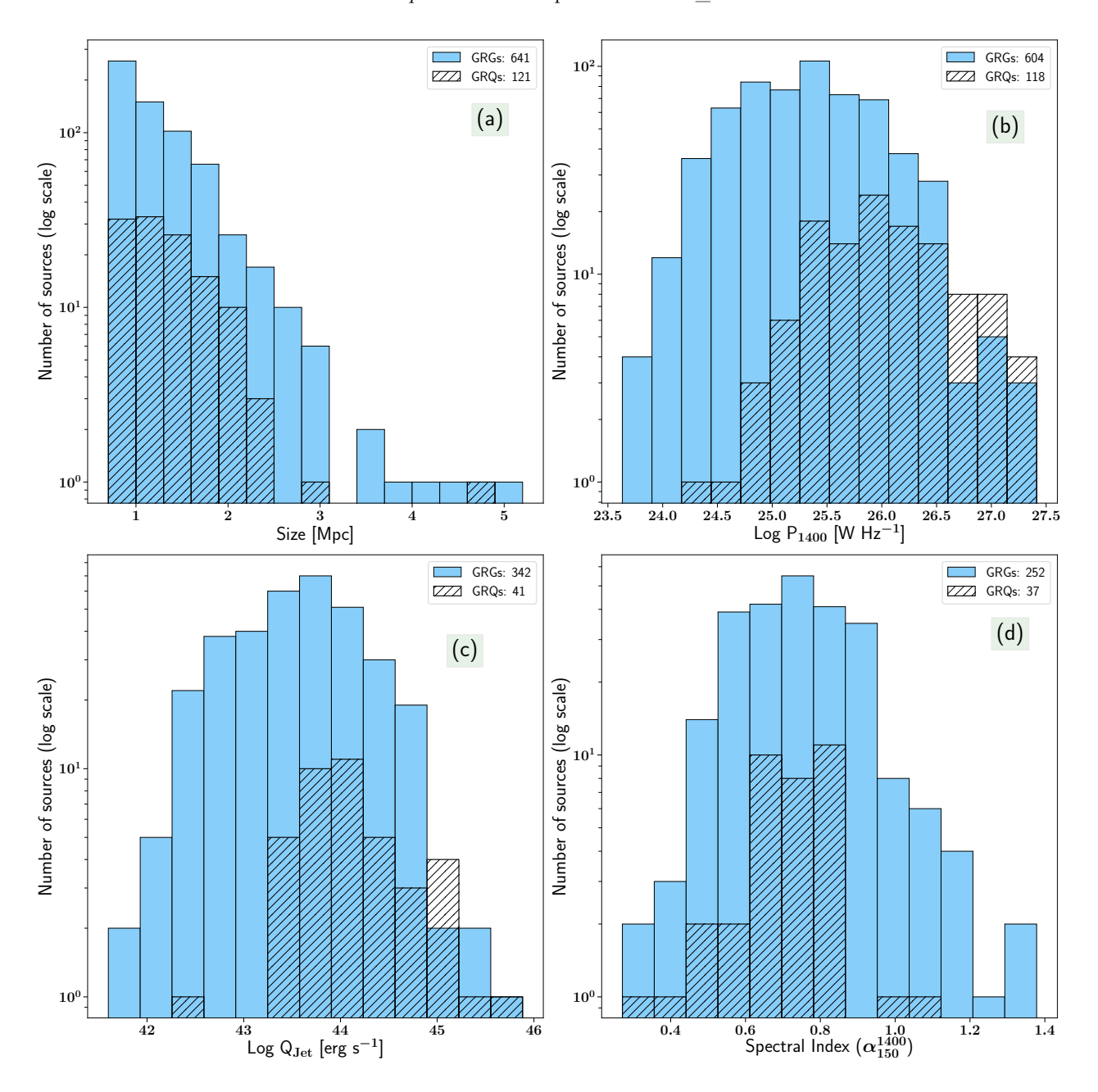


Fig. 6: The above plots show distribution of GRGs and GRQs for their different properties, where they are represented in unhatched and hatched bins respectively in the redshift range of 0.01 < z < 1.0. The mean and median values of the distributions are given in Table. 3. Sub-figure a: distribution of size; Sub-figure b: histogram of radio power at 1400 MHz (P₁₄₀₀); Sub-figure c: distribution of jet kinetic power (Q_{Jet}); sub-figure d: histogram of spectral index (α_{150}^{1400}).

sample reduces drastically to 153, since we only consider sources from region-II to be LEGRGs. The HEGRGs from the region-I sum upto a total of 148 sources and therefore makes our comparison samples almost equal with each other.

In the following subsections, we have individually described the distribution of HEGRGs and LEGRGs in terms of various properties. As seen in Fig. 7, for each property, the number of sources vary as it is dependent on the availability of data from public archives as the SDSS, NED and Vizier etc.

5.2.1. Distribution of Linear Size

The size distributions of 153 LEGRGs and 148 HEGRGs from the GRG-catalogue are shown in the Fig. 7 (a) based on the availability of data and classification. Both the classes seem to follow different distributions as indicated by p-value of 4.20×10^{-11} of K-S test. Our data suggest that HEGRGs tend to grow to larger sizes than the LEGRGs as seen from their mean and median values of sizes presented in Table. 3. In other words, the radiatively efficient nature of HEGRGs helps in the growth of GRGs to larger sizes.

Similarly, if we take a sample of RGs (~ 400 RGs; Kozieł-Wierzbowska & Stasińska 2011) for which we have size estimates along with high and low excitation classifi-

cation (from WISE), we find the similar result that sizes of high excitation (HERGs) sources are larger than those of low excitation sources (LERGs). Therefore, it is evident that this particular property is similar for RGs and GRGs and is independent of the overall size of the source.

5.2.2. Distribution of Radio Power (P_{1400})

Fig. 7 (b) shows P_{1400} distribution of 139 LEGRGs and 136 HEGRGs, from which we infer that, firstly, the HEGRGs spread over a larger range of P_{1400} in comparison with LEGRGs. Secondly, the distributions are fairly different as strongly indicated by p-value of 2.56×10^{-24} of K-S test. There is a significant overlap in their distributions also, with HEGRGs having higher P_{1400} than LEGRGs as seen in Table. 3. This result complements the fact that HEGRGs have high accretion state, resulting in the high radio power of GRGs. Kozieł-Wierzbowska & Stasińska (2011) too found that HERGs like HEGRGs, which are radiatively efficient have higher radio power at 1400 MHz.

5.2.3. Distribution of jet kinetic power (Q_{Jet})

The $Q_{\rm Jet}$ of both the population varies over a wide range with HEGRGs occupying the higher end of the distribution (Fig. 7 (c)). The difference in $Q_{\rm Jet}$ is statistically significant with median $Q_{\rm Jet} \sim 10^{44} {\rm erg s^{-1}}$ of HEGRGs being around 10 times higher than that of LEGRGs (Table. 3). The high mean and median values of HEGRGs (as seen in Table. 3) as compared to LEGRGs strongly indicate that the AGNs of GRGs with high excitation type is responsible for launching higher powered jets, resulting in more radio luminous sources (higher P_{1400} as above).

5.2.4. Distribution of Absolute r-band Magnitude (M_r)

The estimated M_r of 83 LEGRGs and 47 HEGRGs is presented in Fig. 7 (d), which show two distinct populations, and is also supported by the low p-value of K-S test (Table. 3). The LEGRGs are found to be optically brighter by ~ 1 magnitude than HEGRGs, indicating that LEGRGs are mostly hosted by bright giant elliptical galaxies comprising of old stellar population which is quite prominent from their absolute r-band magnitudes. This is consistent with the findings of Hardcastle et al. (2007) who have shown this for LERGs.

Overall, Fig. 7 (d) shows M_r distribution of GRGs ranging from ~ -19 to -25 in brightness. A similar distribution has been observed for host galaxies of normal sized RGs (Govoni et al. 2000; Sadler et al. 2007; Capetti et al. 2017).

5.2.5. Distribution of Black Hole Mass (M_{BH})

A study of M_{BH} distribution in LEGRGs and HEGRGs is very crucial in understanding one of the key factors driving the two different accretion modes. For this study, our sample was restricted to 94 sources based on the availability of the spectroscopic data from SDSS. Fig. 7 (e) shows the distribution of M_{BH} of both the classes, in which mean and median (see Table. 3) of LEGRGs are found to be greater than HEGRGs. The difference in mean and median values as well as the p-value of 2.24×10^{-4} in K-S test, proves

that both the distributions are different or in other words HEGRGs have lower $M_{\rm BH}$ when compared to LEGRGs.

5.2.6. Distribution of Eddington ratio ($\lambda_{\rm Edd}$)

In this study, the sample is restricted to just 55, due to the availability of reliable [OIII] line flux data from the SDSS, which is essential for estimating the L_{bol} . Out of this a total of 48 GRGs are classified as LEGRG, and 7 are classified as HEGRG in the GRG-catalogue depending on their mid-IR properties. Nearly 87% of the sample constitutes LEGRGs which is consistent with earlier studies (Hardcastle 2018a), where it is shown that LERGs are the dominant population of radio galaxies. LERGs or LEGRGs are dominated by the 'Radiatively Inefficient Accretion Flow' or RIAF (Yuan & Narayan 2014). In Fig. 7 (f) we observe the distribution of $\lambda_{\rm Edd}$ which ranges from $\sim 10^{-4}$ to 10^{-2} for LEGRGs and from 10^{-2} to 10^{-1} for HEGRGs with a little overlap. The lower $\lambda_{\rm Edd}$ values of (Table. 3) of LEGRGs, implies a radiatively inefficient state governed by low accretion rate. HEGRGs, in contrast to LEGRGs, are rarer and have comparatively higher $\lambda_{\rm Edd}$ (Table. 3), indicating their radiatively efficient mode and higher accretion rate. Our results on GRGs are similar to previous findings on RGs by Kozieł-Wierzbowska & Stasińska (2011); Smolčić (2009); Best & Heckman (2012), who have shown that $\lambda_{\rm Edd}$ is higher for HERGs as compared to LERGs. The λ_{Edd} of LEGRGs peaks around 10^{-4} , which is consistent with the findings presented in Ho (2008).

5.2.7. HEGRG-LEGRG comparison overview

In the earlier 6 subsections while comparing HEGRGS to LEGRGs we have found that LEGRGs to be optically brighter by ~ 1 magnitude than HEGRGs and have lower Eddington ratios but higher black hole masses and launch lower Q_{Jet} jets (by factor 10), also implies that higher mass BHs are growing in the nucleus of optically brighter and more massive galaxies, whose central engines are presently found in low excitation, radiatively inefficient, low mass accretion state but are capable of producing sufficiently powerful FR-II jets resulting in Mpc-scale GRGs, which clearly constitute the vast majority (> 80%) of all GRGs selected in our study. Beyond the scope of the present work, in future, it will be very effective if one compares the detailed properties of LERGs with LEGRGs and HERGs with HEGRGs in order to gain much deeper insight into the inner workings of GRG central engine.

5.3. How similar are GRGs and RGs?

The following studies have been carried out to understand the factors which make a very small population of RGs transform into GRGs. We carry out this investigation by studying three of their properties - α , M_{BH} and λ_{Edd} , in this Section. Possible differences in black hole spin are discussed in Sec. 5.4.1

5.3.1. Spectral Index (α)

Several radio spectral index studies of RGs in the past (Kellermann et al. 1969; Oort et al. 1988; Gruppioni et al. 1997; Kapahi et al. 1998; Sirothia et al. 2009; Ishwara-

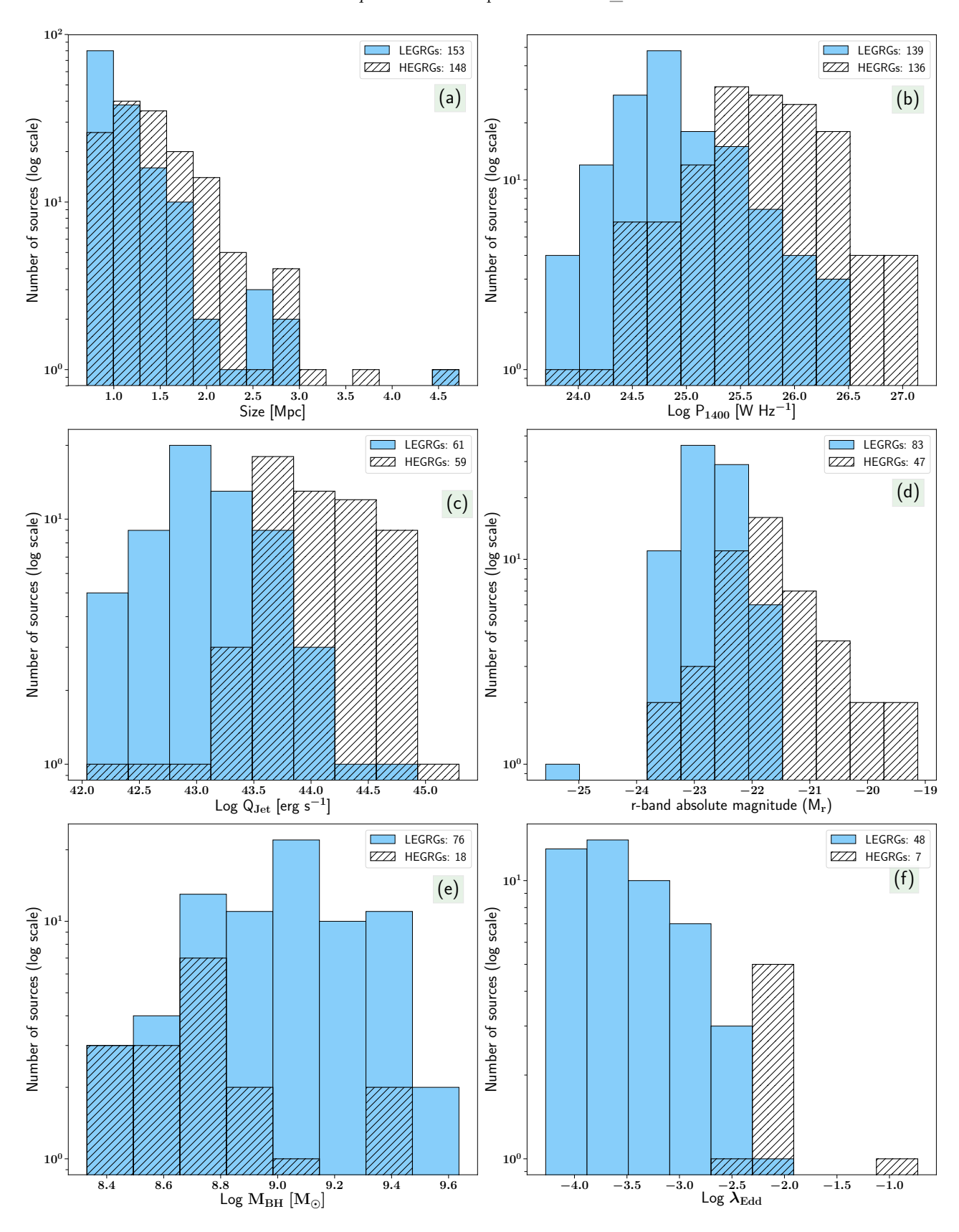


Fig. 7: The above plots show distribution of LEGRGs and HEGRGs for their various physical properties, where they are represented in unhatched and hatched bins respectively in the redshift range of 0.01 < z < 1.0. The mean and median values of the distributions are given in Table. 3. Sub-figure a: distribution of physical size (Mpc); Sub-figure b: histogram of radio power at 1400 MHz (P₁₄₀₀); Sub-figure c: distribution of jet kinetic power (Q_{Jet}); Sub-figure d: histogram of absolute r-band magnitude (M_r); Sub-figure e: histogram of black hole mass (M_{BH}); Sub-figure f: distribution of Eddington ratio ($\lambda_{\rm Edd}$); here accretion state of GRGs with $\lambda_{\rm Edd} \leq 10^{-2}$ is shifted towards the Radiatively Inefficient Accretion Flows or RIAFs regime.

Chandra et al. 2010; Mahony et al. 2016) have established the mean spectral index value to be ~ 0.75 . Until recently, it was believed that GRGs have steeper spectral index values. However, Dabhade et al. (2020), using their large sample of GRGs found that the spectral index of RGs and GRGs is very similar. Now, with our GRG-catalogue (which comprises of LoTSS and SGS), we establish this result strongly with larger (> 250) sample size as seen in Table. 3, where we have shown the α for GRGs and GRQs to be ~ 0.75 and ~ 0.72 respectively.

5.3.2. Black Hole Mass (M_{BH})

- 1. RG Sample In order to compare $M_{\rm BH}$ of GRGs and RGs, we use the RG sample from Best & Heckman (2012). This RG sample was created using the SDSS DR7 (Abazajian et al. 2009) optical spectroscopic data along with the FIRST and NVSS radio data. This sample has been filtered from star-forming galaxies (SFGs) and only consists of radio-loud AGNs (RLAGNs) or RGs. Further, we fetched their stellar velocity dispersion (σ) information to compute M_{BH} from SDSS DR14 database (Abolfathi et al. 2018) through CasJobs⁵, and retained only those galaxies which had reliable spectra, i.e., redshift warning flag, ZWarning = 0 from the SDSSDR14 database. Next, only sources with σ in the range of $80 < \sigma < 420 \; \mathrm{km} \; s^{-1}$ were selected based on the criterion provided by Bolton et al. (2012). Lastly, in order to have a more clean and robust sample, we also imposed an additional filter to the sources in the sample to have σ error less than 30%. The redshift range of RG sample was restricted in the range of 0.01 to 1 to match the redshift range of the GRG sample (GRG-catalogue), and radio-loud quasars were not considered for this study. Therefore, this reduced the original RG sample of Best & Heckman (2012) to 14764. We will call this edited sample as BH12 in the rest of the paper.
- 2. The GRG Sample In our SGS, only 46 GRGs have spectroscopic data from the SDSS, and hence, only these have $\rm M_{BH}$ estimates derived from the $\rm M_{BH}\text{-}\sigma$ relation. In order to carry out a comparative study of $\rm M_{BH}$ which is statistically significant, we make use of the GRG-catalogue. Out of 820 GRGs in the GRG-catalogue (including SGS), 230 have clean, reliable σ information from the SDSS and hence, for the purpose of $\rm M_{BH}$ RG-GRG comparison study our sample of GRGs is restricted to 230.
- 3. Distribution of Black Hole Mass As seen in Fig. 8 (a), the distributions of RGs and GRGs are largely similar. The spread of RGs is wider on the lower end of the plot as compared to GRGs, but both the distributions peak at the similar value and have similar mean and median values (GRG: mean = $1.06 \times 10^9 \, \mathrm{M_\odot}$, median = $0.79 \times 10^9 \, \mathrm{M_\odot}$; RG: mean = $1.10 \times 10^9 \, \mathrm{M_\odot}$, median = $0.84 \times 10^9 \, \mathrm{M_\odot}$). This establishes that both RGs and GRGs have same M_{BH} distribution, and it is also supported by the K-S test where the p-value of 0.60 emphasises that null hypothesis cannot be rejected, and the distributions of the two samples are the same.

5.3.3. Eddington ratio ($\lambda_{\rm Edd}$)

As per the availability of [OIII] line flux information from the SDSS, we have the estimation of $\lambda_{\rm Edd}$ for 99 GRGs from the GRG-catalogue and 14366 RGs from BH12, whose distribution is shown in Fig. 8 (b). Based on our analysis of the available data, it appears that the RGs and GRGs have different mean and median values (Table. 3). The plot shows that the distributions are different, which is statistically evident from the p-value of 5.71 \times 10 $^{-16}$ from K-S test. Thus, our data indicates $\lambda_{\rm Edd}$ of RGs to be higher than that of GRGs. We can further extrapolate and conjecture that GRGs mostly have RIAF as compared to RGs as almost all the GRGs have $\lambda_{\rm Edd} < 0.01$ (which is the RIAF regime).

5.4. Astrophysical processes near accreting black holes in GRGs

5.4.1. Black Hole Spin (a)

The spin of the accreting black hole has been identified as one of the key ingredients for powering the relativistic jets in AGN for a timescale of millions of years or more. Rearranging equation 7, we get

$$a \propto \frac{\sqrt{\rm Q_{Jet}}}{\rm B \times M_{BH}}$$
 (9)

The spin (a) of the black hole of GRGs has been estimated using our M_{BH} and Q_{jet} estimates as explained in Sec. 3.8. We rejected sources with 60% and above error in their M_{BH} estimates and therefore, our sample (GRG-catalogue) was restricted to 95 sources for this particular study as listed in Table A.3. Fig. 9 shows the distribution of black hole spin with respect to M_{BH} varying over two orders of magnitude i.e 10^7 to 10^9 M_{\odot}. The range of spin spans from 0.007 to 0.518 resulting in the mean and median values of 0.079 and 0.055 respectively for GRGs in our sample. We also plot iso-tracks with their respective colours which indicate the constant jet kinetic powers obtained for various range of spin, M_{BH} and magnetic field strength. The magnetic field is assumed to be a dynamically important field near the black hole (given by Eq. 8), since it has been observationally shown to exist (Eatough et al. 2013).

King & Pringle (2006) find that if a black hole has a series of accretion episodes whose principal angular momentum vectors are randomly orientated (a chaotic randomwalk process), with black hole's angular momentum domination, then it leads to lower black hole spin values. However, the successive accretion flows accumulate the poloidal magnetic flux in the vicinity of the black hole, and this strong magnetic flux threading the black hole accretion disk might lead to the state of a magnetically arrested disk (MAD), which affects the dynamical accretion process onto the black hole itself (Narayan et al. 2003; Tchekhovskoy et al. 2011). This state disrupts the accretion flow by breaking the flow into small streams. The velocity of the stream decreases with respect to free-fall velocity as the material in the stream has to find its way to the black hole through magnetic interchange and re-connection, which results in lower spin values of the black hole. Similarly, the low spin value of GRGs is explainable if we invoke the state of MAD or equivalently a dynamically important field, which indicates that their accretion history was chaotic rather than a smooth, progressive process. An outwardly decreasing angular velocity of the disk gives rise to linear instabilities in

⁵ http://skyserver.sdss.org/CasJobs/

Table 3: Mean and median values of properties of sources in the GRG-catalogue for comparison between their sub-types like GRG-GRQ, HEGRG-LEGRG and GRG-RG. The p-value corresponds to K-S test of the respective distributions. Only the sources below redshift of 1 were considered from the GRG-catalogue for all the studies.

Property	No of sources	Mean	Median	No of sources	Mean	Median	p-value
		GRG			GRQ		
Size [Mpc]	641	1.26	1.09	121	1.35	1.23	7.01×10^{-3}
$P_{1400} [W Hz^{-1}]$	604	8.53×10^{25}	2.09×10^{25}	118	26.22×10^{25}	9.09×10^{25}	1.23×10^{-16}
$Q_{Jet} [erg s^{-1}]$	342	13.23×10^{43}	4.03×10^{43}	41	37.85×10^{43}	12.30×10^{43}	2.98×10^{-5}
α_{150}^{1400}	252	0.75	0.73	37	0.72	0.72	1.20×10^{-1}
		HEGRG			LEGRG		
Size [Mpc]	148	1.45	1.35	153	1.12	0.97	4.20×10^{-11}
$P_{1400} [W Hz^{-1}]$	136	11.29×10^{25}	4.94×10^{25}	139	1.68×10^{25}	0.65×10^{25}	2.56×10^{-24}
$Q_{Jet} [erg s^{-1}]$	59	20.66×10^{43}	10.20×10^{43}	61	2.70×10^{43}	0.95×10^{43}	3.71×10^{-15}
$ m M_r$	47	-21.67	-21.84	83	-22.75	-22.76	1.20×10^{-11}
${ m M_{BH}~[M_{\odot}]}$	18	0.72×10^{9}	0.52×10^9	76	1.26×10^{9}	1.11×10^{9}	2.24×10^{-4}
$\lambda_{ m Edd}$	7	3.25×10^{-2}	8.15×10^{-3}	48	6.75×10^{-4}	2.86×10^{-4}	5.72×10^{-6}
		GRG			RG		
${ m M}_{ m BH} \ [{ m M}_{\odot}]$	230	1.06×10^{9}	0.79×10^{9}	14764	1.10×10^{9}	0.84×10^{9}	6.07×10^{-1}
$\lambda_{ m Edd}$	99	4.05×10^{-3}	5.41×10^{-4}	14366	7.50×10^{-3}	2.93×10^{-3}	5.71×10^{-16}

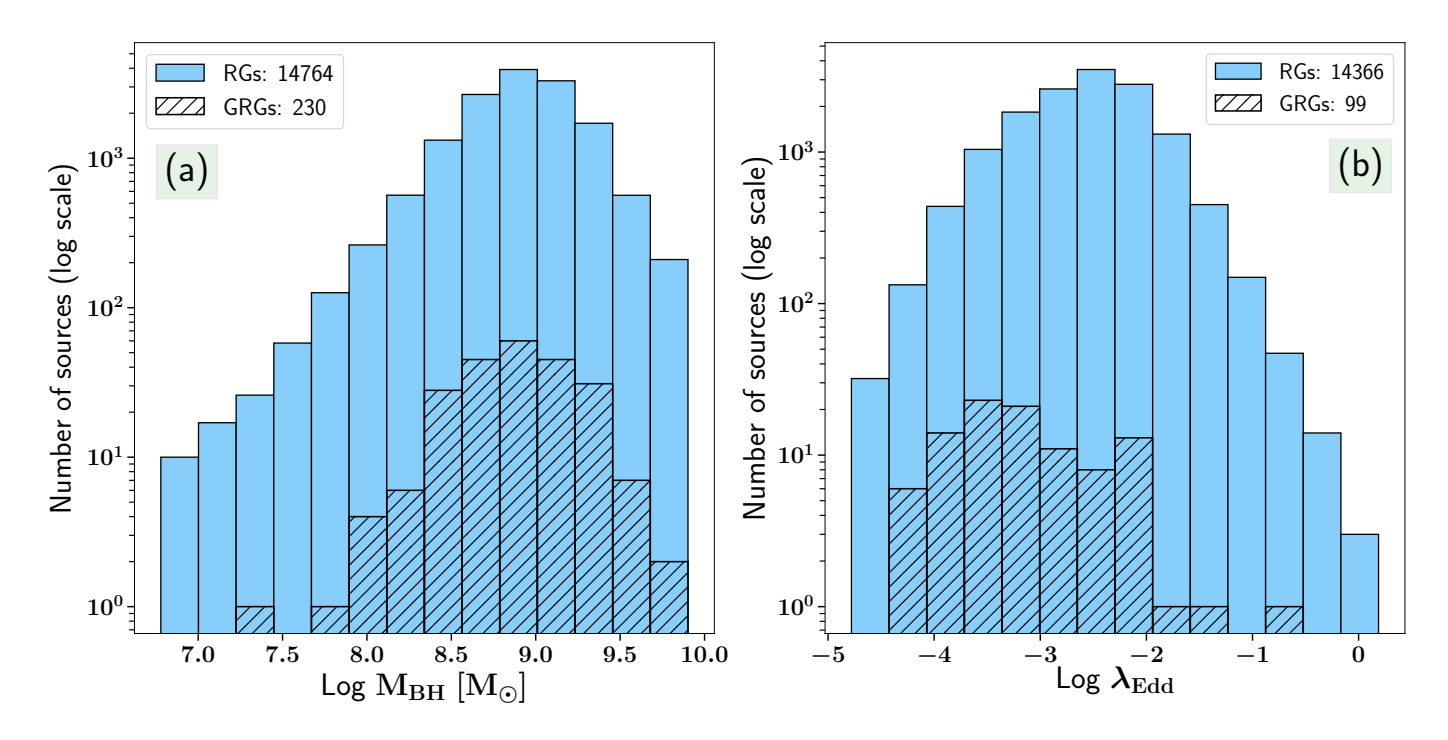


Fig. 8: Distribution of black hole mass (M_{BH}) in sub-figure (a) and Eddington ratio (λ_{Edd}) in sub-figure (b) of RGs (unhatched bins) and GRGs (hatched bins). The RG sample has been derived from Best & Heckman (2012) and the GRG sample is from the GRG-catalogue created by us.

the magnetised fluid, namely magneto-rotational instabilities (MRI) (Balbus & Hawley 1998) which in turn generate magneto-hydrodynamic turbulence in the disk. This effectively enhances the viscosity of small streams of fluid. Thus the in-falling material has to pave its way through streams of velocity gradients via magnetic reconnection which periodically randomises the direction of angular momentum.

Hence, even for smaller scales, the angular momentum of the central black hole was misaligned with respect to the accreted material eventually resulting in the spin-down of the black hole. Nevertheless, these small regions of viscosity raise the overall viscosity of the disk and eventually, strengthen the magnetic field of the disk which has a significant impact in powering relativistic jets.

Another possible scenario could be due to the self gravity which fragments the material in the disk into small clouds with randomly oriented angular momentum (Fanidakis et al. 2011). This leads to randomly oriented numerous accretion episodes which collectively lower the spin of the black hole. The lower spin correlating with higher mass black holes (Fig. 9) suggests that SMBHs powering the GRGs were formed due to episodes of quasi-isotropic, chaotic accretion events.

In addition, Fig. 9 also shows distribution of spin as a function of black hole mass in various bins of $Q_{\rm Jet}$ from $10^{41}~{\rm erg~s^{-1}}$ to $10^{45}~{\rm erg~s^{-1}}$, which we have simulated using equations 7 and 8. It can be well observed that with the plausible values of black hole mass, magnetic field and spin, no GRG is observed to acquire a $Q_{\rm Jet} \geq 10^{45}~{\rm erg~s^{-1}}$. For the objects with a low value of $Q_{\rm Jet}~(\sim 10^{41}~{\rm erg~s^{-1}})$, even a drastic change in the magnetic field or $M_{\rm BH}$ would lead to only a minute change in spin, whereas for the objects with higher $Q_{\rm Jet}$ ($\sim 10^{44}$ erg s⁻¹) values, a small change in the magnetic field or $M_{\rm BH}$ would result into a significant change in spin values. Based on our sample, we observe that the spin values of 99% of GRGs are constrained within 0.3. For the source having the highest spin value of 0.518, a right combination of lower mass and high jet power as compared to the rest of the sources served as the favourable condition. AGNs of both types, i.e. with and without powerful jets have SMBHs which are spinning rapidly, which in turns implies that spin alone is not the driving factor for the production of powerful relativistic jets. Spin is coupled with the strength and geometry of the magnetic field, which depends on the accretion rate (Abramowicz & Fragile 2013). A further study is needed with a larger sample of GRGs and a comparison study with the RGs to understand this interplay of various properties driving the GRGs to megaparsec

5.4.2. Disk-Jet Coupling: The interplay between Eddington ratio ($\lambda_{\rm Edd}$), spin (a), and jet kinetic power ($Q_{\rm Jet}$)

What is the role of black hole spin as well as its accretion rate in the launching of observed radio jets is still a highly contentious, but an unsolved issue (Reynolds 2019). Most often the jet radio luminosity is taken as a good indicator of the the jet kinetic power, but in reality it is only a small fraction of the latter. What then is the source of radio jet power that we observe in black hole systems which fuels the extremely large GRGs, and how does its luminosity scales with the black hole spin and accretion rate?

The growth and evolution of AGN is coupled with accretion rate and spin of the central black hole which determines the accretion radiative efficiency (ϵ) i.e. what fraction of rest mass energy of accreted matter in the accretion disk is getting converted into radiation ($L_{\rm bol} = \epsilon \dot{\rm M} c^2$) (Novikov & Thorne 1973; Thorne 1974). The spin of the black hole dictates the position of the innermost stable circular orbit (ISCO), which is the innermost edge of the accretion disk (Bardeen et al. 1972). For a black hole with retrograde spin i.e. $-1 \le a < 0$, $9R_{\rm g} \le r_{\rm ISCO} < 6R_{\rm g}$ whereas for prograde spin i.e., $0 < a \le 1$, $6R_{\rm g} < r_{\rm ISCO} \le R_{\rm g}$, where $R_{\rm g}$ is gravitational radius of black hole and is expressed as $R_{\rm g} = GM_{\rm BH}/c^2$. The higher spin of the black hole brings the ISCO closer to the black hole and therefore, increases the radiative efficiency of the accretion flow. This is quite evi-

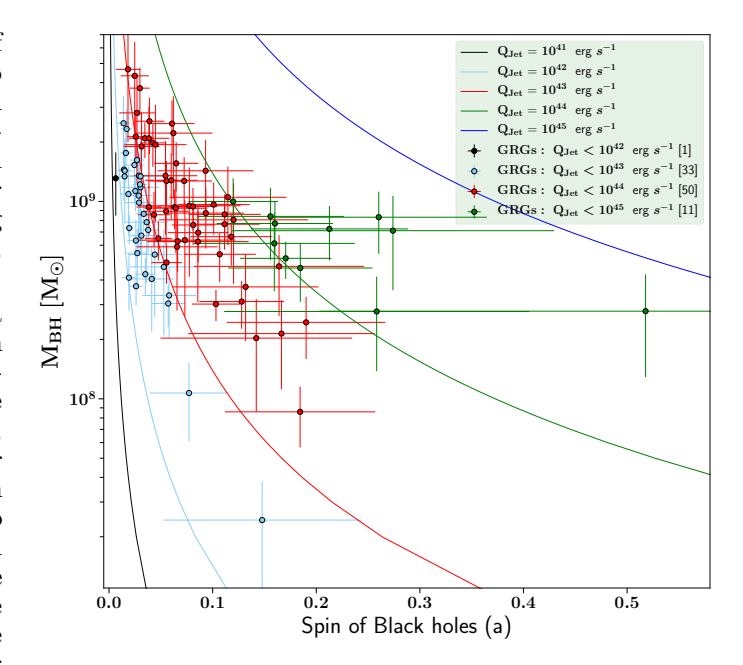


Fig. 9: The figure shows a simulation of black hole spin (using Eq. 9) as a function black hole mass over a various range of jet kinetic power with coloured points representing estimated values from observation of GRGs. The solid curved lines with their respective colours indicate the different values of spin a black hole could attain for a mass range of $10^7 \, \mathrm{M}_\odot$ to $10^9 \, \mathrm{M}_\odot$ at that particular jet kinetic power. The solid circles with different colours indicate the GRGs in our sample with their estimated spin values lying in the range of jet kinetic power specified. The total number of GRGs is 95. Figures mentioned in the square brackets in the legend of the plot indicate number of GRGs in respective kinetic jet power bins.

dent from the following relation:

$$\epsilon = 1 - \sqrt{1 - \frac{2}{3} \frac{1}{\hat{\mathbf{r}}_{\text{ISCO}}}} \tag{10}$$

where ϵ is the accretion radiative efficiency and \hat{r}_{ISCO} = r_{ISCO}/R_g. In order to compare the spins of RGs and GRGs, we have used FR-II RG sample of 105 sources with z < 1from Daly (2011) and Daly (2019). We observe that nearly 66% of the RG sample have black hole spins greater than 0.3, which is quite larger than the lower spins of GRGs in our GRG-catalogue (see Fig. 9 & Sec. 5.4.1). The available spin estimates enabled us to estimate $r_{\rm ISCO}$ for the combined sample of RGs (Daly 2011, 2019). The r_{ISCO} has been computed using equation 2.21 of Bardeen et al. (1972), which was further used to estimate the ϵ using Eq. 10. It results in the mean ϵ of RGs to be $\sim 15\%$, and for GRGs the mean ϵ comes to $\epsilon \sim 6\%$. Hence, RGs appear to be more efficient as compared to GRGs based on the above mentioned theoretical assumptions and our observational data. Previous studies (Marconi et al. 2004; Zhang et al. 2012; Ueda et al. 2014) on AGN in general have shown the accretion efficiency to be $\epsilon \sim 10\%$. If we consider an extreme scenario of a prograde maximally spinning black hole (a=1)

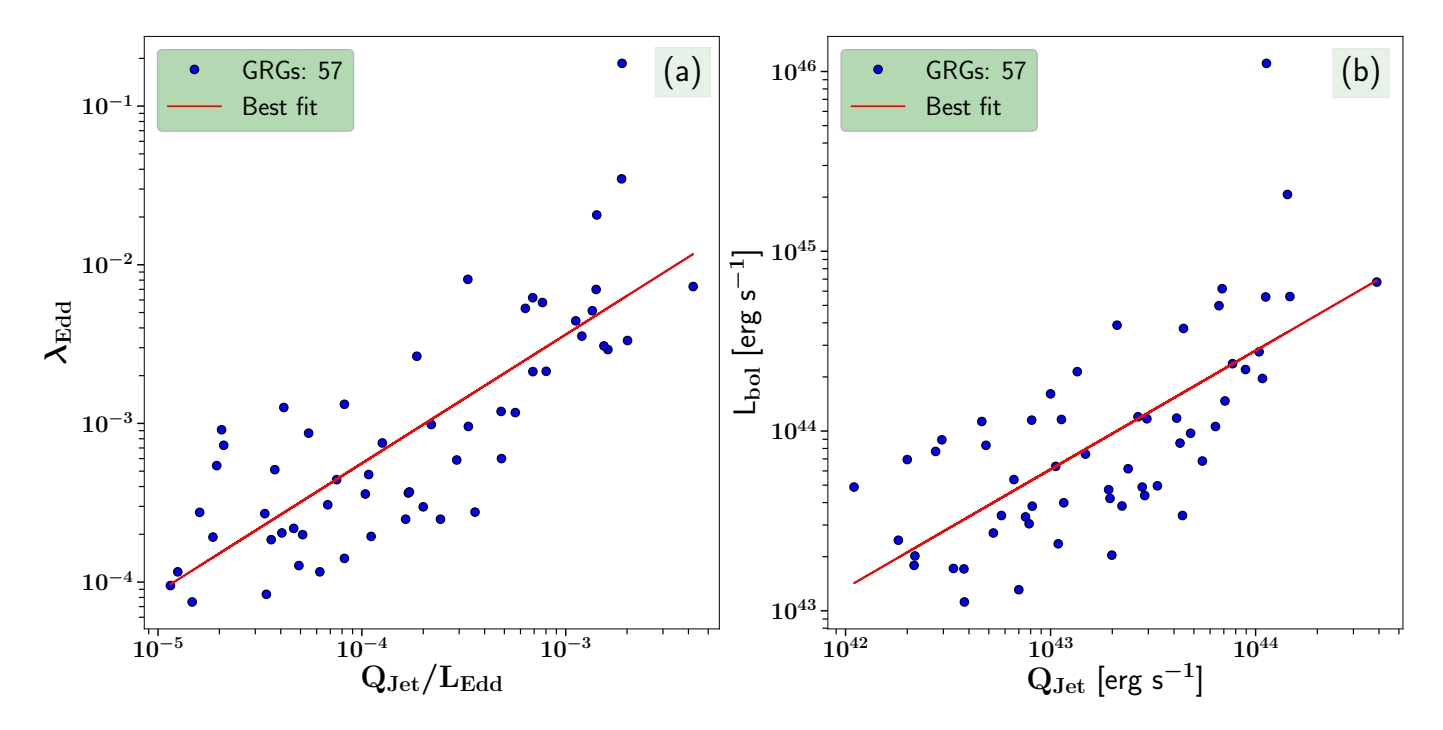


Fig. 10: As discussed in Sec. 5.4.2, the sub-figure (a) shows a linear correlation for 57 objects between Eddington ratio ($\lambda_{\rm Edd}$) and the ratio of jet kinetic power (Q_{Jet}) to the Eddington luminosity (L_{Edd}), which can be represented as: $\log \lambda_{\rm Edd} = 0.81 \times \log(Q_{\rm Jet}/L_{\rm Edd}) - 0.005$; sub-figure (b) shows bolometric luminosity (L_{bol}) as a function of jet kinetic power (Q_{Jet}), which takes the equation form as: $\log L_{\rm bol} = 0.66 \times \log(Q_{\rm Jet}) + 15.38$; The Spearman's correlation coefficient is 0.8 and 0.7 for sub-figure (a) and sub-figure (b) respectively. The red line indicates the best linear fit of the correlations on the log-log plots.

then the $\epsilon \sim 42\%$. The accretion radiative efficiency (ϵ) is related to the Eddington ratio, which can be expressed as:

$$\frac{\epsilon \dot{M}c^2}{\dot{M}_{\rm Edd}c^2} = \frac{L_{\rm bol}}{L_{\rm Edd}} = \lambda_{\rm Edd} \tag{11}$$

In order to understand the possible co-dependence of various parameters of black holes for the purpose of jet launching and propagation, we have studied how $\lambda_{\rm Edd}$ affects the $Q_{\rm Jet}.$ Hence, we have created a sub-sample of 57 GRGs (based on their data availability) from the GRG-catalogue and find that there is linear correlation between the Eddington ratio $(\lambda_{\rm Edd})$ and $Q_{\rm Jet}/L_{\rm Edd}$ (dimensionless jet kinetic power), which is strongly supported by the Spearman correlation coefficient of 0.8 as seen in Fig. 10 (a). The relation between the two parameters takes the following form: $\log \lambda_{\rm Edd} = 0.81 \times \log(Q_{\rm Jet}/L_{\rm Edd}) - 0.005$ based on our data.

Therefore, it implies that $L_{\rm bol}$ has a significant influence on the collimated kinetic jet output $(Q_{\rm Jet})$ of the AGN since $\lambda_{\rm Edd} = \frac{L_{\rm bol}}{L_{\rm Edd}}$, and corresponding equation takes the form as : $\log L_{\rm bol} = 0.66 \times \log(Q_{\rm Jet}) + 15.38$ as evident from Fig. 10 (b). Spearman correlation coefficient for the above correlation is 0.7. The formation and propagation of highly relativistic magnetised jets is dependent (disk-jet coupling) on the magnetic field strength coupled to magnetic field geometry of the accretion disk (McKinney & Narayan 2007).

Zamaninasab et al. (2014) have shown that there exists a strong correlation between the jet magnetic field $\phi_{\rm Jet}$ and accretion disk luminosity (L_{acc} or L_{bol}). Further, they also concluded that the launching regions of jets are threaded

by dynamically important magnetic fields with the possible influence of the black hole's spin and strongly favouring the MAD model of the accretion disk. Similarly, Sikora & Begelman (2013) also argue in favour of magnetic flux threading of black hole over spin and Eddington ratio as the governing factor for the launch of collimated powerful radio jets. Zamaninasab et al. (2014) also find that the magnetic flux of black hole $\phi_{\rm BH} \propto \sqrt{L_{\rm bol}}$ $\rm M_{BH}$ and hence, in absence of direct measurements of $\phi_{\rm BH}$, we can use $\rm L_{bol}$ as proxy. Therefore, our $\rm L_{bol}$ - $\rm Q_{Jet}$ correlation (discussed above) is also indicative of strong influence of $\phi_{\rm BH}$ on $\rm Q_{Jet}$. This strongly hints at disk-jet coupling phenomenon where the magnetic field in the magnetically arrested disk surrounding the black hole controls the dynamics of accretion flow responsible for jet launching.

In ADAF, Q_{Jet} is related to L_{Edd} (Fanidakis et al. 2011):

$$Q_{\rm Jet} \sim 0.01 a^2 L_{\rm Edd} \tag{12}$$

where $Q_{\rm Jet}$ and $L_{\rm Edd}$ are in erg s⁻¹. It shows that maximum 1% of $L_{\rm Edd}$ can be converted into $Q_{\rm Jet}$ if we consider spin to be 1. Based on our analysis, we infer that $\sim 0.05\%$ of $L_{\rm Edd}$ on an average is getting converted into $Q_{\rm Jet}$ for GRGs. Therefore, it is evident from above result and discussion that for GRGs the fraction $L_{\rm Edd}$ converting to $Q_{\rm Jet}$ is quite low and hence, is expected to have lower spin values as well. This matches with our estimated spin values presented in Sec. 5.4.1, where the mean spin value is ~ 0.079 . The spin values for our GRGs have been estimated using independently computed $Q_{\rm Jet}$ and $M_{\rm BH}$ values. Here, the $Q_{\rm Jet}$ is the lower limit as the $Q_{\rm Jet}$ relation (Eq. 3) from

Hardcastle (2018b) is expected to underestimate the Q_{Jet} for GRGs and hence the spin values also are expected to be the lower limits. However, for GRGs, even after corrections in spin values, it will be much lower than spin values of RGs. From the correlations shown in Fig. 10 (a), one can expect a significant correlation between the spin and $\lambda_{\rm Edd}$ also, represented through the relation: $\log \lambda_{\rm Edd} = 1.62 \times$ $\log(a) - 1.02$ based on the same data. Spearman's correlation coefficient for the above is 0.8. The $\lambda_{\rm Edd}$ is an indicator of accretion efficiency onto the black hole, which increases with increasing value of spin. The spin regulates in through $r_{\rm ISCO}$ and in turn affects $\lambda_{\rm Edd}$ as seen from Eq. 10 and Eq. 11. Based on our results, we observe strong evidence of a tight correlation between spin and $\lambda_{\rm Edd}$ at least for the lower regime of spin and $\lambda_{\rm Edd}$ values. Fig. 9 clearly depicts that the value of spin decreases with the increase in black hole mass which is quite consistent with the findings of Daly (2011) and Griffin et al. (2019), but the magnitude of spin for GRGs is less as compared to their sample studies. The low spin value of GRGs is also indicative of their accretion rate being low. The reduction in accretion rate also indicates a decline in radiative efficiency, where a large part of accretion power gets converted into relativistic jets, which are mostly kinetic in nature than radiative (Ho 2008). Other theoretical and empirical studies (Heinz et al. 2007; Körding et al. 2008) have also shown that a large part of accretion power is transferred to jets. Observations (Reynolds 2019) from X-ray reflection of nearly two dozen SMBHs (prone to bias) have shown that the higher mass black holes ($\geq 10^8 \text{ M}_{\odot}$) tend to have low spin ($a \leq 0.7$) values, which is quite similar to our results for the GRGs, though our average spins are much lower. Note, it is not ideal to compare properties X-ray selected AGN sample (as mentioned in Reynolds 2019) and radio selected AGN (like our GRGs).

The two correlations as seen in Fig. 10 (a) and Fig. 10 (b) together, bring out the possible explanation of how magnetic field and spin are affecting the kinetic output of relativistic jets. Increment in spin leads to increment in $\lambda_{\rm Edd}$, and eventually, enhances the conversion of $L_{\rm Edd}$ into Q_{Jet}. In other words, higher the Eddington ratio higher is the accumulation of magnetic flux near the black hole leading to saturation of magnetic field (MAD). It drives the magneto-rotational instabilities which carry away the angular momentum of the in-falling material and thus, control the accretion flow. The magnetic flux in the jetted output scales with the magnetic flux threading the black hole. Further, the spin twists the magnetic field lines around the black hole to transfer energy in the form of Poynting flux through jets. Therefore, the magneto-hydrodynamics and spin of black holes play a crucial role in formation of the powerful jets which could scale large distance.

5.5. Environment analysis

We have used the GRG-catalogue to determine how many GRGs possibly are hosted by BCGs in galaxy clusters, and therefore, we utilise the WHL galaxy cluster catalogue as done for SGS in Sec. 4.5. We find a total of 60 GRGs from the GRG-catalogue to be BCGs, residing in a dense cluster environment. These 60 BCG-GRGs clearly provide a shred of strong evidence that sparse environment alone is not responsible for the large size of GRGs, and powerful AGNs

like these can pierce through the dense cluster environment to grow to Mpc scales.

In Fig. 11 (a), we explore the relation between the sizes of the GRGs and the $\rm M_{200}$ of the respective galaxy clusters. We observe that GRGs with sizes ≥ 1 Mpc are not found in clusters with $\rm M_{200}$ greater than $2.5 \times 10^{14} \rm M_{\odot}$. Fig. 11 (b) shows the distribution of $\rm M_{200}$ of clusters with radioloud BCGs and BCG-GRGs, where we observe that radioloud BCGs occur in clusters with a wide range of $\rm M_{200}$. About 95% of the BCG-GRGs in our sample are located in clusters with $\rm M_{200}$ lesser than $2 \times 10^{14} \rm M_{\odot}$. Below we test if this result is statistically significant. Interestingly, no GRGs found to be residing in the cluster environment is observed to grow beyond the virial radius ($\rm R_{200}$) of the host cluster. Also, we find no correlation between the total $\rm P_{1400}$ of the GRGs and the mass of the cluster.

The K-S test on the distributions of M_{200} of BCG-GRGs and radio-loud BCGs gives the p-value of 0.83, which indicates that both the distributions are identical. If we take the ratio of the number of BCG-GRGs to the radio-loud BCGs in the first four mass (M_{200}) bins, we get 0.0055, 0.0061, 0.0033 and 0.0099, respectively, with an average value of 0.0062. If we assume this ratio to be true for all mass bins, then this indicates that we should expect only 0.62 % of radio-loud BCGs in clusters to be GRGs. The cosmological halo mass function of evolving structures shows that the abundance of low mass clusters is much higher than the abundance of high mass clusters in the local Universe (Sheth et al. 2001). Also, as the number of high mass clusters is interestingly very low, we get an even lower number of radio-loud BCGs hosting GRGs in the cluster environment. For example, if we take the mass bin around $7\times10^{14} M_{\odot}$ (6th bin), then there are 14 radio-loud BCGs in this bin. The average value of the ratio, 0.0062, suggests that we needed around 160 clusters of such high masses with a radio-loud BCG to detect at least one GRG. Therefore, the probability of finding a radio-loud BCG as a GRG in clusters is indeed very low, and it is very difficult to find them in massive clusters.

We also observe that the radio morphology of BCG-GRGs is not linear and symmetric but is rather deformed to certain degrees. This clearly illustrates the effect of the environment on the GRGs, which, despite the resistance of the intra-cluster medium and cluster weather, are able to grow to megaparsec scale.

In order to study the environment of the GRGs more thoroughly, we need to find out precisely what fraction of GRG population resides in clusters (BCG or a cluster member), which can be done only via a controlled and complete sample. We will be focusing on this aspect in our future work under project SAGAN.

6. Discussion

Based on our study described in the paper so far, we further discuss the overall results in the context of GRGs in this section. Nearly 20 years old surveys like NVSS, when combined with other radio and optical surveys, still have a lot of discovery potential. This is evident from the large sample (SGS) of 162 GRGs discovered by us, and thereby, increasing the overall known GRG population by nearly 25%.

Our GRG compilation work under project SAGAN leading to the construction of the GRG-catalogue has revealed

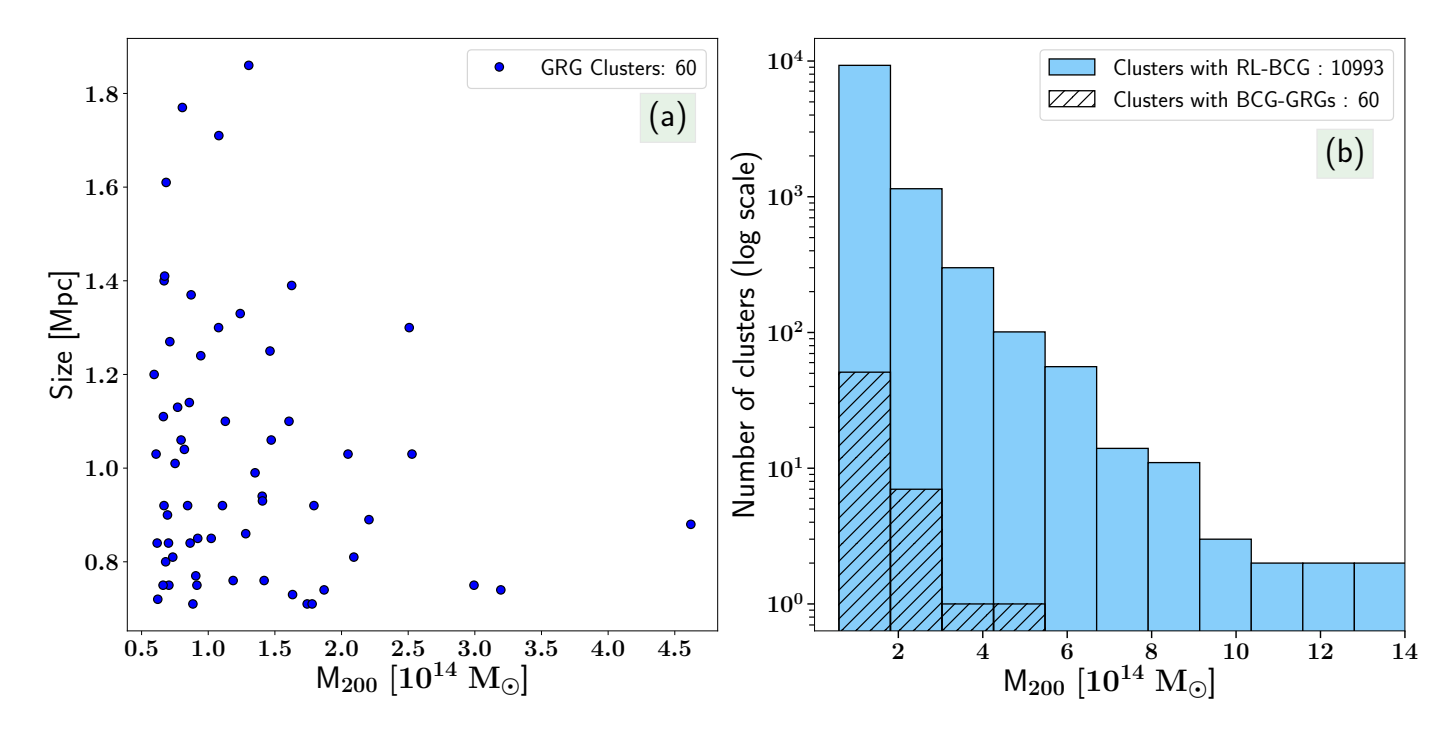


Fig. 11: Sub-figure (a): The X-axis shows the mass of the galaxy cluster hosting the BCG-GRG and on the Y-axis the size of the GRG is shown. Sub-figure (b): Distribution of M_{200} of clusters with radio-loud BCGs and clusters with GRG as BCGs from GRG-catalogue.

that GRGs are not as rare as thought of before. Nevertheless, the GRG-catalogue consists of only 820 sources, which is still quite rare when compared to the overall RG population. This large compilation of GRGs has enabled us to reveal new properties of these rare sources, leading to its better understanding.

The central engine powering the GRGs is hosted by both galaxies (GRGs) and quasars (GRQs). We have studied the key similarities and dissimilarities in their properties to understand the influence of the central powering engine on their respective properties. Our analysis (Sec. 5.1) shows that the projected linear size of the GRQs and GRGs is nearly similar (from the homogeneous sample of LoTSS and SAGAN). Also, the GRQs are more powerful in terms of their central engine, P₁₄₀₀ and Q_{Jet}. This implies that the GRQs could scale megaparsec distances in lesser time than the GRGs. However, the study of their spectral indices reveals that both have similar distributions as well as a similar value of the spectral index. It has been shown (Dennett-Thorpe et al. 1999; Ishwara-Chandra & Saikia 2000) previously that the hotspots of RQs are steeper as compared to RGs and the same argument can be applicable to GRQs as well. Thus, the flatter core and steeper hotspots of GRQs counterbalance each other, resulting in similar spectral index like GRGs.

AGNs broadly are classified into two categories, namely the radiatively efficient (RE) mode and the radiatively inefficient (RI) mode. In the context of radio galaxies, these modes are referred to as HERGs (RE) and LERGs (RI) and similarly for GRGs as HEGRGs-LEGRGs. In literature, these modes are also referred to as the 'radiative mode' (RE) and the 'jet mode' (RI). The quasars lie in the RE mode; and below, in this discussion we will primarily focus on non-quasar AGNs, which does not include the GRQs.

The GRG-AGN activity (HEGRG and LEGRG) can regulate different characteristics of AGN in terms of radiative efficiency, and the formation and powering of relativistic jets. Best & Heckman (2012) concluded that HERGs are associated with lower mass black holes with high accretion rates as compared to LERGs. A similar kind of picture is reflected while dealing with properties of HEGRGs and LEGRGs using the GRG-catalogue, where our results (Sec. 5.2) too show that the $\lambda_{\rm Edd}$ is higher for HEGRGs as compared to LEGRGs. There is a significant overlap in the distribution of $\lambda_{\rm Edd}$ of HEGRGs and LEGRGs without a sharp boundary separating both populations. The high $\lambda_{\rm Edd}$ implies high accretion rate in HEGRGs, which possibly is responsible for producing powerful relativistic jets, which in turn could be accountable for the larger sizes of HEGRGs as compared to LEGRGs.

One of the most fundamental properties of the black hole is its mass (M_{BH}), and for SMBHs residing in AGNs, their masses are in the range of $\sim 10^7$ to 10^{10} M_{\odot}. The aim of carrying out a comparative study (Sec. 5.3) of AGN properties of RGs and GRGs is to possibly find factors that allow a tiny subset of RGs to grow to GRGs. Despite their $M_{\rm BH}$ distribution being very similar, the $\lambda_{\rm Edd}$ distribution varies with GRGs having predominantly lower values as compared to RGs. Our study clearly rules out the possibility of M_{BH} alone being the crucial factor for driving RGs to GRG scales. AGNs with low values ($\lambda_{\rm Edd} < 0.01$) of Eddington ratio follow the RIAF model, and therefore, our study shows that almost all the GRGs (except GRQs and few HEGRGs) seem to be fuelled via radiatively inefficient flows at low accretion rates. Objects with RIAFs have very low Eddington ratio, and hence, quite often there is a absence of the 'big blue bump'. This leads to accretion disk being under-luminous, and hence, weak in X-ray regime

(Ho 2008; Hardcastle 2018a). The formation of powerful jets is quite favourable in RIAFs due to the presence of thick disk structure, which boosts the large-scale poloidal component of the magnetic field, resulting in the launch of collimated jets (Rees et al. 1982; Meier 1999). Interestingly, Bagchi et al. (2014) reached the same conclusion for an extremely unusual GRG hosted by a spiral galaxy 2MASX J23453268-0449256 in an under dense environment, that the launch of powerful FR-II jets in it is facilitated by an advection-dominated, magnetized accretion flow at low Eddington rate onto a super massive and moderately spinning $a \sim 0.7$ central black hole. Thus, our previous and present results provide fundamental insight into accretion disk-relativistic jet coupling process in GRGs.

The RGs, as evident from their distribution of $\lambda_{\rm Edd}$ have higher mass accretion rate as well as high accretion efficiency too, which leads to the formation of powerful relativistic jets scaling to hundreds of kiloparsecs. We can further conjecture that GRGs at the start of their lives are RGs with higher $\lambda_{\rm Edd}$, which diminishes over a period of their growth to GRGs. The SMBHs that grow over a period of time via mergers and coherent disk accretion are most likely responsible for high spinning black holes (like quasars, seyferts and HERGs etc). On the other hand, the low spinning black holes (like GRGs) with high mass black holes were possibly formed by more isotropic chaotic accretion (Volonteri et al. 2005, 2013; Reynolds 2019).

Connecting the above to large scales, one of the most striking results obtained from the large sample of GRGs available to us is the radio morphology of GRGs. Both samples, LoTSS and SGS have >90% FR-II type GRGs, with FR-I type GRGs preferring low-excitation type AGN and FR-IIs high excitation type AGN. It is known that FR-I type RGs are mostly associated to clusters of galaxies and hence we can conclude (from a different chain of arguments compared to Sec. 5.5) that the GRGs preferentially avoid denser environments.

After, evaluating all the properties derived by us (as mentioned above) and their distributions along with the comparisons with RG samples, it is clear that it is not one sole factor/parameter but a right combination of multiple parameters which lead to the growth of GRGs. A possibility to be explored in future studies is to estimate and assess the fueling process of the SMBHs in GRGs in conjunction with their environments.

7. Summary

In this paper, we present a sample of 162 new GRGs (also called the SAGAN GRG Sample or SGS for short) with a projected linear size above ~ 0.7 Mpc, based on our searches from NVSS. This investigation used the Proctor's catalogue of probable GRG candidates and employed the visual search for extended sources. The ancillary data from the radio surveys like the FIRST, TGSS, WENSS and VLASS were very crucial in confirming the morphology of these sources. The identification and classification of the hosts are made using spectroscopic data from the SDSS, Pan-STARRS, and mid-IR data from the WISE survey. As a result, 23 out of 162 radio giants have been confirmed to be GRQs while the rest are GRGs. The mean and median values of several properties of the GRGs are presented in Table. 3.

A brief summary of our results is given below:

- 1. GRGs are known to be relatively rare and considering that only ~ 658 are known so far; the addition of another 162 new sources increases the known population by $\sim 25\%$. This helps for better statistical studies of these objects in multiple wavelengths to decipher the reasons for their gigantic nature and rarity.
- 2. SGS: The projected linear sizes of all sources in SGS lie in the range of ~ 0.71 Mpc to ~ 2.82 Mpc, with P_{1400} as low as 10^{23} W Hz⁻¹ at 1400 MHz.
- 3. SGS: About 92% of the GRGs in SGS have FR-II morphology. The rest of the sample consists of 8 FR-I, 4 HyMoRS and 1 DDRG. It is prominent that giants are dominated by FR-II population similar to RGs.
- 4. The study of GRGs of two AGN types (galaxy/quasar) reveals that the radio power and jet kinetic power are higher in GRQs with respect to GRGs. It clearly shows that GRQs have more powerful central engines than GRGs. However, the linear size and spectral index of both the population are similar.
- 5. The study of high and low excitation GRGs reveals that the ones with lower black hole mass, higher efficiency of accretion, radio power and jet kinetic power, i.e. the HEGRGs grow to the maximum extent.
- 6. We establish for the first time using our large database of GRGs- the GRG-catalogue that the radio spectral index (between 150 MHz and 1400 MHz) of RGs and GRGs is similar.
- 7. We find that, the black holes hosted by GRGs are spinning slowly with maximum spin upto ~ 0.3 , which possibly indicates a chaotic accretion history of the host galaxies of GRGs.
- 8. There is a strong correlation between $\lambda_{\rm Edd}$ and the amount of Eddington luminosity being converted to jet kinetic power. It significantly implies that efficient accretion is responsible for the formation of powerful jets, and disk-jet coupling is at play.
- 9. We find 60 GRGs hosted by BCGs in dense cluster environments. The analysis of their linear sizes indicates the size of BCG-GRGs is limited with respect to other GRGs in the same redshift range due to the presence of the dense ambient medium. Thus, from our study and the previous results from the literature, it is apparent that the local environment indeed plays a role in the growth of GRGs, but is not the sole factor impacting their size.

Acknowledgements

LCH was supported by the National Key R&D Program of China (2016YFA0400702) and the National Science Foundation of China (11721303, 11991052). PD, JB, FC, and BG gratefully acknowledge generous support from the Indo-French Center for the Promotion of Advanced Research (Centre Franco-Indien pour la Promotion de la Recherche Avancee) under programme no. 5204-2. We thank IUCAA (especially Radio Physics Lab), Pune for providing all the facilities during the period the work was carried out. We gratefully acknowledge the use of Edward (Ned) Wright's online Cosmology Calculator. This research has made use of the VizieR catalogue tool, CDS, Strasbourg, France (Ochsenbein et al. 2000).

References

- Abazajian, K. N., Adelman-McCarthy, J. K., Agüeros, M. A., et al. 2009, ApJS, 182, 543
- Abolfathi, B., Aguado, D. S., Aguilar, G., et al. 2018, The Astrophysical Journal Supplement Series, 235, 42
- Abramowicz, M. A. & Fragile, P. C. 2013, Living Reviews in Relativity, 16, 1
- Amirkhanyan, V. R. 2016, Astrophysical Bulletin, 71, 384
- Amirkhanyan, V. R., Afanasiev, V. L., & Moiseev, A. V. 2015, Astrophysical Bulletin, 70, 45
- Athreya, R. M. & Kapahi, V. K. 1998, Journal of Astrophysics and Astronomy, 19, 63
- Baade, W. & Minkowski, R. 1954, ApJ, 119, 206
- Bagchi, J., Vivek, M., Vikram, V., et al. 2014, ApJ, 788, 174
- Balbus, S. A. & Hawley, J. F. 1998, Rev. Mod. Phys., 70, 1
- Bardeen, J. M. 1970, Nature, 226, 64
- Bardeen, J. M., Press, W. H., & Teukolsky, S. A. 1972, ApJ, 178, 347 Becker, R. H., White, R. L., & Helfand, D. J. 1995, ApJ, 450, 559 Beckwith, K., Hawley, J. F., & Krolik, J. H. 2008, The Astrophysical
- Journal, 678, 1180–1199
- Begelman, M. C., Blandford, R. D., & Rees, M. J. 1984, Reviews of Modern Physics, 56, 255
- Bennett, A. S. 1962, MmRAS, 68, 163

- Beskin, V. S. 2010, Physics Uspekhi, 53, 1199 Best, P. N. & Heckman, T. M. 2012, MNRAS, 421, 1569 Best, P. N., Röttgering, H. J. A., & Lehnert, M. D. 1999, MNRAS, 310, 223
- Blandford, R. D. 1990, in Active Galactic Nuclei, ed. R. D. Blandford, H. Netzer, L. Woltjer, T. J. L. Courvoisier, & M. Mayor, 161-275
- Blandford, R. D. & Payne, D. G. 1982, MNRAS, 199, 883 Blandford, R. D. & Rees, M. J. 1974, MNRAS, 169, 395
- Blandford, R. D. & Znajek, R. L. 1977, MNRAS, 179, 433 Blanton, M. R. & Roweis, S. 2007, AJ, 133, 734

- Blundell, K. M., Rawlings, S., & Willott, C. J. 1999, AJ, 117, 677 Bock, D. C.-J., Large, M. I., & Sadler, E. M. 1999, AJ, 117, 1578 Bolton, A. S., Schlegel, D. J., Aubourg, É., et al. 2012, AJ, 144, 144 Bridle, A. H., Davis, M. M., Meloy, D. A., et al. 1976, Nature, 262,
- Bruni, G., Panessa, F., Bassani, L., et al. 2019, ApJ, 875, 88 Bruni, G., Panessa, F., Bassani, L., et al. 2020, arXiv e-prints, arXiv:2003.09183
- Burbidge, G. R. 1956, ApJ, 124, 416
- Capetti, A., Massaro, F., & Baldi, R. D. 2017, A&A, 601, A81
- Caretta, C. A., Maia, M. A. G., & Willmer, C. N. A. 2004, AJ, 128, 2642
- Chambers, K. C., Magnier, E. A., Metcalfe, N., et al. 2016, arXiv e-prints, arXiv:1612.05560
- Clarke, A. O., Heald, G., Jarrett, T., et al. 2017, A&A, 601, A25 Colla, G., Fanti, C., Ficarra, A., et al. 1970, A&AS, 1, 281
- Colless, M., Dalton, G., Maddox, S., et al. 2001, MNRAS, 328, 1039 Condon, J. J., Cotton, W. D., Greisen, E. W., et al. 1998, AJ, 115,
- Cotter, G., Rawlings, S., & Saunders, R. 1996, MNRAS, 281, 1081 Dabhade, P., Gaikwad, M., Bagchi, J., et al. 2017, MNRAS, 469, 2886 Dabhade, P., Röttgering, H. J. A., Bagchi, J., et al. 2020, A&A, 635,
- A_5
- Daly, R. A. 2011, MNRAS, 414, 1253 Daly, R. A. 2019, The Astrophysical Journal, 886, 37
- Danziger, I. J. & Goss, W. M. 1983, MNRAS, 202, 703
- de Bruyn, A. G. 1989, A&A, 226, L13
- Delli Veneri, M., Cavuoti, S., Brescia, M., Longo, G., & Riccio, G. 2019, MNRAS, 486, 1377
- Dennett-Thorpe, J., Bridle, A. H., Laing, R. A., & Scheuer, P. A. G. 1999, MNRAS, 304, 271
- Drake, C. L., McGregor, P. J., & Dopita, M. A. 2004, AJ, 128, 955 Dressler, A. & Shectman, S. A. 1988, AJ, 95, 284
- Eatough, R. P., Falcke, H., Karuppusamy, R., et al. 2013, Nature, 501,
- Ekers, R. D., Wall, J. V., Shaver, P. A., et al. 1989, MNRAS, 236, 737
- Fanaroff, B. L. & Riley, J. M. 1974, MNRAS, 167, 31P Fanidakis, N., Baugh, C. M., Benson, A. J., et al. 2011, MNRAS, 410, 53
- Ferrarese, L. & Merritt, D. 2000, ApJ, 539, L9
- Gao, J., Zou, H., Zhou, X., & Kong, X. 2018, ApJ, 862, 12
- Gebhardt, K., Bender, R., Bower, G., et al. 2000, ApJ, 539, L13
- Gopal-Krishna & Wiita, P. J. 2000, A&A, 363, 507
- Gopal-Krishna, Wiita, P. J., & Saripalli, L. 1989, MNRAS, 239, 173 Govoni, F., Falomo, R., Fasano, G., & Scarpa, R. 2000, A&A, 353,

- Griffin, A. J., Lacey, C. G., Gonzalez-Perez, V., et al. 2019, MNRAS, 487, 198
- Grupe, D., Beuermann, K., Thomas, H.-C., Mannheim, K., & Fink, H. H. 1998, A&A, 330, 25
- Gruppioni, C., Zamorani, G., de Ruiter, H. R., et al. 1997, MNRAS, 286, 470
- Gürkan, G., Hardcastle, M. J., & Jarvis, M. J. 2014, MNRAS, 438, 1149
- Hardcastle, M. 2018a, Nature Astronomy, 2, 273
- Hardcastle, M. J. 2018b, MNRAS, 475, 2768
- Hardcastle, M. J., Evans, D. A., & Croston, J. H. 2007, MNRAS, 376, 1849
- Heckman, T. M., Kauffmann, G., Brinchmann, J., et al. 2004, ApJ, 613, 109
- Heinz, S., Merloni, A., & Schwab, J. 2007, The Astrophysical Journal, 658, L9–L12
- Hinshaw, G., Larson, D., Komatsu, E., et al. 2013, ApJS, 208, 19 Ho, L. C. 2008, ARA&A, 46, 475
- Ho, L. C. & Kim, M. 2009, ApJS, 184, 398
- Hota, A., Sirothia, S. K., Ohyama, Y., et al. 2011, MNRAS, 417, L36 Huchra, J. P., Macri, L. M., Masters, K. L., et al. 2012, ApJS, 199,
- Hughes, S. A. & Blandford, R. D. 2003, ApJ, 585, L101
- Huynh, M. T., Jackson, C. A., & Norris, R. P. 2007, AJ, 133, 1331 Intema, H. T., Jagannathan, P., Mooley, K. P., & Frail, D. A. 2017, A&A, 598, A78
- Ishwara-Chandra, C. H. & Saikia, D. J. 1999, MNRAS, 309, 100
- Ishwara-Chandra, C. H. & Saikia, D. J. 2000, MNRAS, 317, 658 Ishwara-Chandra, C. H., Sirothia, S. K., Wadadekar, Y., Pal, S., & Windhorst, R. 2010, MNRAS, 405, 436
- Ito, H., Kino, M., Kawakatu, N., Isobe, N., & Yamada, a. 2008, The Astrophysical Journal, 685, 828
- Jennison, R. C. & Das Gupta, M. K. 1953, Nature, 172, 996
- Jones, D. H., Read, M. A., Saunders, W., et al. 2009, MNRAS, 399, 683
- Jones, P. A. 1989, Proceedings of the Astronomical Society of Aus-
- tralia, 8, 81 Kaiser, N., Aussel, H., Burke, B. E., et al. 2002, in Society of Photo-Optical Instrumentation Engineers (SPIE) Conference Series, Vol.
- 4836, Proc. SPIE, ed. J. A. Tyson & S. Wolff, 154–164 Kaiser, N., Burgett, W., Chambers, K., et al. 2010, in Society of Photo-Optical Instrumentation Engineers (SPIE) Conference Series, Vol. 7733, Proc. SPIE, 77330E
- Kaldare, R., Colless, M., Raychaudhury, S., & Peterson, B. A. 2003, MNRAS, 339, 652
- Kapahi, V. K., Athreya, R. M., van Breugel, W., McCarthy, P. J., &
- Subrahmanya, C. R. 1998, ApJS, 118, 275 Kapińska, A. D., Terentev, I., Wong, O. I., et al. 2017, AJ, 154, 253 Kellermann, K. I., Pauliny-Toth, I. I. K., & Williams, P. J. S. 1969, ApJ, 157, 1
- King, A. R. & Pringle, J. E. 2006, MNRAS, 373, L90
- King, A. R., Pringle, J. E., & Hofmann, J. A. 2008, Monthly Notices of the Royal Astronomical Society, 385, 1621-1627
- Kirk, J. G. & Schneider, P. 1987, ApJ, 315, 425
- Klamer, I. J., Ekers, R. D., Bryant, J. J., et al. 2006, MNRAS, 371, 852
- Klein, U., Mack, K.-H., Gregorini, L., & Vigotti, M. 2003, A&A, 406, 579
- Kolmogorov, A. 1933, Inst. Ital. Attuari, Giorn., 4, 83
- Komberg, B. V. & Pashchenko, I. N. 2009, Astronomy Reports, 53,
- Körding, E. G., Jester, S., & Fender, R. 2008, MNRAS, 383, 277 Kormendy, J. & Ho, L. C. 2013, Annual Review of Astronomy and Astrophysics, 51, 511–653
- Kozieł-Wierzbowska, D., Goyal, A., & Żywucka, N. 2019, arXiv eprints, arXiv:1912.09959
- Kozieł-Wierzbowska, D. & Stasińska, G. 2011, MNRAS, 415, 1013
- Krolik, J. H. & Chen, W. 1991, AJ, 102, 1659
- Kronberg, P. P., Wielebinski, R., & Graham, D. A. 1986, A&A, 169,
- Kuźmicz, A., Jamrozy, M., Bronarska, K., Janda-Boczar, K., & Saikia, D. J. 2018, ApJS, 238, 9
- Lacy, M., Baum, S. A., Chandler, C. J., et al. 2019, arXiv e-prints, arXiv:1907.01981
- Lacy, M., Rawlings, S., Saunders, R., & Warner, P. J. 1993, MNRAS, 264, 721
- Laing, R. A. & Peacock, J. A. 1980, MNRAS, 190, 903
- Laing, R. A., Riley, J. M., & Longair, M. S. 1983, MNRAS, 204, 151 Lake, S. E., Wright, E. L., Petty, S., et al. 2012, AJ, 143, 7 Lara, L., Cotton, W. D., Feretti, L., et al. 2001, A&A, 370, 409

- Law-Green, J. D. B., Eales, S. A., Leahy, J. P., Rawlings, S., & Lacy, M. 1995, MNRAS, 277, 995
- Letawe, G., Courbin, F., Magain, P., et al. 2004, A&A, 424, 455 Lynden-Bell, D. 1969, Nature, 223, 690
- Machalski, J. 1998, A&AS, 128, 153
- Machalski, J., Jamrozy, M., & Zola, S. 2001, A&A, 371, 445 Machalski, J., Koziel-Wierzbowska, D., & Jamrozy, M. 2007, Acta Astron., 57, 227
- Machalski, J., Kozieł-Wierzbowska, D., Jamrozy, M., & Saikia, D. J. 2008, ApJ, 679, 149 Mack, K. H., Klein, U., O'Dea, C. P., Willis, A. G., & Saripalli, L.
- 1998, A&A, 329, 431
- Magorrian, J., Tremaine, S., Richstone, D., et al. 1998, AJ, 115, 2285 Mahatma, V. H., Hardcastle, M. J., Williams, W. L., et al. 2018, MNRAS, 475, 4557
- Mahony, E. K., Morganti, R., Prandoni, I., et al. 2016, MNRAS, 463,
- Malarecki, J. M., Jones, D. H., Saripalli, L., Staveley-Smith, L., & Subrahmanyan, R. 2015, MNRAS, 449, 955
- Marconi, A., Risaliti, G., Gilli, R., et al. 2004, MNRAS, 351, 169 McCarthy, P. J., Kapahi, V. K., van Breugel, W., et al. 1996, ApJS,
- McGreer, I. D., Helfand, D. J., & White, R. L. 2009, AJ, 138, 1925 McKinney, J. C. & Narayan, R. 2007, MNRAS, 375, 513
- McMullin, J. P., Waters, B., Schiebel, D., Young, W., & Golap, K. 2007, in Astronomical Society of the Pacific Conference Series, Vol. 376, Astronomical Data Analysis Software and Systems XVI, ed. R. A. Shaw, F. Hill, & D. J. Bell, 127

- Meier, D. L. 1999, ApJ, 522, 753 Meier, D. L., Koide, S., & Uchida, Y. 2001, Science, 291, 84 Mikhailov, A. G. & Gredin, Y. N. 2018, Astronomy Reports, 62, 1 Miley, G. & De Breuck, C. 2008, A&A Rev., 15, 67
- Mingo, B., Croston, J. H., Hardcastle, M. J., et al. 2019, MNRAS, 488, 2701
- Mingo, B., Hardcastle, M. J., Croston, J. H., et al. 2014, MNRAS, 440, 269
- Mingo, B., Watson, M. G., Rosen, S. R., et al. 2016, MNRAS, 462, 2631
- Molina, M., Bassani, L., Malizia, A., et al. 2014, A&A, 565, A2 Narayan, R., Igumenshchev, I. V., & Abramowicz, M. A. 2003, PASJ, 55, L69
- Novikov, I. D. & Thorne, K. S. 1973, in Black Holes (Les Astres Occlus), 343–450
- Ochsenbein, F., Bauer, P., & Marcout, J. 2000, A&AS, 143, 23 Oort, M. J. A., Steemers, W. J. G., & Windhorst, R. A. 1988, A&AS,
- Pâris, I., Petitjean, P., Aubourg, É., et al. 2018, A&A, 613, A51 Parma, P., Murgia, M., de Ruiter, H. R., et al. 2007, A&A, 470, 875
- Peacock, J. A. 1983, MNRAS, 202, 615 Pirya, A., Saikia, D. J., Singh, M., & Chandola, H. C. 2012, MNRAS, 426, 758
- Planck Collaboration, Ade, P. A. R., Aghanim, N., et al. 2016, A&A, 594, A13
- Prescott, M., Whittam, I. H., Jarvis, M. J., et al. 2018, MNRAS, 480,
- Proctor, D. D. 2016, The Astrophysical Journal Supplement Series, 224, 18
- Ratcliffe, A., Shanks, T., Parker, Q. A., et al. 1998, MNRAS, 300, 417 Rees, M. J. 1971, Nature, 229, 312
- Rees, M. J. 1984, ARA&A, 22, 471
- Rees, M. J., Begelman, M. C., Blandford, R. D., & Phinney, E. S. 1982, Nature, 295, 17
- Rengelink, R. B., Tang, Y., de Bruyn, A. G., et al. 1997, A&AS, 124 Reynolds, C. S. 2019, Nature Astronomy, 3, 41
- Sadler, E. M., Cannon, R. D., Mauch, T., et al. 2007, MNRAS, 381, 211
- Sadler, E. M., Jackson, C. A., Cannon, R. D., et al. 2002, MNRAS, $329,\,227$
- Saikia, D. J., Konar, C., & Kulkarni, V. K. 2006, MNRAS, 366, 1391 Saikia, D. J., Thomasson, P., Jackson, N., Salter, C. J., & Junor, W. 1996, MNRAS, 282, 837
- Salpeter, E. E. 1964, ApJ, 140, 796
- Saripalli, L., Hunstead, R. W., Subrahmanyan, R., & Boyce, E. 2005, AJ. 130, 896
- Saripalli, L. & Malarecki, J. M. 2015, in Proceedings of "The many facets of extragalactic radio surveys: towards new scientific challenges" (EXTRA-RADSUR2015). 20-23 October 2015. Bologna, 44 Scheuer, P. A. G. 1974, MNRAS, 166, 513
- Scheuer, P. A. G. & Williams, P. J. S. 1968, ARA&A, 6, 321

- Schoenmakers, A. P., de Bruyn, A. G., Röttgering, H. J. A., & van der Laan, H. 2001, A&A, 374, 861
- Sebastian, B., Ishwara-Chandra, C. H., Joshi, R., & Wadadekar, Y. 2018, MNRAS, 473, 4926
- Sheth, R. K., Mo, H. J., & Tormen, G. 2001, MNRAS, 323, 1
- Shimwell, T. W., Tasse, C., Hardcastle, M. J., et al. 2019, A&A, 622,
- Shklovskii, I. S. 1955, AZh, 32, 215
- Sikora, M. & Begelman, M. C. 2013, ApJ, 764, L24
- Sirothia, S. K., Saikia, D. J., Ishwara-Chandra, C. H., & Kantharia, N. G. 2009, MNRAS, 392, 1403
- Smirnov, N. 1948, The Annals of Mathematical Statistics, 19, 279 Smolčić, V. 2009, ApJ, 699, L43
- Solovyov, D. I. & Verkhodanov, O. V. 2011, Astrophysical Bulletin, 66, 416
- Solovyov, D. I. & Verkhodanov, O. V. 2014, Astrophysical Bulletin, 69, 141
- Soltan, A. 1982, MNRAS, 200, 115
- Stern, D., Assef, R. J., Benford, D. J., et al. 2012, ApJ, 753, 30
- Subrahmanyan, R., Saripalli, L., & Hunstead, R. W. 1996, MNRAS, 279, 257
- Tamhane, P., Wadadekar, Y., Basu, A., et al. 2015, MNRAS, 453, 2438
- Tchekhovskoy, A., Narayan, R., & McKinney, J. C. 2011, MNRAS, 418, L79
- Thorne, K. S. 1974, ApJ, 191, 507
- Ueda, Y., Akiyama, M., Hasinger, G., Miyaji, T., & Watson, M. G. 2014, ApJ, 786, 104
- Ursini, F., Bassani, L., Panessa, F., et al. 2018, MNRAS, 481, 4250 Véron-Cetty, M. P. & Véron, P. 2006, A&A, 455, 773
- Volonteri, M., Madau, P., Quataert, E., & Rees, M. J. 2005, ApJ, 620,
- Volonteri, M., Sikora, M., & Lasota, J. 2007, The Astrophysical Journal, 667, 704-713
- Volonteri, M., Sikora, M., Lasota, J. P., & Merloni, A. 2013, ApJ, 775, 94
- Wei, J.-Y., Xu, D.-W., Cao, L., et al. 1998, A&A, 329, 511
- Wen, Z. L., Han, J. L., & Liu, F. S. 2012, The Astrophysical Journal Supplement Series, 199, 34
- Willis, A. G., Strom, R. G., & Wilson, A. S. 1974, Nature, 250, 625 Willott, C. J., Rawlings, S., Blundell, K. M., & Lacy, M. 1999, MN-RAS, 309, 1017
- Wright, E. L., Eisenhardt, P. R. M., Mainzer, A. K., et al. 2010, AJ, 140, 1868
- York, D. G., Adelman, J., Anderson, Jr., J. E., et al. 2000, AJ, 120, 1579
- Yuan, F. & Narayan, R. 2014, ARA&A, 52, 529
- Zamaninasab, M., Clausen-Brown, E., Tchekhovskoy, A. 2014, Nature, 510, 126 Zhang, X., Lu, Y., & Yu, Q. 2012, ApJ, 761, 5

Appendix A: Tables

symbolizes and megaparsecs, respectively. Columns (9) and (11) enlist the integrated flux densities (\dot{S}_{ν}) , and columns (10) and (12) list the total power P_{ν} of the spectroscopic redshifts while the rest are photometric redshift estimates. Columns (7) and (8) list the total projected linear size of the sources in arcmins sources at 1400 MHz and 150 MHz, respectively. Column (13) states the α_{150}^{1400} which is the two point spectral index between 1400 MHz (NVSS) and 150 MHz (TGSS). Column (14) contains redshift references (z_{ref}), given at the end of the table. Column (15) lists the morphological type of the sources:- I 'i' represents the sources found from independent manual search. Columns (2) & (3) represent the in DMS of the host galaxies of the GRGs. Column (4) represents the host type where G stands for r-band magnitude of the host galaxy from SDSS. In column (6), z† representing FR-I type, II representing FR-II type, HM representing probable HyMoRS type and RM representing remnant galaxy. galaxy and Q stands for quasar. In column (5), mr represents apparent Table A.1: In Column (1), Sr.No with superscript right ascension (RA) in HMS and declination (Dec)

(3) (4) (5) (7) (10) (10) (10) (11) (11) (11) (11) (11	Sr.No	(HMS)	Dec (DMS)	Type	mr	Z	Size	Size (Mpc)	$S_{1400} $ (mJy)	$\frac{P_{1400}}{(10^{25} \text{W Hz}^{-1})}$	S_{150} (mJy)	$^{\mathrm{P}_{150}}_{(10^{25}\mathrm{W~Hz}^{-1})}$	$lpha_{150}^{1400}$	$z_{ m ref}$	Morphology
0.04 65.25 12.84 10.0 G 17.15 at 0.01 0, 17.05 12.05 24.0 at 22.0 170.4 2.01 0 170.4 2.01 0 170.5 2.01 2.01 0 170.4 2.01 0	(1)	(2)	(3)	(4)	5)	(9)	(7)	(8)	(6)	(10)	(11)	(12)	(13)	(14)	(15)
00 11935 3 27 11838 G	П	00 04 50.25	12 48 40.10	ŋ	± 0.01	$0.14300 \pm 0.00020^{\dagger}$	7.01	1.09	1983 ± 60	11.10 ± 0.36		56.30 ± 11.30		12	II
00 11 103.2 3 10 10 105.3 2 17.18 2 10.2 4.2 2 10.2 4.2 1 10.2 4.2 2 10.2 4.2 1 10.2 4.2 1 11.5 0 + 10.0 0 0.0 1 10.0 1	2	$00\ 06\ 23.24$	26 35 44.66	ŭ	± 0.08	0.43600 ± 0.18820	4.88	1.71	339 ± 10	22.40 ± 22.90	1705 ± 343	113.00 ± 117.00	$^{\rm H}$	П	П
00.15 0.24.3 to 10 0.66.33 c 2.08.2 ±0.01 0.4578.1 ± 0.000007 3.60 t 2.001 0.41.3 to 3.75.2 c 2.002 0.01 0.41.4 to 3.75.2 c 2.002 0.01 0.41.4 to 3.75.2 c 2.002 0.02 0.02 0.02 0.02 0.02 0.02 0	က	$00\ 11\ 19.35$		Ü	± 0.00	$0.10714 \pm 0.00002^{\dagger}$	7.80	0.95	722 ± 22	2.18 ± 0.07	3564 ± 714	10.80 ± 2.16	$^{\rm H}$	_	II
00.18 13.2 1 14 13.3.2 G 18.24 ± 0.01 0.07541 ± 0.000077 2.75 1.20 377 ± 8 1.00 ± 2.90 16.65 ± 335 31.10 ± 0.4.30 0.7.74 ± 0.00 18 13.2 1 14 13.3.2 G 18.24 ± 0.01 0.07536 ± 0.000078 0.05 ± 0.02 ± 0.02 ± 0.02 0.02 0.02 0.02 0.0	4	$00\ 15\ 02.43$	$10\ 10\ 56.33$	ŭ	\pm 0.11	0.41900 ± 0.14980	4.67	1.60	47 ± 2	2.75 ± 2.32	196 ± 41	11.50 ± 10.00	0.64	П	П
00.8 15.22 1 43.34.5 G 18.57 ± 0.02 0.2304.0 ± 0.00005] 5.0 1 10. 852 ± 18 2 8.5 1.05 ± 0.05 ± 1.05 0.07 ± 0.07 0.07 0.0 0.0 0.0 0.0 0.0 0.0 0.0 0	20	00 17 41.45	08 27 55.72	o	± 0.01	$0.67841 \pm 0.00007^{\dagger}$	2.75	1.20	267 ± 8	51.60 ± 2.90	1662 ± 335	321.00 ± 66.30	$0.82 \pm$	П	П
0.03 6 2.29 0 - 0.2 85 21.55 G 18.77± 0.00 0.10.7500± 0.05690 9.72 1.78 1.20 0.10 0.17500± 0.00 0.00 0.00 0.00 0.00 0.00 0.00	9	$00 \ 18 \ 15.21$	$21\ 41\ 33.42$	Ü	± 0.02	$0.30256 \pm 0.00005^{\dagger}$	3.60	1.00	862 ± 26	24.80 ± 0.95		121.00 ± 24.30	0.71	_	II
0.03 8.03 8.0 1.3 3 C	7	$00\ 26\ 13.63$	$11\ 43\ 43.66$	ŭ	$\pm \ 0.01$	9.17500 ± 0.01620	9.72	1.78	582 ± 18	4.90 ± 1.02		16.80 ± 4.85	$0.55 \pm$	П	П
0.08 80.89 0.9 60 13.3 G 18.17 ± 0.02 0.2941G ± 0.000021 4.80 1.30 216 ± 7 58.7 ± 0.23 1089 ± 219 29.6 ± 5.90 0.07 ± 0.04 55.63 12.55 41.01 G 18.5 ± 0.02 0.29400 ± 0.00240 0.10 (1.03 132 ± 4 2.85 ± 1.54 (173 ± 326 50.23 50.2 ± 0.05 ± 0.00 55.4 ±	∞	003622.99	-025821.55	Ü	± 0.02	0.29400 ± 0.05690	4.51	1.23	188 ± 6	+	745 ± 155	19.70 ± 9.67	$0.62 \pm$	_	II
0045 37.11 38 25 63.23 G 0.160 ± 0.13 0.88000 ± 0.00540 3.14 1.65 222 ± 7 86.10 ± 23.40 1673 ± 336 649.00 ± 219.00 0.90 666 35.4 1.15 1.05 0.55 ± 1.15 1.29 ± 1.29 ± 1.24 0.055 ± 1.05 ±	6	00 38 09.89	$09\ 36\ 01.33$	ŭ	± 0.02	$0.29416 \pm 0.00005^{\dagger}$	4.80	1.30	216 ± 7	5.87 ± 0.23	1089 ± 219	29.60 ± 5.99	$0.72 \pm$	П	П
0.04 63361 125 54.101 G 18.54 ± 0.02 0.26400 ± 0.000340 4.10 135 ± 4 2.85 ± 1.154 613 ± 124 1.20 0.054 + 0.08 1	10		$38\ 25\ 03.23$	ŗ	± 0.13	0.89000 ± 0.09560	3.44	1.65		86.10 ± 23.40	$1673 \pm$	649.00 ± 219.00	$0.90 \pm$	Н	II
0.055 48.79 -22 31 16.50 G	11		125541.01	ŋ	± 0.02	0.26400 ± 0.06240	4.10	1.03		2.85 ± 1.54	$613 \pm$	12.90 ± 7.45		П	II
0.10 0.556 0.6 16 41.01 C 15.72 ± 0.00 0.11100 ± 0.00700 5.76 0.72 195 ± 6 0.63 ± 0.00 660 ± 135 2.12 ± 0.52 5 0.00 4.00 0.00 6.00 ± 0.00 € 0.00 ± 0.00 € 0.00 € 0.00 ± 0.00 € 0.00 ± 0.00 € 0.00 € 0.00 € 0.00 € 0.00 € 0.00 € 0.00 € 0.00 ± 0.00 € 0.00	12^i	55	$-22\ 31\ 16.50$	ტ	0 -	$0.11437 \pm 0.00015^{\dagger}$	6.25	0.80		0.61 ± 0.02	$555 \pm$	1.89 ± 0.39	+	2	II
0.0 23.734 0.1 20.026 C 18.44 ± 0.01 0.29200 ± 0.0000 4.20 1.14 312 ± 9 1.140 ± 283 37.00 ± 8.06 0.50 1.02 0.00 4.00 1.02 33.00 ± 16 0.58 ± 0.20 1.02 0.00	13	$01\ 00\ 52.60$	06 16 41.01	ŋ	± 0.00	9.11100 ± 0.00700	5.76	0.72		0.63 ± 0.09	∓ 099	2.12 ± 0.52		П	II
0.103 64.05 4.2 99.35.65 G	14	02	$04\ 21\ 00.26$	ტ	± 0.01	0.29200 ± 0.01000	4.20	1.14		8.23 ± 0.72	$1404\ \pm$	37.00 ± 8.06		9	II
$\begin{array}{cccccccccccccccccccccccccccccccccccc$	15	01 03 40.05	$42\ 39\ 35.63$	ŭ	± 0.00	9.13500 ± 0.00720		1.02		2.58 ± 0.31	$2039 \pm$	9.94 ± 2.30		_	II
$\begin{array}{cccccccccccccccccccccccccccccccccccc$	16			ŭ	± 0.01	9.12600 ± 0.01290		0.87	205 ± 6	0.88 ± 0.20	1		1	П	$_{ m HM}$?
$\begin{array}{cccccccccccccccccccccccccccccccccccc$	17	$01 \ 08 \ 03.52$	27 00 01.99	Ü	± 0.02	0.32700 ± 0.05530		1.17	696 ± 21	23.60 ± 9.30	3087 ± 618	105.00 ± 46.20	0.67 ± 0.21	П	II
011104.70 -144 23 32.60 G - 0.010406 ± 0.00015† 3.61 1.55 46 ± 2 7.78 ± 0.38	18	$01\ 09\ 36.45$	$25\ 24\ 03.76$	Ü	± 0.16	0.58100 ± 0.04760		1.39	202 ± 6	28.90 ± 5.91	1729 ± 347		0.96 ± 0.21	П	II
$\begin{array}{cccccccccccccccccccccccccccccccccccc$	19	01 11 04.70	$-14\ 22\ 32.60$	Ü	0 -	$0.10406 \pm 0.00015^{\dagger}$		0.80	402 ± 12	1.11 ± 0.04	996 ± 201	2.75 ± 0.56		2	II
$\begin{array}{cccccccccccccccccccccccccccccccccccc$	20^i	$01\ 12\ 22.34$		c	0 -	$0.65312 \pm 0.00015^{\dagger}$		1.55	46 ± 2	7.78 ± 0.38		,	1	2	HM?
$\begin{array}{cccccccccccccccccccccccccccccccccccc$	21	01 13 41.11	$01 \ 06 \ 08.52$	Ü	± 0.01	9.28100 ± 0.00001		1.12	383 ± 12	9.36 ± 0.35	1858 ± 373	45.40 ± 9.15	0.71 ± 0.21	П	II
$\begin{array}{cccccccccccccccccccccccccccccccccccc$	22	$01\ 14\ 30.75$	05 08 30.64	ŭ	± 0.01	$0.20456 \pm 0.00003^{\dagger}$		1.35	229 ± 7	2.73 ± 0.10	902 ± 181	10.70 ± 2.17	+	П	II
$\begin{array}{cccccccccccccccccccccccccccccccccccc$	23^i	01 14 40.34	$-36\ 16\ 31.80$	IJ		$0.11207 \pm 0.00011^{\dagger}$		0.89	61 ± 3	0.20 ± 0.01	ı	1	1	2	I
$\begin{array}{cccccccccccccccccccccccccccccccccccc$	24	23	$43\ 12\ 55.78$	ŭ	± 0.03	0.40900 ± 0.05650		1.65	436 ± 13	25.10 ± 8.27	+		0.75 ± 0.21	Н	II
$\begin{array}{cccccccccccccccccccccccccccccccccccc$	25		07 03 37.11	ŭ	± 0.00	0.09800 ± 0.01010		1.17	98 ± 4	0.25 ± 0.06		1	1	Н	II
$\begin{array}{cccccccccccccccccccccccccccccccccccc$	26	$\frac{5}{8}$	$24\ 31\ 52.10$	Ü	± 0.01	$0.16455 \pm 0.00002^{\dagger}$		0.95	100 ± 4	0.76 ± 0.03	1	1	1	_	Π
$\begin{array}{cccccccccccccccccccccccccccccccccccc$	27	33	$-08\ 24\ 16.52$	Ü	± 0.00	$0.14893 \pm 0.00013^{\dagger}$		0.92	234 ± 7	1.40 ± 0.05	+	5.27 ± 1.07	+	П	II
$\begin{array}{cccccccccccccccccccccccccccccccccccc$	28	$01\ 35\ 36.11$	$50\ 40\ 38.54$	Ü	± 0.04	0.47600 ± 0.01810		1.68	86 ± 3	6.49 ± 0.68	285 ± 61	21.40 ± 5.07	+	П	II
$\begin{array}{cccccccccccccccccccccccccccccccccccc$	29	$01\ 42\ 08.56$	-064143.4	Ü	∓ 0.00	$0.12447 \pm 0.00015^{\dagger}$		0.89	138 ± 5	0.56 ± 0.02	\mathbb{H}	1.75 ± 0.36	\mathbb{H}	7	II
$\begin{array}{cccccccccccccccccccccccccccccccccccc$	30	48	$06\ 22\ 43.26$	Ü	± 0.03	0.32000 ± 0.03650		0.96	445 ± 13	15.00 ± 3.99	\mathbb{H}	91.60 ± 30.40		\vdash	II
$\begin{array}{cccccccccccccccccccccccccccccccccccc$	31	52	$-30\ 33\ 19.00$	Ü		$0.16999 \pm 0.00021^{\dagger}$		0.94	57 ± 2	0.46 ± 0.02	,	1	1	က	П
$\begin{array}{cccccccccccccccccccccccccccccccccccc$	32	$\frac{5}{2}$	$24\ 51\ 36.38$	ŋ	± 0.01	$0.17660 \pm 0.00002^{\dagger}$		0.92	81 ± 3	0.69 ± 0.03	+	+	+	П	II
$\begin{array}{cccccccccccccccccccccccccccccccccccc$	33	25	$-31\ 37\ 37.00$	ŋ		$0.11000 \pm 0.00021^{\dagger}$		0.71	85 ± 3	0.27 ± 0.01	+	+	0.58 ± 0.26	3	II
$\begin{array}{cccccccccccccccccccccccccccccccccccc$	34	$03\ 21\ 25.91$		ŋ	± 0.00	0.06155 ± 0.00014		0.87	260 ± 8	0.25 ± 0.01	1	1	1	4	Ι
$\begin{array}{cccccccccccccccccccccccccccccccccccc$	35	21		ŋ	± 0.02	0.36530 ± 0.01000	3.28	1.03	401 ± 12	18.70 ± 1.43	+	139.00 ± 29.60	0.90 ± 0.21	2	II
$\begin{array}{cccccccccccccccccccccccccccccccccccc$	36	$03\ 25\ 33.95$		ŋ		$0.06300 \pm 0.00015^{\dagger}$	12.41	0.93	209 ± 7	0.21 ± 0.01	1	1	1	18	II
$\begin{array}{cccccccccccccccccccccccccccccccccccc$	37			ŭ	± 0.07	\geq	4.08	1.62	+	+	\mathbb{H}	129.00 ± 32.50		9	П
$03\ 50\ 45.56\ -18\ 18\ 29.80\ G \qquad - \qquad 0.17474\pm 0.00015^{\dagger}\ 5.50\ 1.01 \qquad 141\ \pm 5 \qquad 1.19\pm 0.04 \qquad 555\pm 114 \qquad 4.71\pm 0.96 0.62\pm 0.03$	38	$03\ 49\ 10.95$	$05\ 34\ 26.69$	Ü	± 0.02		5.06	1.50	+	+	1	1	1	1	П
$03\ 53\ 39.31\ -01\ 13\ 19.73\ \ \ G$ $16.85\ \pm\ 0.01\ \ 0.19100\ \pm\ 0.00970\ \ 5.69\ \ 1.12$ $199\ \pm\ 6$ $2.08\ \pm\ 0.25$ $970\ \pm\ 196$ $10.10\ \pm\ 2.35$ $0.71\ \pm\ 196$	39,	03 50 45.56		ۍ ري		+1 -	5.50	1.01	+ -	+ -	+ -	щ-	+ -	7	п
	40	533		5	∓ 0.01	# 00	5.69	1.12	199 ± 6	2.08 ± 0.25	Н	+		-	

Table A.1: continued.

(') (Mpc)		_	M)		. (0)		(KIII)	(10~0 W Hz_1)		
(7)	(7)		,	(8)	(6)	(10)	(11)	(12)	13)	(14)
$\pm 0.05000^{\dagger} 5.72$	$\pm 0.05000^{\dagger} 5.72$		0	0.83		+ -	5957 ± 1191	27.50 ± 23.40	0.67 ± 0.21	
$-$ 0.07457 \pm 0.00015 $^{\circ}$ 9.95 0 19.38 $+$ 0.06 0.33100 $+$ 0.03880 5.14 1	$\pm 0.00015^{\circ}$ 9.95 $+ 0.03880$ 5.14		○	1.51	205 ± 205	0.38 ± 0.01 2.38 + 0.66	382 + 78	-13.70 + 4.69	0.79 + 0.21	N -
0.07 0.30900 ± 0.04670 4.32	0.04670 4.32			1.21	64 ± 2	1.93 ± 0.68	314 ± 65	9.48 ± 3.85		
$0.07791 \pm 0.00015^{\dagger} 10.38$	10.38		0	0.95	341 ± 11	0.52 ± 0.02	+	+	+	∞
$0.00 0.24177 \pm 0.01000 11.95$	11.95		C1 ,	2.82	250 ± 8	4.41 ± 0.44	1 -	1 -	1 -	ر د د
$0.07 0.55200 \pm 0.05740 3.96$	3.96			1.57	103 ± 4	11.60 ± 2.98	495 ± 102	55.80 ± 18.30	0.70 ± 0.22	1
4.89	4.89			0.84	98 ± 3	0.71 ± 0.02	- 1000	- 00	1 -	,
$0.35000 \pm 0.05000 - 3.96$	0.05000 3.90			17.	927 ± 28	38.60 ± 13.00	0131 ± 1227	255.00 ± 99.50	0.85 ± 0.21	L5
$0.01 0.23100 \pm 0.03070 6.20$ 0.58500 + 0.06800 4.41	0.03070 - 6.20 $0.06800 - 4.41$			1.41	320 ± 10 185 + 6	3.30 ± 1.08 26.10 + 7.45	3934 ± 708 1355 + 273	60.20 ± 21.80 191.00 + 66.40	H +	
0.00890 5.22	$\pm 0.00890 5.22$	_	_	0.72	103 ± 4	0.42 ± 0.07	١,		-	1
5.42	0.02960 5.42			1.34	183 ± 6	3.81 ± 1.01	1307 ± 263	27.20 ± 9.01	$0.88 \pm$	1
$0.04 \ 0.47498 \pm 0.00003^{\dagger} \ 3.28$	$\pm 0.00003^{\dagger}$ 3.28			1.20	348 ± 11	29.10 ± 1.35	2181 ± 437	182.00 ± 37.10	0.82 ± 0.21	1
$\pm 0.00001^{\dagger} 5.10$	$\pm 0.00001^{\dagger} 5.10$			1.45	86 ± 3	2.72 ± 0.10	1	1	1	1
$0.00 \ 0.06933 \pm 0.00002^{\dagger} \ 9.18$	$\pm 0.00002^{\dagger} 9.18$		$\overline{}$	0.75	127 ± 4	0.15 ± 0.01		1	1	1
$0.00 \ 0.28347 \pm 0.00003^{\dagger} \ 4.00$	$\pm 0.00003^{\dagger} 4.00$			1.06	222 ± 7	5.70 ± 0.22	1406 ± 281	36.00 ± 7.26	0.83 ± 0.21	П
$0.01 \ 0.21979 \pm 0.00003^{\dagger} \ 4.30$	$\pm 0.00003^{\dagger} + 4.30$			0.94	502 ± 15	7.18 ± 0.22		1	1 -	
$0.01 \ 0.27649 \pm 0.00004^{T} \ 4.36$	$\pm 0.00004^{\intercal} 4.36$			1.13	337 ± 10	7.81 ± 0.29	1416 ± 286	32.80 ± 6.67	0.64 ± 0.21	
$0.00 0.12600 \pm 0.01180$		8.33		1.16	25 ± 2	0.11 ± 0.02	1	1	1	-
$0.01 0.24004 \pm 0.00003$	± 0.00003	5.55		1.30	123 ± 4	2.05 ± 0.08		7.37 ± 1.51	+	1
$\pm 0.00024^{\dagger} 2.94$	$\pm 0.00024^{\dagger} 2.94$			1.44	160 ± 5	69.30 ± 4.89	1000 ± 208	433.00 ± 94.00	0.82 ± 0.22	1
$0.01 \ 0.27300 \pm 0.00002^{\dagger} \ 4.85$	$\pm 0.00002^{\dagger} 4.85$			1.25	108 ± 4	2.50 ± 0.09	1	1	1	1
$\pm 0.00013^{\dagger}$	$\pm 0.00013^{\dagger}$	4.74		1.69	106 ± 4	7.85 ± 0.38	610 ± 126	45.00 ± 9.45	0.78 ± 0.22	1
$\pm \ 0.00004^{\dagger}$	$\pm \ 0.00004^{\dagger}$	5.99		0.82	100 ± 4	0.40 ± 0.02	1	1	1	1
0.13476	$\pm \ 0.00015^{\dagger}$	5.55		0.82	26 ± 2	0.13 ± 0.01	•	ı	1	2
	$\pm 0.00005^{\dagger}$	2.78		1.02	61 ± 2	4.89 ± 0.29	270 ± 67	21.60 ± 5.46	+	1
		5.53		1.32	206 ± 7	3.79 ± 1.00	+	20.50 ± 6.87		
$0.24600 \pm 0.05000^{\dagger}$	$\pm 0.05000^{\dagger}$	5.13		1.23	671 ± 20	12.50 ± 5.77	4164 ± 833	77.50 ± 39.00	0.82 ± 0.21	7
$0.00 \ 0.10513 \pm 0.00002^{\dagger}$	$\pm \ 0.00002^{\dagger}$	6.31		0.75	162 ± 5	0.47 ± 0.01	1	1	1	1
$0.01 0.20800 \pm 0.01490$		4.10		98.0	115 ± 4	1.49 ± 0.24	802 ± 164	10.40 ± 2.70	+	1
		5.29		1.19	91 ± 3	1.39 ± 0.19	404 ± 85	6.16 ± 1.52	\mathbb{H}	1
$0.01 \ 0.83633 \pm 0.00018^{\dagger}$		1.99		0.94	30 ± 2	8.65 ± 0.69		36.80 ± 8.28	+	2
$0.01 \ 0.14475 \pm 0.00002^{\dagger}$		5.90		0.93	288 ± 9	1.66 ± 0.06	1554 ± 312	8.97 ± 1.80	+	1
$0.01 \ 0.37417 \pm 0.00003^{\dagger}$		4.05		1.29	369 ± 11	17.00 ± 0.71	1660 ± 333	76.30 ± 15.50	+	1
$0.20300 \pm 0.03420 5.54$	5.54			1.14	315 ± 9	+	\mathbb{H}		+	1
$0.01 0.25900 \pm 0.03080 4.84$	$\pm 0.03080 4.84$			1.20	+	7.37 ± 2.01	1722 ± 345	35.00 ± 11.80	0.70 ± 0.21	
$\pm 0.00003^{\dagger} 5.09$	$\pm 0.00003^{\dagger} 5.09$			0.92	52 ± 3	0.44 ± 0.02	1	1	ī	_
$0.10032 \pm 0.00015^{\dagger} 6.84$	$\pm 0.00015^{\dagger} 6.84$		_	0.78	194 ± 6	0.51 ± 0.02	737 ± 149	1.92 ± 0.39	+	2
$0.01 \ 0.72638 \pm 0.00003^{\dagger} \ 3.60$	$\pm 0.00003^{\dagger} 3.60$			1.61	299 ± 9	66.60 ± 3.86	1721 ± 344	383.00 ± 78.90	\mathbb{H}	1
$0.14 0.62100 \pm 0.10070 2.75$	$\pm 0.10070 2.75$			1.15	84 ± 3	+	491 ± 101	75.70 ± 33.80	\mathbb{H}	1
0.01	$\pm 0.00002^{\dagger}$	3.97		1.09	360 ± 11	10.00 ± 0.39	1622 ± 326	45.00 ± 9.11	0.67 ± 0.21	
$\pm 0.00 \ 0.18079 \pm 0.00003^{\dagger} \ 4.23$	$\pm 0.00003^{\dagger}$	4.23		08.0	43 ± 2	0.40 ± 0.02	,	,	ı	1
$0.00 \ 0.11482 \pm 0.00002^{\dagger} \ 6.64$	$\pm \ 0.00002^{\dagger}$	6.64		98.0	2079 ± 62	7.24 ± 0.23	9212 ± 1843	32.10 ± 6.43	0.67 ± 0.21	П
$0.08853 \pm 0.00015^{\dagger}$ 7.43	$\pm 0.00015^{\dagger}$	7.43		92.0	639 ± 19	1.29 ± 0.04	2893 ± 580	5.84 ± 1.17	0.68 ± 0.21	2
$\pm 0.00100^{\dagger}$	$\pm 0.00100^{\dagger}$	6.93		0.91	1655 ± 50	+	8270 ± 1654	30.20 ± 6.07	+	11
$16.66 \pm 0.01 \ 0.17670 \pm 0.00005^{\dagger} \ 5.59$	$\pm 0.00005^{\dagger}$	5.59		1.03	409 ± 12	3.59 ± 0.12	1858 ± 374	16.30 ± 3.29	+	Ţ
0.00000 + 0.00000	+ 0.00005†	39.00		1.03	331 + 11	+ +	1 0001	1	+	18
± 0.00005 32.90	16.25 c0000.0 #		٦,	7.	Н	Н		ı		01

Table A.1: continued.

					`	1		777					
$ \begin{array}{ccc} (3) & (4) & (5) \end{array} $	(5)	(5)		(9)	-1	(8)	(6)	(10)	(11)	(12)	(13)	(14)	(15)
$G 16.12 \pm 0.00 0.10096$	$\pm 0.00 0.10096$	$\pm 0.00 0.10096$		$\pm 0.00001^{\dagger}$	6.48	0.75		0.44 ± 0.01	1	ı	1		П
$20\ 20\ 54.80$ G $18.39\ \pm\ 0.01$ $0.26300\ \pm\ 16.24\ 32.28$ G $19.53\ +\ 0.03$ 0.45908 +	$\pm 0.01 + 0.26300 + 0.03 + 0.45908 -$	$\pm 0.01 + 0.26300 + 0.03 + 0.45908 -$	_ '	± 0.01830 + 0.00003 [†]	5.09	1.06	213 ± 7 147 + 5	4.37 ± 0.71 10.80 ± 0.51	792 ± 161 677 + 137	16.20 ± 4.20 49.60 + 10.20	0.59 ± 0.21 0.68 + 0.21		===
			0.16474 ±	0.00015^{\dagger}	5.43	0.95	180 ± 6	+	+	4.10 ± 0.85	+	2	I II
G 18.90 ± 0.02 $0.33005 \pm$	± 0.02	± 0.02	0.33005 ±	0.01000	4.70	1.38		+ .	663 ± 135	22.90 ± 4.97	+ -	ر د	п
19 54 25.41 Q 17.52 \pm 0.01 0.23936 \pm 0.00006 35 19 11 97 C 17 81 \pm 0.01 0.20400 \pm 0.03060	$\pm 0.01 \ 0.23936 \pm 0.01 \ 0.20100 \pm 0.01$	$\pm 0.01 \ 0.23936 \pm 0.01 \ 0.20100 \pm 0.01$	0.23936 ± 0	0.000061	4.38 5.70	1.03	121 ± 4 170 ± 6	2.05 ± 0.08 2.15 ± 0.50	524 ± 109 1227 ± 246	8.87 ± 1.86	0.66 ± 0.22 0.86 \pm 0.21		II II
0 G 16.51 ± 0.00	± 0.00 ± 0.00	± 0.00 ± 0.00	0.13400 ± 0	± 0.00860 ± 0.00860	5.00	0.74	116 ± 4	+ +	432 ± 100	2.07 ± 0.56			==
G 18.65 ± 0.01 $0.20507 \pm$	\pm 0.01 0.20507 \pm	\pm 0.01 0.20507 \pm	+	± 0.01000	5.29	1.10	169 ± 5	1.99 ± 0.23	541 ± 118	6.37 ± 1.55	+	ಬ	П
G $17.02 \pm 0.01 \ 0.24863 \pm$	\pm 0.01 0.24863 \pm	\pm 0.01 0.24863 \pm	\mathbb{H}	0.00004^{\dagger}	4.44	1.07	310 ± 9	+	1133 ± 229	20.50 ± 4.16	0.58 ± 0.21	_	П
G $15.51 \pm 0.00 \ 0.13761 \pm$	$\pm 0.00 0.13761 \pm$	$\pm 0.00 0.13761 \pm$	+	0.00002^{\intercal}	5.66	0.85	133 ± 5	0.69 ± 0.02	ı	ı	ı	_	II
$0.13520 \pm 0.13520 \pm 0.12086 \pm 0.12$	$-$ 0.13520 \pm	$-$ 0.13520 \pm	H -	0.00021	5.03	0.75	67 ± 3	0.33 ± 0.01	- 0010	- 00 00 - 1	1 -	က -	E
G 17.22 \pm 0.01 0.17080 \pm 0 14.97 \pm 0.01 0.33789 \pm	± 0.01 0.17080 ± + 0.01 0.33789 ±	± 0.01 0.17080 ± + 0.01 0.33789 ±	H +	0.00001	7.10	1 10	252 + 8	9.00 ± 0.13	99.4 ± 300 99.4 ± 200	20.00 ± 4.13 35.70 ± 7.24	0.70 ± 0.21 0.61 ± 0.21		==
G 15.16 ± 0.00 0.11547 ±	± 0.00 0.11547 ±	± 0.00 0.11547 ±	+ +	0.00002†	7.12	0.92	221 ± 7	0.75 ± 0.02	443 ± 95	1.50 ± 0.32	+ +		= =
G $17.15 \pm 0.01 \ 0.14735 \pm$	$\pm 0.01 0.14735 \pm$	$\pm 0.01 0.14735 \pm$	+	0.00001^{\dagger}	5.88	0.94	219 ± 7	+	1054 ± 217	6.28 ± 1.29	+	_	Ι
G $16.90 \pm 0.01 \ 0.14262 \pm$	\pm 0.01 0.14262 \pm	\pm 0.01 0.14262 \pm	$^{\rm H}$	0.00002^{\dagger}	5.55	98.0	407 ± 13	+	1	1	1	_	П
G $18.43 \pm 0.02 \ 0.32180$	$\pm 0.02 0.32180$	$\pm 0.02 0.32180$	$0.32180 \pm 0.$	0.00005^{\dagger}	3.70	1.07	298 ± 9	9.74 ± 0.39	1318 ± 265	43.10 ± 8.73	+		П
Q 18.55 ± 0.01 0.36800	$\pm 0.01 0.36800$	$\pm 0.01 0.36800$	0.36800 ± 0.000	$\pm 0.00001^{\dagger}$	3.20	1.01	153 ± 5	7.07 ± 0.30	925 ± 188	42.70 ± 8.76	H -	17	= =
$G = 18.57 \pm 0.01$	± 0.01	± 0.01	0.22900 ± 0	.01890	4.11	0.93	.258 ± 8	4.08 ± 0.77	1488 ± 299	23.50 ± 6.44	0.78 ± 0.21	- ,	= :
4 G $^{16.36}$ \pm 0.00 (± 0.00	± 0.00	$0.20233 \pm 0.68233 \pm 0.6833 \pm$	000037	4.48	0.92	86 ± 3	1.02 ± 0.04) 1 1 1		1 -	٠ ,	Π:
22 43 14:96 G 19:10 ± 0:02 0:33200 ± 0:03020 12 25 10 39 G 15 81 + 0 00 0 12199 + 0 00002	+ 0.02 + 0.00	+ 0.02 + 0.00	$0.33200 \pm 0.033200 \pm 0.0312199 \pm 0.03121$	± 0.03620 + 0.00002†	5.7I	0.94	125 ± 4 95 + 3	4.57 ± 1.17 0.38 + 0.01	. 00 ± 153	27.50 ± 8.97	0.80 ± 0.21 -	- -	= =
G $20.29 \pm 0.04 \ 0.49979$	± 0.04 0.49979	± 0.04 0.49979		0.00004	3.78	1.42	326 ± 30	31.70 ± 1.53	2453 ± 498	239.00 ± 49.30	0.90 ± 0.21		ij
G $14.20 \pm 0.00 \ 0.07857 \pm$	\pm 0.00 0.07857 \pm	\pm 0.00 0.07857 \pm	+	0.00001^{\dagger}	8.32	0.77	315 ± 10	0.50 ± 0.02	,	1	- 1		П
G - 0.03914 \pm	+	+	+	0.00012^{\dagger}	17.11	0.82	447 ± 14	0.17 ± 0.01	1	1	1	4	II
7 G - 0.23860	- 0.23860	- 0.23860		0.01000^{\dagger}	4.34	1.01	194 ± 6	3.25 ± 0.33	789 ± 161	13.20 ± 2.97	+		Π
$01\ 24\ 22.04$ G $16.27\ \pm\ 0.00\ 0.20836\ \pm\ 0.00004$	$\pm 0.00 0.20836$	$\pm 0.00 0.20836$		$\pm 0.00004^{T}$	4.40	0.93	158 ± 5	1.94 ± 0.07	564 ± 116	6.94 ± 1.43	0.57 ± 0.21		==
G 18.00 ± 0.02 0.34100	$\pm 0.02 0.24100$ $\pm 0.02 0.36824$	$\pm 0.02 0.24100$ $\pm 0.02 0.36824$		± 0.00008†	3.95	1.25	517 ± 16	23.20 ± 0.96		116.00 ± 23.40			= =
Q 17.64 \pm 0.01 0.22687 \pm	\pm 0.01 0.22687 \pm	\pm 0.01 0.22687 \pm	+	0.00003^{\dagger}	4.58	1.03	946 ± 28	14.40 ± 0.51	4577 ± 916	69.60 ± 14.00		_	п
G $18.43 \pm 0.01 \ 0.31117$	\pm 0.01 0.31117	\pm 0.01 0.31117		0.00004^{\dagger}	4.66	1.32	262 ± 8	8.05 ± 0.32	1287 ± 258	39.50 ± 7.99	+		П
9 G - 0.10900	- 0.10900	- 0.10900	0.10900 ± 0	$\pm 0.00100^{\dagger}$	6.84	0.84	3399 ± 102	10.70 ± 0.40	17554 ± 3511	55.20 ± 11.10	+	6	II
G 17.80 ± 0.01	± 0.01	± 0.01	0.19000 ± 0	.02360	09.9	1.29	150 ± 5	1.56 ± 0.43	+ -	8.20 ± 2.83	+ -	₩,	= :
43 13 19.82 G 18.14 \pm 0.01 0.25069 \pm 0.00003/00 57 00 06 O 17.18 \pm 0.01 0.93493 \pm 0.00001 †	# 0.01 0.25069 # + 0.01 0.23423 +	# 0.01 0.25069 # + 0.01 0.23423 +	0.25069 ± 0	0.00003	0. r	1.38 1.10	116 ± 4 106 + 4	2.21 ± 0.09 1 74 + 0 06	611 ± 186	11.00 ± 2.28	0.72 ± 0.21	F	= -
G 19.26 ± 0.02 $0.32000 \pm$	± 0.02 0.32000 \pm	± 0.02 0.32000 \pm	1 +1	0.04470	5.33	1.54	508 ± 15	17.10 ± 5.58	3173 ± 635	107.00 ± 40.70	0.82 ± 0.21		Ι
G 17.68 ± 0.01 (± 0.01 (± 0.01 ($0.16963 \pm 0.$	$\pm 0.00002^{\dagger}$	5.38	96.0	236 ± 7	1.90 ± 0.07	1090 ± 221	8.77 ± 1.78	+	1	II
Q $17.77 \pm 0.01 \ 0.28321$	$\pm 0.01 0.28321$	$\pm 0.01 0.28321$	0.28321 ± 0.0	0.00002^{\dagger}	3.95	1.05	803 ± 24	17.90 ± 0.67	1473 ± 297	32.80 ± 6.67			II
ŭ	± 0.05	± 0.05	0.55200 ± 0	.03730	2.84	1.13	288 ± 9	33.20 ± 5.66	1542 ± 310	178.00 ± 46.60	0.75 ± 0.21	1	П
18 27 20.66 Q $16.49 \pm 0.00 \ 0.18588 \pm 0.00$	± 0.00	± 0.00	0.18588 ± 0.0	190000	5.70	1.10	1075 ± 32	10.80 ± 0.37	7046 ± 1411	70.90 ± 14.20	0.84 ± 0.21	19	П
G - $0.04871 \pm$	\mathbb{H}	\mathbb{H}	\mathbb{H}	0.00012^{\dagger}	30.50	1.80	467 ± 15	0.27 ± 0.01	1	1	1	4	$_{ m HM}$?
22 51 20.04 G 18.68 ± 0.02 0.33400 \pm	$\pm 0.02 0.33400$	$\pm 0.02 0.33400$	$0.33400 \pm$	± 0.01920	4.89	1.45	209 ± 7	7.83 ± 1.09	1401 ± 281	52.50 ± 12.70		1	П
G $18.05 \pm 0.01 \ 0.24000$	$\pm 0.01 0.24000$	$\pm 0.01 0.24000$	$0.24000 \pm$	± 0.07050	5.07	1.19	141 ± 5	+	652 ± 136	11.20 ± 7.77	+		II
0.07084	0.07084	0.07084		0.00012^{\dagger}	10.08	0.84	473 ± 14	+	+	1.60 ± 0.32	\mathbb{H}	4	П
ر 2	$-$ 0.09258 \pm	$-$ 0.09258 \pm	$0.09258 \pm$	0.00015^{\dagger}	8.58	0.91	361 ± 11	0.79 ± 0.03	1373 ± 297	3.02 ± 0.65	0.60 ± 0.22	2	П
0 G - 0.09458	- 0.09458	- 0.09458			13.01	1.41	238 ± 8	0.55 ± 0.02	ı	1	ı	2	= :
14 17 01.22 G 20.59 ± 0.06 0.23800 \pm	$\pm 0.06 0.23800$	± 0.06 0.23800	0.23800 ±	0.03980	5.36	1.25	43 ± 2	0.73 ± 0.28	1	1	1	-	=

Table A.1: continued.

$z_{ m ref}$ Morphology	(15)	II	II	II	II	II	II	II	II	II	Π	Π	Π	Π	II	II	II	II	II	II	II	Π	Π	II	II	II	II
$z_{ m ref}$	(14)	ಬ	2	_	14	_	20	\vdash	\vdash	2	9	2	П	П	_	_	_	_	10	_	က	9	13	_	_	_	П
α_{150}^{1400}	(13)	0.65 ± 0.21	0.53 ± 0.23	0.61 ± 0.23	0.73 ± 0.21	0.78 ± 0.21	+		0.57 ± 0.22	,	1.05 ± 0.22	,	0.48 ± 0.21	0.43 ± 0.25	0.82 ± 0.22	0.78 ± 0.21	0.65 ± 0.21	0.75 ± 0.21	0.59 ± 0.21	1	0.69 ± 0.21	0.47 ± 0.21	+	0.73 ± 0.21		1.07 ± 0.21	0.83 ± 0.21
P ₁₅₀	$(10^{-5} \text{W Hz}^{-1})$ (12)	43.40 ± 9.22	4.23 ± 0.93	13.30 ± 2.91	228.00 ± 45.80	84.80 ± 40.20	35.80 ± 7.21	2.31 ± 0.46	8.11 ± 1.75	•	17.20 ± 3.76		9.97 ± 3.11	2.04 ± 0.50	63.90 ± 33.80	15.30 ± 16.00	19.80 ± 22.00	50.80 ± 16.80	10.20 ± 2.07	1	112.00 ± 22.50	4.59 ± 1.22	8.98 ± 1.81	33.80 ± 22.20	14.00 ± 2.87	79.20 ± 16.10	7.01 ± 1.41
S ₁₅₀	(mJy) (11)	827 ± 167	381 ± 84	411 ± 89	19593 ± 3919	1548 ± 310	2351 ± 471	739 ± 149	633 ± 136		484 ± 99		951 ± 192	256 ± 62	973 ± 202	1748 ± 353	1266 ± 255	900 ± 183	1624 ± 329	ı	13186 ± 2637	1107 ± 223	686 ± 138	2190 ± 439	765 ± 156	1276 ± 257	2683 ± 539
P ₁₄₀₀	(10 ²² W Hz ¹) (10)	10.00 ± 0.74	1.28 ± 0.05	3.41 ± 0.15	44.20 ± 1.52	14.80 ± 6.40	8.79 ± 0.31	0.69 ± 0.02	2.28 ± 0.09	9.35 ± 0.32	1.63 ± 0.14	7.83 ± 0.42	3.43 ± 0.82	0.77 ± 0.03	10.30 ± 5.00	2.66 ± 2.74	4.63 ± 5.06	9.50 ± 2.48	2.75 ± 0.09	2.49 ± 1.32	24.10 ± 0.81	1.62 ± 0.28	3.01 ± 0.11	6.68 ± 4.18	3.00 ± 0.11	7.28 ± 0.33	1.10 ± 0.04
S ₁₄₀₀	(mJy) (9)	192 ± 6	116 ± 4	105 ± 4	3796 ± 114	271 ± 8	577 ± 17	223 ± 7	178 ± 6	205 ± 6	46 ± 2	39 ± 2	327 ± 10	97 ± 3	156 ± 6	304 ± 10	296 ± 9	168 ± 5	439 ± 13	91 ± 4	2826 ± 85	390 ± 12	230 ± 7	433 ± 13	164 ± 5	117 ± 4	421 ± 13
Size	(Mpc) (8)	1.49	0.78	0.99	0.94	1.47	0.94	0.75	1.57	0.94	1.79	1.70	0.93	0.87	1.49	1.74	1.82	2.22	0.80	2.30	1.09	0.91	0.89	1.36	1.68	1.50	1.13
Size	<u> </u>	4.50	3.85	3.41	4.61	4.44	4.17	6.05	7.33	2.98	6.23	3.86	4.64	4.81	4.30	9.49	8.00	6.63	4.91	8.47	5.97	6.50	4.10	00.9	7.00	4.50	9.93
Z	(9)	0.39769 ± 0.01000	$0.19953 \pm 0.00015^{\dagger}$	$0.32285 \pm 0.00002^{\dagger}$	$0.20047 \pm 0.00001^{\dagger}$	0.39800 ± 0.07250	$0.22880 \pm 0.00040^{\dagger}$	$0.10964 \pm 0.00002^{\dagger}$	$0.21246 \pm 0.00003^{\dagger}$	$0.36870 \pm 0.00015^{\dagger}$	0.31800 ± 0.01000	$0.70226 \pm 0.00018^{\dagger}$	0.19500 ± 0.02080	$0.17203 \pm 0.00002^{\dagger}$	0.42800 ± 0.08770	0.17500 ± 0.08170	0.23100 ± 0.11200	0.40500 ± 0.04420	$0.15216 \pm 0.00013^{\dagger}$	0.29400 ± 0.06740	$0.17420 \pm 0.00021^{\dagger}$	0.12600 ± 0.01000	$0.21600 \pm 0.00015^{\dagger}$	0.22800 ± 0.06330	$0.24700 \pm 0.00004^{\dagger}$	$0.40274 \pm 0.00002^{\dagger}$	$0.09940 \pm 0.00001^{\dagger}$
mr	(5)	18.81 ± 0.02	-	19.09 ± 0.02	-	18.77 ± 0.02	15.80 ± 0.00 (15.17 ± 0.00 (17.71 ± 0.01 (17.75 ± 0.01 (18.38 ± 0.01	-	16.35 ± 0.00	17.61 ± 0.01 (21.38 ± 0.11	19.88 ± 0.03	18.11 ± 0.01	19.67 ± 0.04	-	19.10 ± 0.02	-	15.11 ± 0.00	-	18.70 ± 0.01	-	20.25 ± 0.04 (16.34 ± 0.00 (
Type	(4)	U	ŭ	U	c	ŭ	Ç	U	U	c	ŭ	ŭ	U	U	ŭ	ŭ	ŭ	ŭ	ŭ	ŭ	ŭ	U	o	ŭ	ŭ	ŭ	ŭ
Dec	(DMS) (3)	-065910.19	$-25\ 06\ 11.03$	$07\ 35\ 30.28$	$-14\ 32\ 54.90$	19 40 43.51	$29\ 02\ 35.90$	19 31 43.76	01 00 41.80	$-05\ 29\ 58.10$	-070457.93	-165423.10	$31\ 42\ 07.94$	$06\ 19\ 25.49$	$16\ 07\ 53.60$	$16\ 20\ 16.77$	-070638.60	08 20 40.78	$-21\ 08\ 13.90$	$22\ 46\ 50.28$	$-27\ 28\ 12.40$	$14\ 57\ 59.35$	$-32\ 36\ 34.60$	$17\ 41\ 50.38$	08 28 17.25	$16\ 00\ 10.32$	$17\ 06\ 10.97$
`	(HMS) (2)	20 40 19.60	$20\ 59\ 47.18$	$21\ 30\ 39.21$	$21\ 37\ 45.20$	$21\ 49\ 20.70$	$22\ 15\ 36.84$	$22\ 18\ 15.55$	$22\ 31\ 14.32$	$22\ 32\ 49.13$	$22\ 38\ 36.14$	$22\ 46\ 13.00$	$22\ 46\ 21.66$	$22\ 51\ 03.39$	225125.53	225321.28	225356.30	225934.13	$23\ 10\ 46.70$	$23\ 16\ 22.32$	$23\ 19\ 56.30$	$23\ 23\ 44.52$	$23\ 25\ 11.80$	$23\ 35\ 12.35$	$23\ 41\ 37.14$	23 48 47.77	$23\ 59\ 11.07$
Sr.No	(1)	137	138	139	140	141	142	143	144	145	146	147^i	148	149	150	151	152	153	154	155	156	157	158	159	160	161	162

References. 1- SDSS; Abolfathi et al. 2018, 2-6dF; Jones et al. 2009, 3-2dF; Colless et al. 2001, 4-2MASS; Huchra et al. 2012, 5- Delli Veneri et al. 2019, 6- Gao et al. 2018, 7- McCarthy et al. 1996, 8- Dressler & Shectman 1988, 9- Best et al. 1999, 10- Caretta et al. 2004, 11- Danziger & Goss 1983, 12- Drake et al. 2004, 13- Grupe et al. 1998, 14- Ho & Kim 2009, 15- Machalski 1998, 16- Kaldare et al. 2003, 17- McGreer et al. 2009, 18- Ratcliffe et al. 1998, 19- Véron-Cetty & Véron 2006, 20- Wei et al. 1998

Table A.2: The table provides the following information - (4) σ : velocity dispersion (km s⁻¹) of hosts of giants, (5) M_{BH} : central black hole mass ($M_{\odot} \times 10^9$) estimated from M_{BH} - σ relation, (6) $S_{1400MHz}^c$: core flux density at 1400 MHz (FIRST), (7) λ_{Edd} : Eddington Ratio, (8) Q_{Jet} is the jet kinetic power.

Sr.No	Name	Type	σ	$ m M_{BH}$	S ^c _{1400MHz}	$\lambda_{ m Edd}$	Q _{Jet}
4.5	(-)	(-)	$({\rm km}\ {\rm s}^{-1})$	$(10^9 {\rm M}_{\odot})$	(mJy)	(10^{-4})	$(10^{43} \text{ erg s}^{-1})$
(1)	(2)	(3)	(4)	(5)	(6)	(7)	(8)
$\frac{1}{2}$	SAGANJ000450.25+124840.10 SAGANJ000623.24+263544.66	G G	-	-	-	-	$18.80 \\ 37.60$
3	SAGANJ000025.24+205544.00 SAGANJ001119.35+321713.83		245.65 ± 9.27	0.67 ± 0.14	_	_	3.59
4	SAGANJ001113.33+321713.83 SAGANJ001502.43+101056.33		240.00 ± 3.21	-	_	_	3.83
5	SAGANJ001741.45+082755.72		_	_	33.4 ± 1.0	_	107.00
6	SAGANJ001815.21+214133.42	Ğ	250.78 ± 18.45	0.75 ± 0.31	-	_	40.20
7	SAGANJ002613.63+114343.66	G	_	-	7.5 ± 0.2	-	5.61
8	SAGANJ003622.99-025821.55	G	-	-	-	-	6.56
9	SAGANJ003809.89 + 093601.33		264.24 ± 24.68	1.01 ± 0.53	0.6 ± 0.2	-	9.86
10	SAGANJ004517.11+382503.23		-	-	-	-	216.00
11	SAGANJ004653.63+125541.01	G	-	-	-	-	4.31
12	SAGANJ005548.79-223116.50		-	-	-	-	0.63
13	SAGANJ010052.60+061641.01	G G	-	10.21 0.25	-	-	0.70
14 15	SAGANJ010237.34+042100.26 SAGANJ010340.05+423935.63		-	10.31 ± 0.35	-	-	3.31
17	SAGANJ010803.52+270001.99		_	-	_	_	34.90
18	SAGANJ010936.45+252403.76	G	_	_	_	_	82.40
19	SAGANJ011104.70-142232.60	Ğ	_	-	_	_	0.92
21	SAGANJ011341.11+010608.52		228.75 ± 32.77	0.45 ± 0.36	1.2 ± 0.2	_	15.10
22	SAGANJ011430.75+050830.64	G	200.27 ± 11.28	0.21 ± 0.07	-	-	3.58
24	SAGANJ012359.92+431255.78	G	-	-	-	-	44.70
25	SAGANJ012532.16+070337.11	G	-	-	1.5 ± 0.2	-	-
26	SAGANJ012848.89+243152.10	G	219.19 ± 12.93		-	-	-
27	SAGANJ013327.24-082416.52		309.37 ± 8.32	2.45 ± 0.37	22.6 ± 0.7	-	1.76
28	SAGANJ013536.11+504038.54	G	-	-	-	-	7.13
29	SAGANJ014208.56-064143.4	G	-	-	0.5 ± 0.1	-	0.58
30	SAGANJ014849.35+062243.26	G G	-	176 029	-	-	30.50
32 33	SAGANJ015826.09+245136.38 SAGANJ022527.01-313737.00	G	291.95 ± 9.28	1.76 ± 0.32	-	-	$0.83 \\ 0.33$
35	SAGANJ032155.75+434640.78		_	-	<u>-</u>	_	46.50
37	SAGANJ034253.70-065224.40		_	_	_	_	43.00
39	SAGANJ035045.56-181829.80	G	_	_	_	_	1.57
40	SAGANJ035339.31-011319.73		_	_	_	_	3.38
41	SAGANJ042234.14-261643.20	G	_	-	-	-	9.16
43	SAGANJ051536.11+151821.31	G	-	-	-	-	4.58
44	SAGANJ054359.77+304748.28	G	-	-	-	-	3.16
45	SAGANJ061203.50-325747.00	G	-	-	-	-	0.52
47	SAGANJ070844.11+303012.73	G	-	-	-	-	18.60
48	SAGANJ072538.75+400412.52		310.02 ± 8.49	2.48 ± 0.38	39.7 ± 1.2	-	-
49	SAGANJ072805.86+503445.80		-	-	-	-	85.10
50 51	SAGANJ073205.49+155831.06	G G	-	-	-	-	20.10
	SAGANJ075021.33+163259.35		-	-	28 ± 02	-	63.50
$\frac{53}{54}$	SAGANJ082941.34+224758.41 SAGANJ084718.28+422341.33	G G	-171.43 ± 31.83		2.8 ± 0.2	-	$9.08 \\ 60.80$
55	SAGANJ084746.06+383139.33		-	-	6.9 ± 0.3	-	-
56	SAGANJ085349.78+145226.04	•	282.38 ± 7.52	1.46 ± 0.22	13.1 ± 0.4	0.64	-
57	SAGANJ085632.99+595746.89		-	-	26.3 ± 0.8	-	12.00
58	SAGANJ090111.78+294338.00	$\ddot{\mathrm{G}}$	250.21 ± 13.82	0.74 ± 0.23	15.7 ± 0.5	29.98	-
59	SAGANJ090123.31 + 191417.12		233.86 ± 21.87	0.51 ± 0.27	-	69.80	10.90
60	SAGANJ090640.80 + 142522.97	G	-	-	2.6 ± 0.2	-	-
61	SAGANJ090839.13+594512.82		305.75 ± 12.38	2.29 ± 0.52	4.3 ± 0.2	-	2.46
62	SAGANJ092256.47+245323.68	•	-	-	8.9 ± 0.3	-	144.00
63	SAGANJ092438.24+302837.14	-	-	- 0.00 1.00=	3.9 ± 0.2	-	-
64	SAGANJ092545.01+404739.04		215.24 ± 39.17		-	- 0.00	15.00
65 67	SAGANJ093421.58+382305.64		215.21 ± 17.46		2.0 ± 0.2	9.69	- 7 10
67 68	SAGANJ1095455.43+405914.11 SAGANJ100825.61-031734.82	Q G	-	-	3.0 ± 0.2	-	7.19 6.83
69	SAGANJ100825.01-031734.82 SAGANJ100834.30-213914.00	G	-	-	-	-	25.80
70	SAGANJ100834.50-213914.00 SAGANJ100943.50+033722.72		274.69 ± 7.15	1.25 ± 0.18	13.3 ± 0.4	-	-
71	SAGANJ100945.37+162546.17	G	-	-	-	_	3.47
72	SAGANJ103129.21+165024.53		-	-	_	-	2.05
73	SAGANJ104618.84 - 032631.00	Q	-	-	8.4 ± 0.3	-	12.30
74	SAGANJ104632.22 + 543559.69	Q	-	-	7.8 ± 0.3	-	2.99
75	SAGANJ105224.06+373004.53	Q	-	-	2.0 ± 0.3	-	25.40

Table A.2: continued.

Sr.No	Name	Type	σ (km s ⁻¹)	M _{BH} (10 ⁹ M _☉)	S _{1400MHz} (mJy)	$\lambda_{\rm Edd}$ (10^{-4})	$\frac{Q_{\text{Jet}}}{(10^{43} \text{ erg s}^{-1})}$
(1)	(2)	(3)	(4)	(5)	(6)	(7)	(8)
76	SAGANJ105309.33+260142.13	G	-	-	1.0 ± 0.2	-	6.43
77	SAGANJ105539.78+143352.23	G	-	-	-	-	11.70
78	SAGANJ112422.77+150957.90	G	269.40 ± 10.48	1.12 ± 0.25	2.3 ± 0.3	3.49	-
79	SAGANJ112800.60-393316.60	G	-	-	-	-	0.64
80	SAGANJ112946.01-012140.55	Q	-	-	7.4 ± 0.2	-	128.00
81	SAGANJ113501.03+344401.65	G	-	-	-	-	25.20
82	SAGANJ114053.13+252546.53	Q	202 00 10 60	2 12 0 60	15 04	- 0.52	15.00
83 84	SAGANJ114344.42+222906.80 SAGANJ114427.19+370831.87	G G	323.02 ± 12.69 224.78 ± 9.13	0.40 ± 0.09	1.5 ± 0.4 4.7 ± 0.4	0.53 29.19	10.70
85	SAGANJ114427.19+370631.87 SAGANJ114738.90-381542.00	G	-	- 0.40	4.7 ± 0.4	29.19	1.95
86	SAGANJ114906.70-120433.00	G	_	_	_	_	10.10
87	SAGANJ120343.71+234304.72	G	253.57 ± 18.06	0.80 ± 0.32	_	5.99	5.43
89	SAGANJ120855.60+464113.79	G	209.64 ± 6.31	0.27 ± 0.05	63.7 ± 2.0	10.18	-
90	SAGANJ121606.10+202054.80	G	-	-	-	-	5.41
91	SAGANJ121615.21+162432.28	G	216.58 ± 38.15	0.33 ± 0.33	-	-	16.50
92	SAGANJ122444.60-254442.00	G	-	-	-	-	1.37
93	SAGANJ123908.61+001833.00	G	-	-	10.0 ± 0.3	-	7.62
94	SAGANJ123944.96+195425.41	Q	-	-	2.4 ± 0.2	-	2.96
95	SAGANJ125154.40+351911.97	G	-	-	3.0 ± 0.2	-	4.91
96 97	SAGANJ125204.82-222645.70	G G	-	-	-	-	$0.69 \\ 2.12$
98	SAGANJ125308.78-013951.73 SAGANJ125809.42+421109.18	G	259.38 ± 15.52	0.01 ± 0.30	-	11.69	6.83
99	SAGANJ130152.71+144843.01	G	278.55 ± 9.42	1.35 ± 0.26	4.2 ± 0.2	-	-
100	SAGANJ130840.02-045645.00	G	-	-	24.1 ± 0.8	_	_
101	SAGANJ131231.35+211543.42	G	246.19 ± 12.53	0.68 ± 0.19	12.2 ± 0.4	61.96	6.88
102	SAGANJ132404.20+433407.13	Q	-	-	3.6 ± 0.2	-	11.90
103	SAGANJ133742.35+294223.31	G	268.86 ± 9.55	1.11 ± 0.22	3.1 ± 0.2	1.85	0.50
104	SAGANJ135228.39 + 093536.02	G	149.29 ± 10.56		39.8 ± 1.3	347.24	2.09
105	SAGANJ140700.50+100918.77	G	186.41 ± 11.70		-	75.74	-
106	SAGANJ141947.89+081423.39	G	251.32 ± 21.57	0.76 ± 0.37	-	51.20	14.40
107	SAGANJ143548.55+201321.38	Q	-	-	7.5 ± 0.3	-	14.20
108	SAGANJ144408.73+260126.43	G			1.6 ± 0.3	1.00	7.82
$\frac{109}{110}$	SAGANJ144928.63-011617.44 SAGANJ145346.50+224314.96	G G	325.03 ± 12.69	3.23 ± 0.71	40.2 ± 1.2 2.8 ± 0.2	1.09	- 9.19
111	SAGANJ145443.40+122510.39	G	226.73 ± 9.89	0.42 ± 0.10	16.2 ± 0.6	_	9.19 -
112	SAGANJ150148.34+434632.50	G	226.67 ± 45.40		1.0 ± 0.2	_	79.60
113	SAGANJ150725.32+082944.51	G	322.86 ± 7.17	3.11 ± 0.39	3.2 ± 0.1	0.83	-
115	SAGANJ154131.89-270736.57	G	-	-		_	4.39
116	SAGANJ154639.13+012422.04	G	353.67 ± 14.72	5.20 ± 1.22	2.3 ± 0.2	1.26	2.31
117	SAGANJ154817.75+072554.85	G	-	-	2.3 ± 0.2	-	24.80
118	SAGANJ155140.30+103548.66	G	241.95 ± 26.76	0.61 ± 0.38	4.3 ± 0.2	71.83	38.60
119	SAGANJ160027.78+083743.04	Q	-	_	-	-	23.20
120	SAGANJ160513.74+071152.56	G	194.99 ± 21.78	0.18 ± 0.11	-	-	13.20
121	SAGANJ160530.66-092728.99	G G	-	-	12.2 ± 0.4	-	18.40
$\frac{122}{123}$	SAGANJ161157.36+073856.19 SAGANJ161242.06+431319.82	G	$\frac{1}{240.66 \pm 14.56}$	$-$ 0.59 \pm 0.20	12.2 ± 0.4 -	-	$\frac{2.73}{3.68}$
123 124	SAGANJ161534.52+095709.96	Q	-	-	7.1 ± 0.3	_	-
125	SAGANJ170627.63+102453.72	Ğ	-	_	-	_	35.60
126	SAGANJ172107.89+262432.17	G	181.63 ± 23.37	0.12 ± 0.09	2.6 ± 0.2	44.30	2.92
127	SAGANJ172109.49+354216.09	Q	-	-	393.0 ± 11.8	-	10.90
128	SAGANJ173105.95 + 242851.85	G	-	-	-	-	59.20
129	SAGANJ174206.97+182720.66	Q	-	-	-	-	23.60
131	SAGANJ182007.41+225120.04	G	-	-	-	-	17.50
132	SAGANJ182938.62+223008.63	G	-	-	-	-	3.72
133 134	SAGANJ190304.60+361650.92	G G	-	-	-	-	0.53
134 137	SAGANJ194349.35-354646.10 SAGANJ204019.60-065910.19	G	-	-	-	-	1.01 14.50
138	SAGANJ204013.00-003310.13 SAGANJ205947.18-250611.03	G	_	_	_	_	1.41
139	SAGANJ213039.21+073530.28	G	208.24 ± 21.71	0.26 ± 0.15	-	_	4.45
140	SAGANJ213745.20-143254.90	$\widetilde{\mathrm{Q}}$	-	-	-	_	76.10
141	SAGANJ214920.70+194043.51	$\ddot{\mathrm{G}}$	-	-	-	-	28.30
142	SAGANJ221536.84 + 290235.90	Q	-	-	-	-	11.90
143	SAGANJ221815.55 + 193143.76	G	273.87 ± 7.91		-	-	0.77
144	SAGANJ223114.32+010041.80	G	276.10 ± 13.64		6.1 ± 0.2	-	2.70
145	SAGANJ223249.13-052958.10	Q	-	-	21.8 ± 0.7	-	- 5 70
146	SAGANJ223836.14-070457.93	G	-	-	-	-	5.72

Table A.2: continued.

Sr.No	Name	Type	σ	$M_{ m BH}$	$S_{1400\mathrm{MHz}}^{\mathrm{c}}$	$\lambda_{ m Edd}$	$Q_{ m Jet}$
			$({\rm km} \; {\rm s}^{-1})$	$(10^9 {\rm M}_{\odot})$	(mJy)	(10^{-4})	$(10^{43} \text{ erg s}^{-1})$
(1)	(2)	(3)	(4)	(5)	(6)	(7)	(8)
148	SAGANJ224621.66+314207.94	G	-	-	-	-	3.32
149	SAGANJ225103.39+061925.49	\mathbf{G}	199.24 ± 9.68	0.20 ± 0.06	3.2 ± 0.2	-	0.68
150	SAGANJ225125.53+160753.60	\mathbf{G}	-	-	-	-	21.30
151	SAGANJ225321.28+162016.77	\mathbf{G}	-	-	-	-	5.09
152	SAGANJ225356.30-070638.60	\mathbf{G}	-	-	-	-	6.60
153	SAGANJ225934.13+082040.78	\mathbf{G}	-	-	1.5 ± 0.2	-	16.90
154	SAGANJ231046.70-210813.90	\mathbf{G}	-	-	-	-	3.40
156	SAGANJ231956.30-272812.40	\mathbf{G}	-	-	-	-	37.50
157	SAGANJ232344.52+145759.35	\mathbf{G}	-	-	-	-	1.53
158	SAGANJ232511.80-323634.60	Q	-	-	-	-	2.99
159	SAGANJ233512.35+174150.38	\mathbf{G}	-	-	-	-	11.30
160	SAGANJ234137.14+082817.25	\mathbf{G}	289.43 ± 15.33	1.68 ± 0.50	1.3 ± 0.2	-	4.66
161	SAGANJ234847.77+160010.32	\mathbf{G}	243.11 ± 15.53	0.63 ± 0.23	-	-	26.40
162	SAGANJ235911.07+170610.97	\mathbf{G}	198.95 ± 6.42	0.20 ± 0.04	-	-	2.34

Table A.3: Column (1) indicates the sample from which the GRGs originate, where 'Others' refers to GRGs from GRG-catalogue which are not part of LoTSS or SGS. Columns (2) and (3) represent the right ascension (RA) in HMS and declination (Dec) in DMS of the host galaxies of the GRGs. Column (4) consists of the jet kinetic power (Q_{Jet}). In Column (5), M_{BH} : central black hole mass ($10^9~M_{\odot}$) estimated from M_{BH} - σ relation. Column (6) includes B_{Edd} : Eddington magnetic field ($10^4~G$) and Column (7) consists the estimated spin of the GRGs.

Sample	RA	Dec	$ m Q_{Jet}$	$ m M_{BH}$	$\mathrm{B}_{\mathrm{Edd}}$	Spin
	(HMS)	(DMS)	$(10^{43} \text{ erg s}^{-1})$	$(10^9 {\rm M}_{\odot})$	$(10^4 {\rm G})$	
(1)	(2)	(3)	(4)	(5)	(6)	(7)
SGS	00 11 19.35	$32\ 17\ 13.83$	3.60 ± 0.72	0.76 ± 0.16	2.18 ± 0.23	0.08 ± 0.02
SGS	00 18 15.21	$21\ 41\ 33.42$	40.60 ± 8.13	0.83 ± 0.29	2.08 ± 0.36	0.26 ± 0.10
SGS	00 38 09.89	09 36 01.33	9.91 ± 1.98	1.05 ± 0.45	1.86 ± 0.40	0.11 ± 0.06
SGS	01 14 30.75	05 08 30.64	3.67 ± 0.73	0.31 ± 0.08	3.40 ± 0.46	0.13 ± 0.04
SGS	$01 \ 33 \ 27.24$	$-08\ 24\ 16.52$	1.79 ± 0.36	2.09 ± 0.43	1.31 ± 0.14	0.03 ± 0.01
$_{ m SGS}$	01 58 26.09	$24\ 51\ 36.38$	0.85 ± 0.17	1.62 ± 0.34	1.49 ± 0.16	0.03 ± 0.01
Others	$07\ 46\ 33.68$	$17\ 08\ 09.63$	0.81 ± 0.17	0.33 ± 0.13	3.28 ± 0.64	0.06 ± 0.03
Others	$07\ 51\ 08.93$	$42\ 31\ 23.6$	2.70 ± 0.54	0.94 ± 0.21	1.96 ± 0.22	0.06 ± 0.02
Others	$08\ 57\ 01.76$	$01\ 31\ 30.93$	2.89 ± 0.58	1.35 ± 0.67	1.63 ± 0.41	0.05 ± 0.03
SGS	$09\ 01\ 23.31$	$19\ 14\ 17.12$	11.20 ± 2.25	0.61 ± 0.26	2.42 ± 0.52	0.16 ± 0.08
Others	09 01 36.70	$21\ 46\ 33.80$	1.12 ± 0.25	4.67 ± 2.67	0.88 ± 0.25	0.02 ± 0.01
SGS	09 08 39.13	$59\ 45\ 12.82$	2.55 ± 0.51	1.98 ± 0.48	1.35 ± 0.16	0.04 ± 0.01
Others	$09\ 11\ 54.57$	08 12 31.13	6.64 ± 1.33	0.66 ± 0.19	2.33 ± 0.33	0.12 ± 0.04
Others	09 32 38.30	$16\ 11\ 57.22$	14.30 ± 2.85	0.77 ± 0.23	2.16 ± 0.32	0.16 ± 0.06
Others	10 21 31.84	$05\ 19\ 02.90$	1.00 ± 0.02	0.94 ± 0.26	1.96 ± 0.28	0.04 ± 0.01
Others	$10\ 32\ 58.88$	$56\ 44\ 53.27$	0.22 ± 0.04	1.34 ± 0.23	1.64 ± 0.14	0.01 ± 0.00
Others	10 34 03.90	18 40 49.00	4.43 ± 0.89	0.54 ± 0.15	2.58 ± 0.36	0.11 ± 0.03
Others	10 36 36.30	$38\ 35\ 07.50$	0.81 ± 0.16	1.35 ± 0.37	1.63 ± 0.22	0.03 ± 0.01
Others	10 48 43.30	11 08 00.30	4.45 ± 0.89	0.94 ± 0.23	1.95 ± 0.24	0.08 ± 0.02
LoTSS	$10\ 57\ 09.25$	48 40 41.03	8.40 ± 1.68	0.81 ± 0.42	2.11 ± 0.56	0.12 ± 0.07
LoTSS	11 04 33.11	$46\ 42\ 25.76$	0.46 ± 0.09	0.11 ± 0.05	5.79 ± 1.24	0.08 ± 0.04
LoTSS	$11\ 05\ 15.27$	$54\ 41\ 09.30$	0.75 ± 0.15	0.79 ± 0.40	2.14 ± 0.54	0.04 ± 0.02
LoTSS	$11\ 18\ 57.28$	$55\ 06\ 56.96$	9.09 ± 1.82	0.47 ± 0.21	2.77 ± 0.61	0.16 ± 0.08
LoTSS	$11\ 21\ 26.44$	$53\ 44\ 56.71$	0.38 ± 0.08	0.43 ± 0.09	2.90 ± 0.30	0.04 ± 0.01
Others	$11\ 21\ 45.00$	$17\ 24\ 25.30$	0.74 ± 0.15	0.72 ± 0.17	2.24 ± 0.27	0.04 ± 0.01
LoTSS	$11\ 24\ 35.86$	$49\ 03\ 25.92$	3.31 ± 0.67	0.63 ± 0.32	2.40 ± 0.60	0.09 ± 0.05
LoTSS	$11\ 27\ 13.18$	$51\ 13\ 26.35$	0.78 ± 0.16	1.18 ± 0.62	1.75 ± 0.46	0.03 ± 0.02
LoTSS	$11\ 32\ 02.31$	$47\ 28\ 24.14$	0.28 ± 0.06	1.09 ± 0.41	1.81 ± 0.34	0.02 ± 0.01
LoTSS	$11\ 32\ 50.67$	$50\ 57\ 04.68$	0.89 ± 0.18	1.34 ± 0.79	1.64 ± 0.48	0.03 ± 0.02
LoTSS	$11\ 35\ 03.20$	$48\ 26\ 12.12$	0.66 ± 0.13	1.53 ± 0.53	1.53 ± 0.27	0.02 ± 0.01
Others	$11\ 35\ 35.23$	$39\ 01\ 45.77$	0.38 ± 0.08	0.02 ± 0.01	12.20 ± 3.48	0.15 ± 0.10
SGS	$11\ 44\ 27.19$	$37\ 08\ 31.87$	10.80 ± 2.16	0.52 ± 0.11	2.64 ± 0.28	0.17 ± 0.04
LoTSS	$11\ 48\ 14.98$	$54\ 57\ 16.49$	0.11 ± 0.02	0.41 ± 0.13	2.96 ± 0.47	0.02 ± 0.01
SGS	$12\ 03\ 43.71$	$23\ 43\ 04.72$	5.49 ± 1.10	0.87 ± 0.30	2.03 ± 0.34	0.09 ± 0.04
LoTSS	$12\ 18\ 49.88$	$50\ 26\ 17.59$	11.30 ± 2.26	0.46 ± 0.15	2.80 ± 0.46	0.18 ± 0.07
LoTSS	$12\ 20\ 28.13$	$52\ 51\ 44.89$	0.75 ± 0.15	0.54 ± 0.28	2.59 ± 0.67	0.04 ± 0.03
LoTSS	$12\ 22\ 55.24$	$49\ 26\ 42.32$	0.34 ± 0.07	1.76 ± 0.51	1.43 ± 0.21	0.02 ± 0.01
LoTSS	$12\ 25\ 31.36$	$49\ 46\ 43.95$	0.24 ± 0.05	1.43 ± 0.66	1.59 ± 0.36	0.02 ± 0.01
LoTSS	$12\ 29\ 36.25$	$50\ 13\ 04.65$	0.94 ± 0.19	0.47 ± 0.26	2.78 ± 0.76	0.05 ± 0.03
LoTSS	$12\ 32\ 04.95$	$53\ 06\ 27.31$	0.49 ± 0.10	0.41 ± 0.19	2.98 ± 0.69	0.04 ± 0.02
LoTSS	$12\ 41\ 42.34$	$51\ 35\ 14.32$	6.17 ± 1.24	2.22 ± 1.19	1.27 ± 0.34	0.06 ± 0.04
Others	$12\ 47\ 33.31$	$67\ 23\ 16.34$	0.20 ± 0.04	0.73 ± 0.13	2.22 ± 0.19	0.02 ± 0.00

A&A proofs: manuscript no. SAGAN1_AA

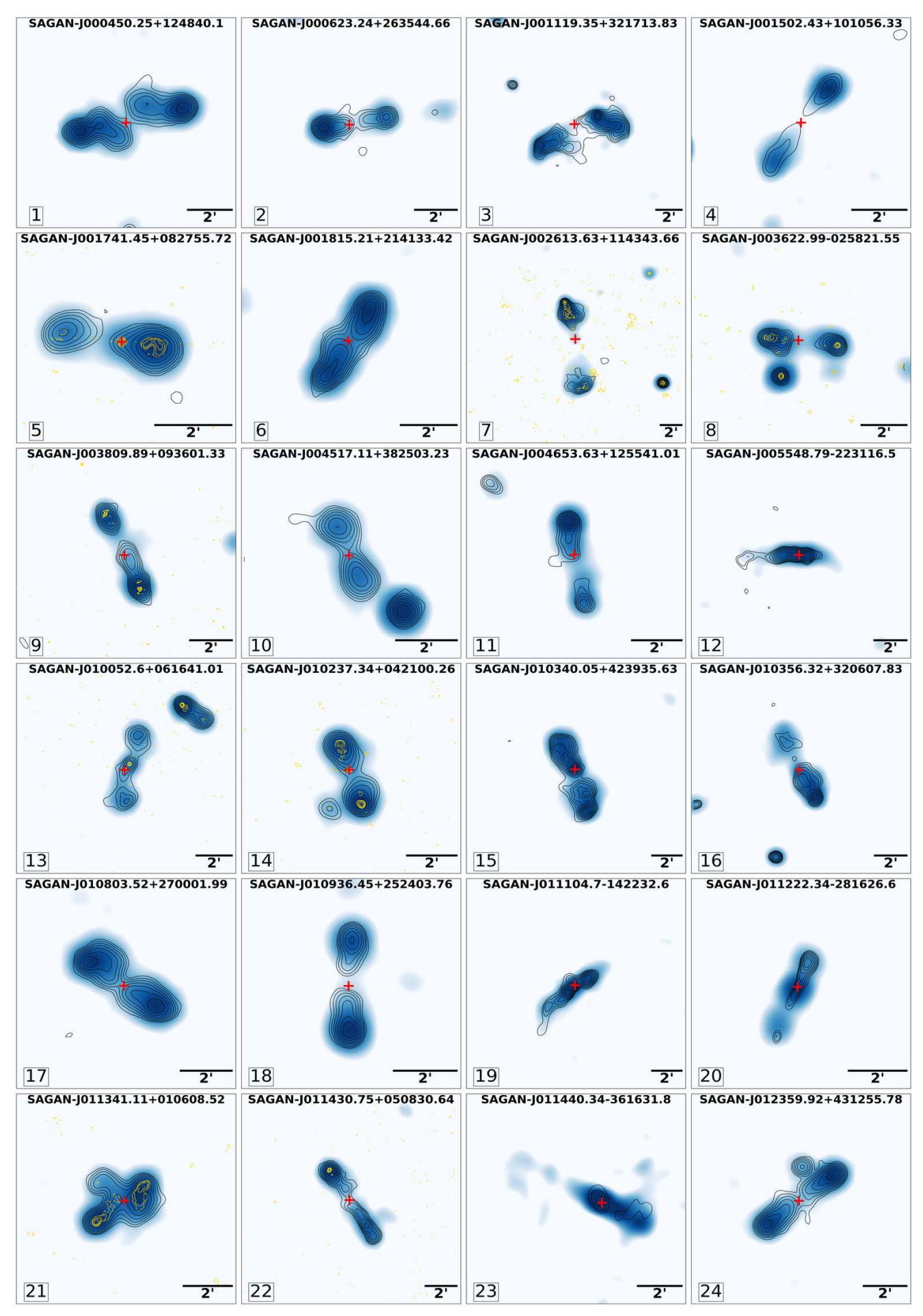
Table A.3: continued.

Sample	RA	Dec	$Q_{ m Jet}$	M _{BH}	B _{Edd}	Spin
(1)	(HMS)	(DMS)	$(10^{43} \text{ erg s}^{-1})$	$(10^9 {\rm M}_{\odot})$	(10^4 G)	(=)
(1)	(2)	(3)	(4)	(5)	(6)	$\frac{(7)}{2000000000000000000000000000000000000$
Others	12 53 03.20	45 00 44.80	0.70 ± 0.14	0.86 ± 0.17	2.04 ± 0.20	0.03 ± 0.01
$\begin{array}{c} ext{Others} \\ ext{SGS} \end{array}$	12 55 50.13	58 18 41.72	1.48 ± 0.31	2.81 ± 1.58	1.13 ± 0.32	0.03 ± 0.02
	12 58 09.42	42 11 09.18 53 59 48.65	7.08 ± 1.42	0.96 ± 0.28	1.93 ± 0.28	0.10 ± 0.03
LoTSS $LoTSS$	13 03 31.08		0.29 ± 0.06	0.55 ± 0.18	2.56 ± 0.42	0.03 ± 0.01
SGS	13 03 32.18 13 12 31.35	52 20 02.02 21 15 43.42	0.63 ± 0.13 6.87 ± 1.37	1.07 ± 0.42 0.77 ± 0.20	1.83 ± 0.36 2.17 ± 0.28	0.03 ± 0.01 0.11 ± 0.03
Others	13 13 57.70	64 25 55.00	1.95 ± 0.40	0.77 ± 0.20 0.89 ± 0.30	2.17 ± 0.28 2.01 ± 0.34	0.06 ± 0.02
LoTSS	13 14 04.60	54 39 37.88	8.91 ± 1.79	1.43 ± 0.62	1.59 ± 0.35	0.00 ± 0.02 0.09 ± 0.05
LoTSS	13 22 29.07	50 48 44.53	0.30 ± 0.06	0.63 ± 0.02	2.38 ± 0.33	0.03 ± 0.03 0.03 ± 0.01
LoTSS	13 24 35.19	50 41 02.31	4.27 ± 0.86	0.03 ± 0.17 0.21 ± 0.10	4.10 ± 0.97	0.03 ± 0.01 0.17 ± 0.09
LoTSS	13 31 35.25	45 59 55.53	1.91 ± 0.38	4.33 ± 2.10	0.91 ± 0.22	0.02 ± 0.01
LoTSS	13 32 58.28	53 53 55.60	2.23 ± 0.45	2.09 ± 0.93	1.31 ± 0.22	0.04 ± 0.02
LoTSS	13 36 18.75	53 39 52.12	0.47 ± 0.09	0.67 ± 0.24	2.32 ± 0.41	0.04 ± 0.02 0.03 ± 0.01
SGS	13 37 42.35	29 42 23.31	0.53 ± 0.10	1.13 ± 0.24	1.79 ± 0.19	0.03 ± 0.01
LoTSS	13 42 06.98	47 25 53.04	1.02 ± 0.20	2.13 ± 0.58	1.30 ± 0.13 1.30 ± 0.18	0.03 ± 0.01 0.03 ± 0.01
Others	13 45 03.60	39 52 31.00	1.99 ± 0.40	0.63 ± 0.19	2.39 ± 0.36	0.07 ± 0.01
LoTSS	13 45 57.55	54 03 16.62	6.36 ± 1.27	0.24 ± 0.08	3.84 ± 0.67	0.19 ± 0.02
LoTSS	13 49 27.92	46 20 15.11	2.46 ± 0.49	0.64 ± 0.38	2.38 ± 0.70	0.07 ± 0.05
Others	13 50 00.70	29 47 21.40	0.22 ± 0.06	1.45 ± 0.44	1.58 ± 0.24	0.01 ± 0.03 0.01 ± 0.01
SGS	13 52 28.39	09 35 36.02	2.10 ± 0.42	0.09 ± 0.03	6.47 ± 1.10	0.18 ± 0.07
LoTSS	13 56 28.50	52 42 19.23	1.35 ± 0.27	1.90 ± 0.92	1.38 ± 0.34	0.03 ± 0.02
LoTSS	13 59 51.16	47 03 21.03	0.59 ± 0.12	0.99 ± 0.43	1.91 ± 0.42	0.03 ± 0.02 0.03 ± 0.01
Others	14 00 43.40	30 19 19.00	7.71 ± 1.54	0.86 ± 0.13	2.05 ± 0.27	0.11 ± 0.03
LoTSS	14 07 18.48	51 32 04.63	53.70 ± 10.80	0.28 ± 0.15	3.60 ± 0.27	0.52 ± 0.32
LoTSS	14 16 25.89	54 25 45.85	4.81 ± 0.96	1.27 ± 0.41	1.68 ± 0.27	0.07 ± 0.03
Others	14 18 37.75	37 46 23.00	1.06 ± 0.21	0.65 ± 0.15	2.35 ± 0.27	0.05 ± 0.01
SGS	14 19 47.89	08 14 23.39	14.70 ± 2.94	0.84 ± 0.13	2.07 ± 0.21	0.16 ± 0.07
LoTSS	14 28 57.66	54 36 27.81	4.11 ± 0.83	0.95 ± 0.54	1.95 ± 0.55	0.08 ± 0.05
LoTSS	14 29 33.45	54 43 35.29	1.09 ± 0.22	0.49 ± 0.11	2.71 ± 0.30	0.06 ± 0.01
Others	14 31 03.40	33 45 41.60	0.48 ± 0.11	2.33 ± 0.64	1.24 ± 0.17	0.02 ± 0.01
LoTSS	14 31 36.99	52 27 24.90	3.32 ± 0.67	1.28 ± 0.47	1.68 ± 0.30	0.06 ± 0.03
LoTSS	14 44 10.50	55 47 45.64	6.60 ± 1.32	2.48 ± 0.76	1.20 ± 0.18	0.06 ± 0.02
LoTSS	14 45 20.87	54 03 29.62	2.80 ± 0.56	1.94 ± 1.15	1.36 ± 0.40	0.04 ± 0.03
Others	14 45 27.40	09 32 18.00	0.18 ± 0.04	0.37 ± 0.07	3.11 ± 0.31	0.03 ± 0.03
LoTSS	14 46 07.20	48 41 37.79	2.76 ± 0.56	0.92 ± 0.38	1.97 ± 0.40	0.06 ± 0.03
Others	14 53 02.93	33 08 40.80	10.30 ± 2.07	1.00 ± 0.31	1.90 ± 0.29	0.12 ± 0.04
LoTSS	14 57 02.81	48 06 46.64	0.04 ± 0.01	1.31 ± 0.46	1.66 ± 0.29	0.01 ± 0.00
LoTSS	15 01 32.11	50 34 55.14	0.35 ± 0.07	2.49 ± 0.95	1.20 ± 0.23	0.01 ± 0.01
LoTSS	15 06 24.10	53 55 02.61	1.16 ± 0.23	0.86 ± 0.26	2.05 ± 0.32	0.04 ± 0.02
Others	15 24 44.60	19 59 57.08	1.83 ± 0.40	0.59 ± 0.31	2.47 ± 0.65	0.07 ± 0.04
SGS	15 46 39.13	01 24 22.04	2.39 ± 0.48	3.75 ± 1.01	0.98 ± 0.13	0.03 ± 0.01
\overline{SGS}	15 51 40.30	10 35 48.66	38.40 ± 7.71	0.71 ± 0.36	2.25 ± 0.56	0.27 ± 0.16
SGS	16 05 13.74	07 11 52.56	13.30 ± 2.66	0.28 ± 0.14	3.61 ± 0.91	0.26 ± 0.15
SGS	16 12 42.06	43 13 19.82	3.70 ± 0.74	0.69 ± 0.20	2.28 ± 0.33	0.09 ± 0.03
SGS	17 21 07.89	$26\ 24\ 32.17$	2.95 ± 0.59	0.20 ± 0.12	4.21 ± 1.21	0.14 ± 0.09
SGS	21 30 39.21	07 35 30.28	4.61 ± 0.92	0.37 ± 0.17	3.12 ± 0.73	0.13 ± 0.07
Others	21 45 04.53	$-06\ 59\ 07.76$	2.79 ± 0.58	2.55 ± 0.81	1.19 ± 0.19	0.04 ± 0.01
SGS	22 18 15.55	19 31 43.76	0.78 ± 0.16	1.22 ± 0.23	1.72 ± 0.17	0.03 ± 0.01
\overline{SGS}	22 31 14.32	01 00 41.80	2.80 ± 0.56	1.27 ± 0.33	1.69 ± 0.22	0.06 ± 0.02
SGS	22 51 03.39	06 19 25.49	0.71 ± 0.14	0.30 ± 0.07	3.44 ± 0.41	0.06 ± 0.02
SGS	23 41 37.14	08 28 17.25	4.72 ± 0.94	1.56 ± 0.43	1.52 ± 0.21	0.06 ± 0.02
\overline{SGS}	23 48 47.77	16 00 10.32	23.60 ± 4.74	0.73 ± 0.22	2.23 ± 0.34	0.21 ± 0.08
SGS	23 59 11.07	17 06 10.97	2.32 ± 0.46	0.30 ± 0.05	3.45 ± 0.31	0.10 ± 0.02

Table A.4: RA and Dec represent the right ascension and declination of the GRGs's host galaxies in HMS and DMS respectively. Column 5 shows the m_r of the BCGs. The parameters like the r_{200} and R_{L*} have been obtained from the WHL galaxy cluster catalogue, and M_{200} has been estimated using equation 2 of Wen et al. (2012). r_{200} is the virial radius (Mpc) of the galaxy cluster, M_{200} is the mass ($10^{14}M_{\odot}$) of the cluster within r_{200} , and N_{200} is the number of galaxies present within r_{200} . Column 11 shows the comoving number density of galaxies within r_{200} . Column 12 includes the ratio of half of the linear extent of the source to the virial radius.

No	WHL Cluster	RA	Dec	$m_{\rm r}$	z	r ₂₀₀	R_{L*}	M_{200}	N_{200}	Density	Ratio
		(HMS)	(DMS)			(Mpc)		$(10^{14} {\rm M}_{\odot})$		${ m Mpc^{-3}}$	
(1)	(2)	(3)	(4)	(5)	(6)	(7)	(8)	(9)	(10)	(11)	(12)
1	J013327.2-082417	01 33 27.24	$-08\ 24\ 16.52$	15.90	0.14893	0.87	16.26	0.85	15	5.44	0.53
2	J014208.5 - 064143	$01\ 42\ 08.56$	$-06\ 41\ 43.40$	15.12	0.12447	1.30	36.91	2.21	22	2.39	0.34
3	J072538.8 + 400413	$07\ 25\ 38.75$	$40\ 04\ 12.52$	16.14	0.16148	0.85	12.42	0.62	9	3.50	0.49
4	J085349.8 + 145226	$08\ 53\ 49.78$	$14\ 52\ 26.04$	14.79	0.06933	0.81	13.18	0.66	9	4.04	0.46
5	J090123.3 + 191417	$09\ 01\ 23.31$	$19\ 14\ 17.12$	17.87	0.27649	0.90	15.02	0.77	10	3.27	0.63
6	J090839.1 + 594513	$09\ 08\ 39.13$	$59\ 45\ 12.82$	17.01	0.24004	1.36	41.19	2.51	37	3.51	0.48
7	J100943.5 + 033723	$10\ 09\ 43.50$	$03\ 37\ 22.72$	14.77	0.10513	0.95	17.40	0.92	8	2.23	0.39
8	J112422.8+150958	$11\ 24\ 22.77$	$15\ 09\ 57.90$	16.34	0.17194	1.17	30.92	1.79	22	3.28	0.39
9	J114344.4 + 222907	$11\ 43\ 44.42$	$22\ 29\ 06.80$	16.55	0.18079	0.76	13.51	0.68	14	7.61	0.53
10	J120343.7 + 234305	$12\ 03\ 43.71$	$23\ 43\ 04.72$	16.64	0.17670	1.36	41.48	2.53	40	3.80	0.38
11	J121606.1 + 202055	$12\ 16\ 06.10$	$20\ 20\ 54.80$	18.39	0.26300	0.89	15.45	0.80	13	4.40	0.60
12	J125154.4+351912	$12\ 51\ 54.40$	$35\ 19\ 11.97$	17.81	0.20100	0.83	12.28	0.61	11	4.59	0.62
13	J130152.7+144843	$13\ 01\ 52.71$	$14\ 48\ 43.01$	15.51	0.13761	0.98	17.50	0.92	12	3.04	0.43
14	J133742.3 + 294223	$13\ 37\ 42.35$	$29\ 42\ 23.31$	15.16	0.11547	0.93	13.30	0.67	9	2.67	0.49
15	J144928.6 - 011617	$14\ 49\ 28.63$	$-01\ 16\ 17.44$	16.32	0.20233	1.04	20.47	1.11	15	3.18	0.44
16	J154639.1 + 012422	$15\ 46\ 39.13$	$01\ 24\ 22.04$	16.22	0.20836	1.04	25.13	1.41	12	2.55	0.45
17	J155140.3 + 103549	$15\ 51\ 40.30$	$10\ 35\ 48.66$	17.98	0.36824	1.13	25.99	1.46	23	3.81	0.55
18	J221815.6 + 193144	$22\ 18\ 15.55$	$19\ 31\ 43.76$	15.14	0.10964	1.35	47.92	2.99	28	2.72	0.28

Appendix B: Radio maps of all GRGs from NVSS, FIRST and TGSS.



Article number, page 36 of 42

Fig. B.1: NVSS colour images of GRGs-1.

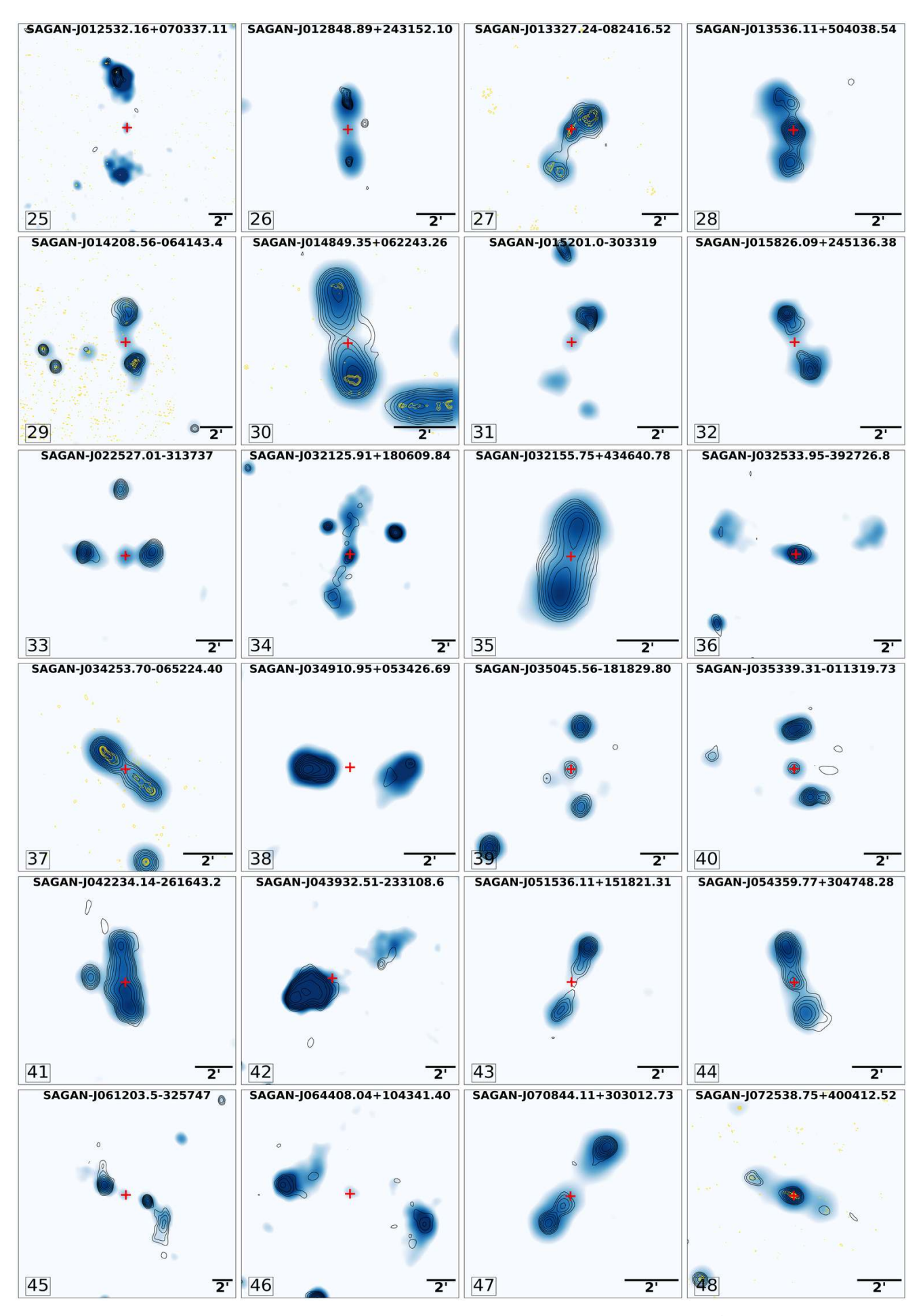
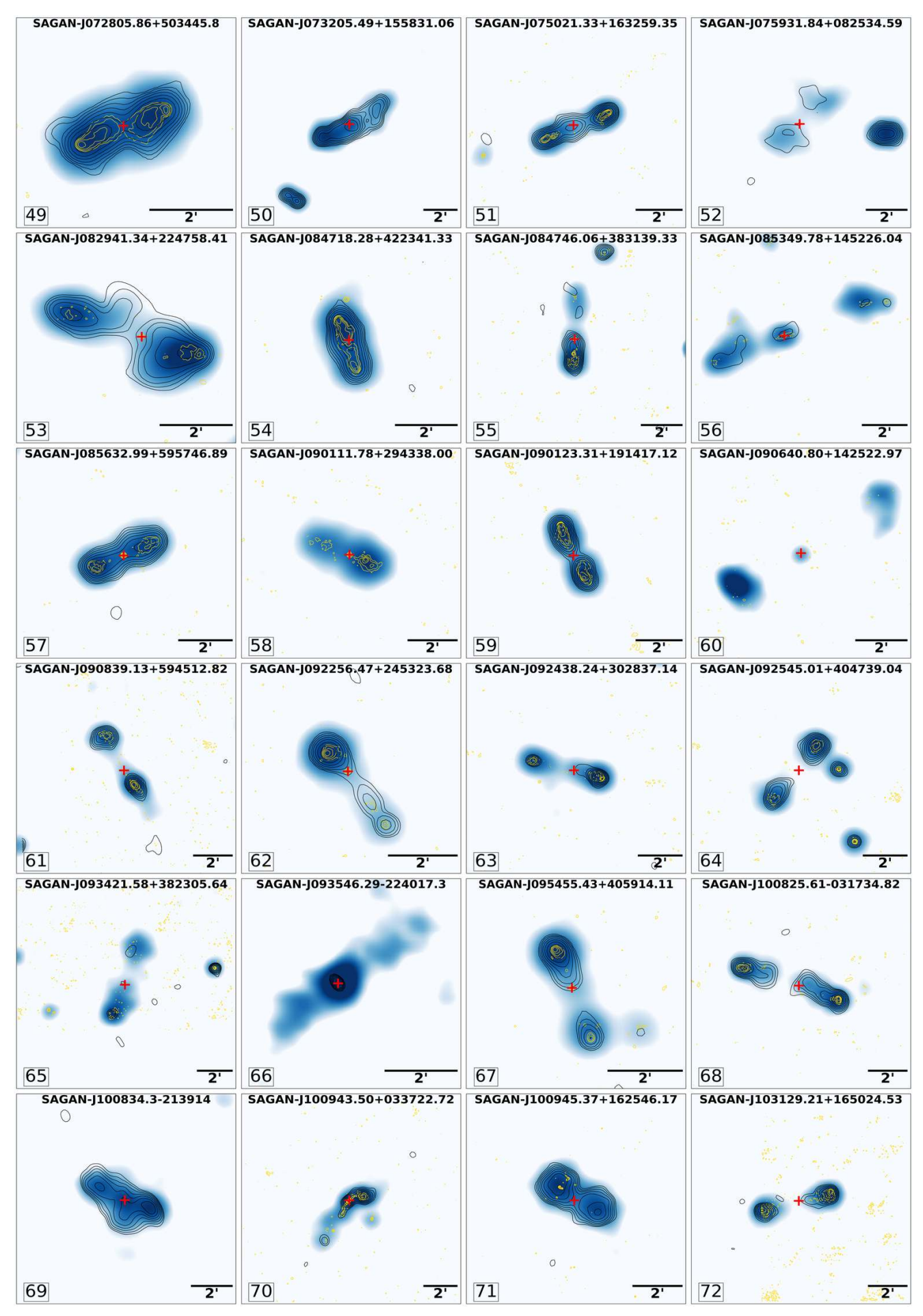


Fig. B.2: NVSS colour images of GRGs-2.



Article number, page 38 of 42

Fig. B.3: NVSS colour images of GRGs-3.

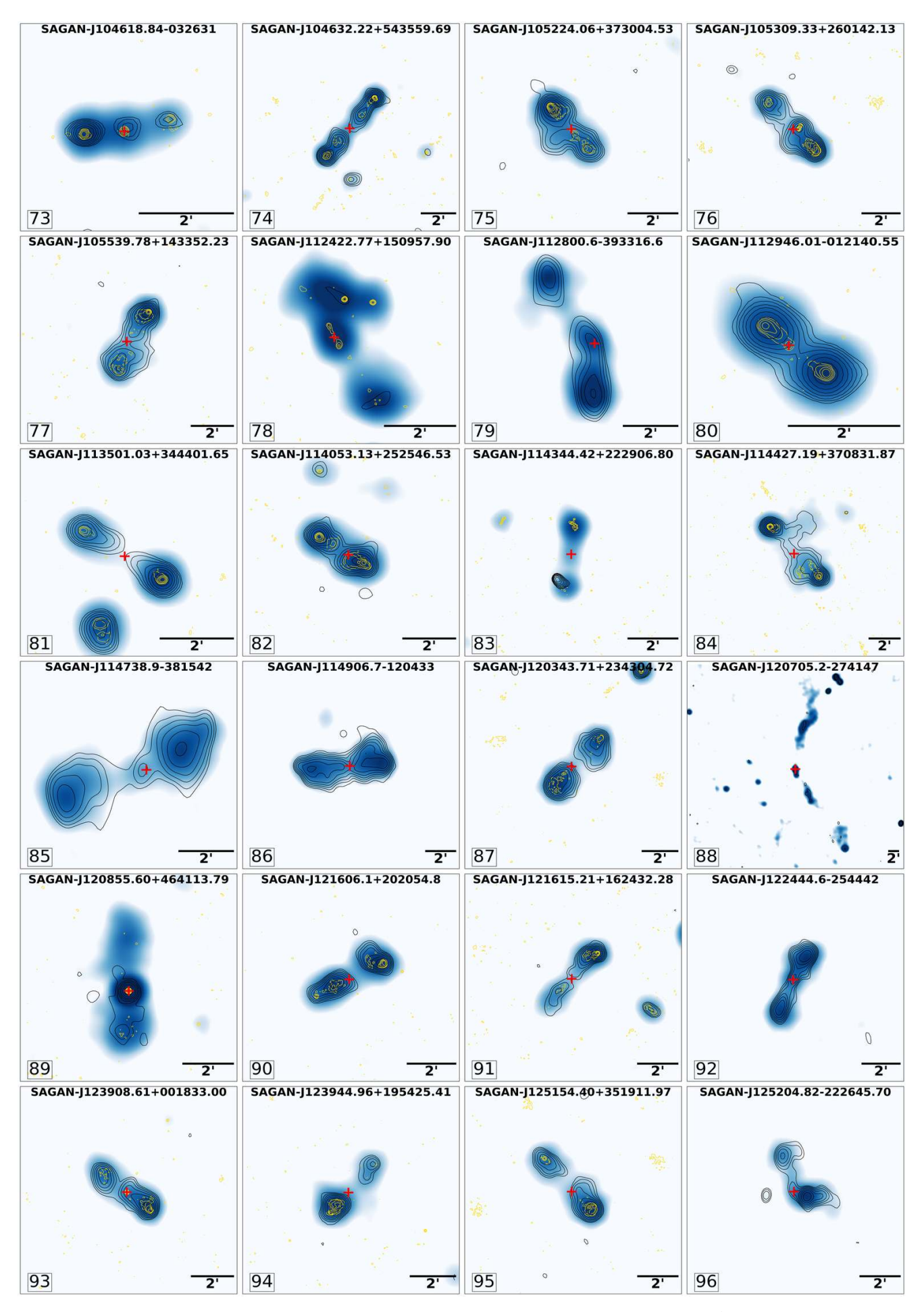
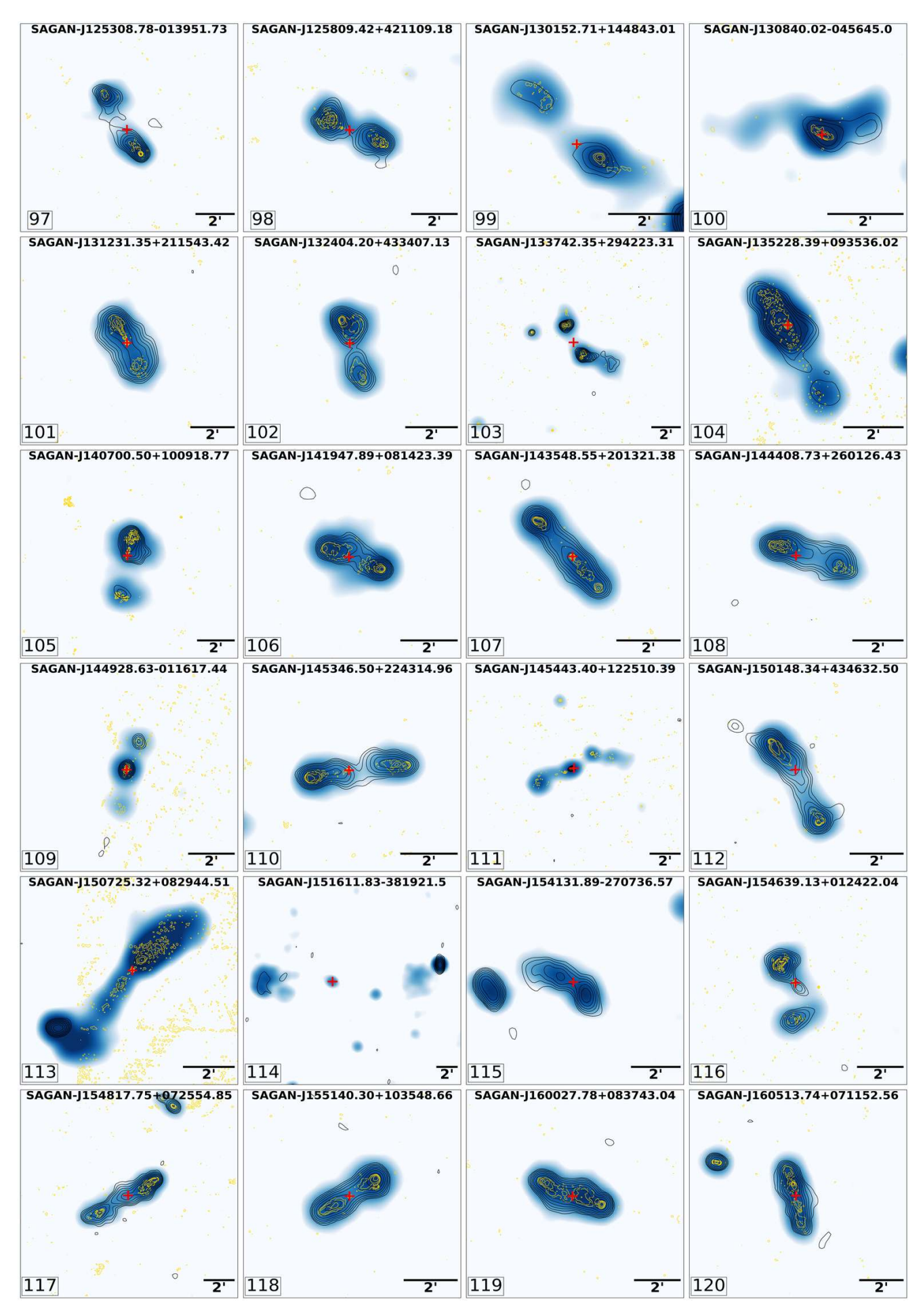


Fig. B.4: NVSS colour images of GRGs-4.



Article number, page 40 of 42

Fig. B.5: NVSS colour images of GRGs-5.

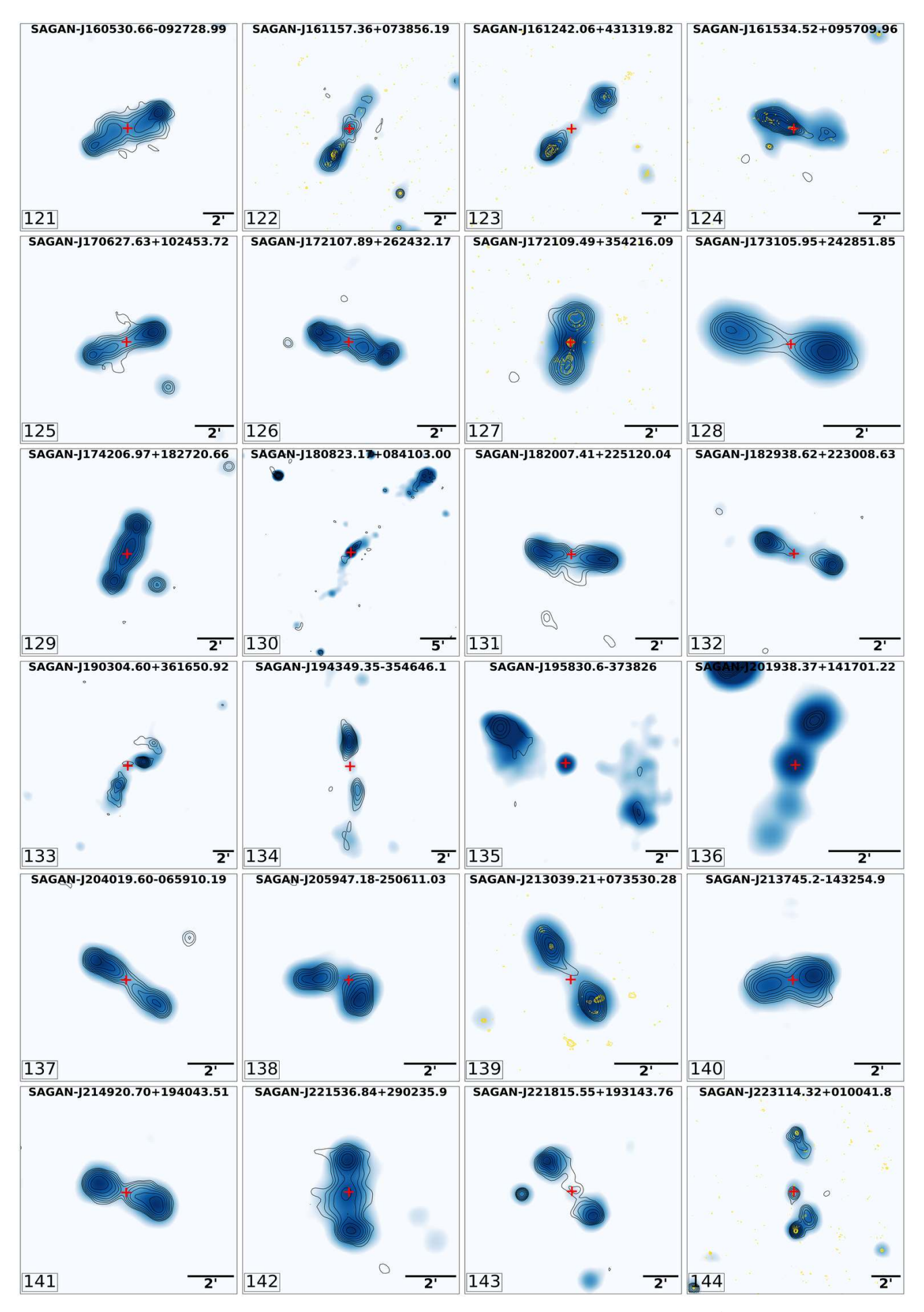
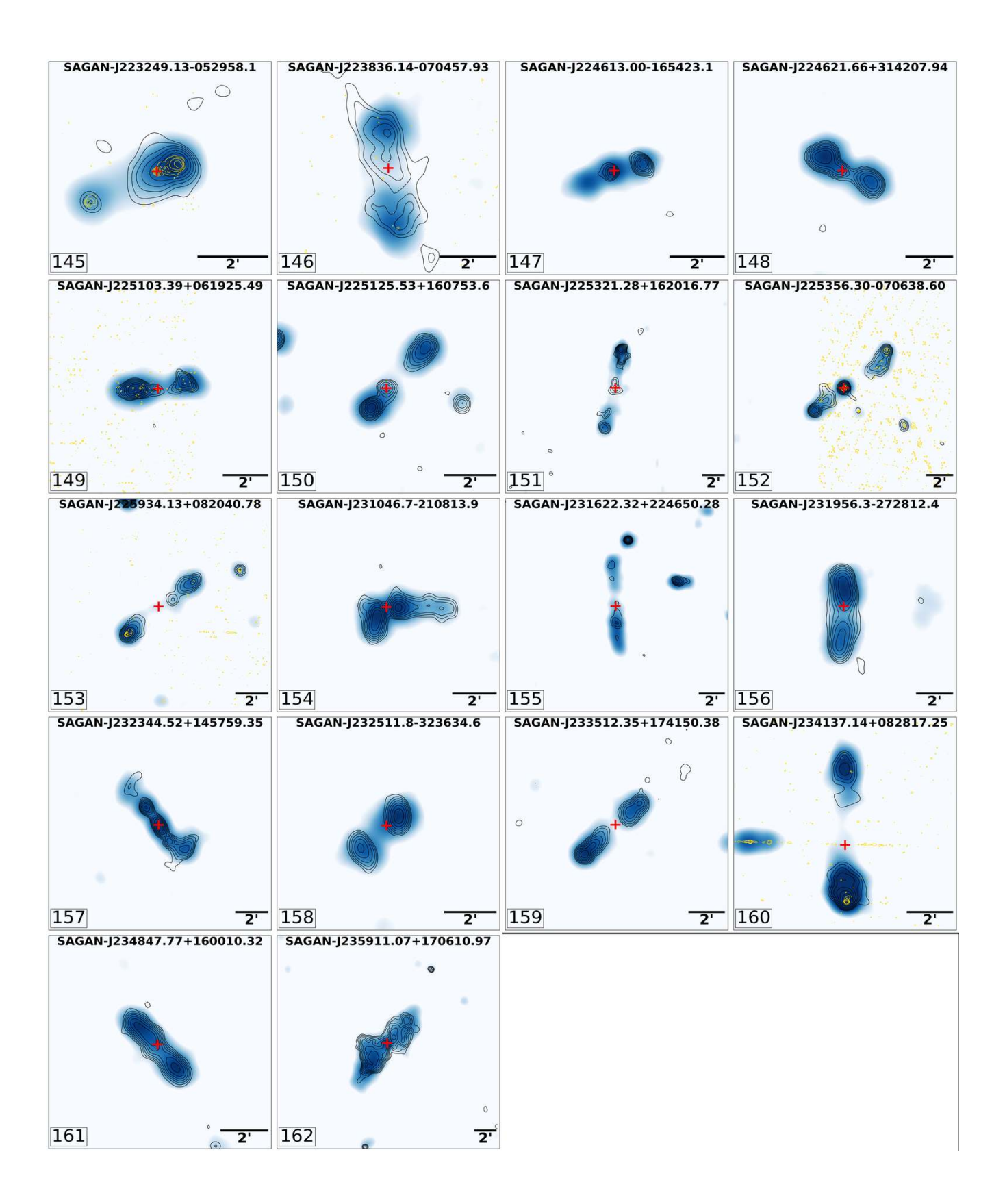


Fig. B.6: NVSS colour images of GRGs-6.



Article number, page 42 of 42

Fig. B.7: NVSS colour images of GRGs-7.